1996

Wangara Day 33 : reevaluation of lower order turbulence closure prediction of the PBL

Frank Freedman
San Jose State University

INFORMATION TO USERS

This manuscript has been reproduced from the microfilm master. UMI films the text directly from the original or copy submitted. Thus, some thesis and dissertation copies are in typewriter face, while others may be from any type of computer printer.

The quality of this reproduction is dependent upon the quality of the copy submitted. Broken or indistinct print, colored or poor quality illustrations and photographs, print bleedthrough, substandard margins, and improper alignment can adversely affect reproduction.

In the unlikely event that the author did not send UMI a complete manuscript and there are missing pages, these will be noted. Also, if unauthorized copyright material had to be removed, a note will indicate the deletion.

Oversize materials (e.g., maps, drawings, charts) are reproduced by sectioning the original, beginning at the upper left-hand corner and continuing from left to right in equal sections with small overlaps. Each original is also photographed in one exposure and is included in reduced form at the back of the book.

Photographs included in the original manuscript have been reproduced xerographically in this copy. Higher quality 6" x 9" black and white photographic prints are available for any photographs or illustrations appearing in this copy for an additional charge. Contact UMI directly to order.

UMI

A Bell & Howell Information Company
300 North Zeeb Road, Ann Arbor MI 48106-1346 USA
313/761-4700 800/521-0600

WANGARA DAY 33: REEVALUATION OF LOWER ORDER TURBULENCE CLOSURE PREDICTION OF THE PBL

A Thesis

Presented to

The Faculty of the Department of Meteorology

San Jose State University

In Partial Fulfillment

of the Requirements for the Degree

Master of Science

by

Frank Freedman

December, 1996

APPROVED FOR THE DEPARTMENT OF METEOROLOGY

Dr. Robert D. Bornstein

Dr. Jerry L. Steffens

Dr. Douglas M. Sinton

APPROVED FOR THE UNIVERSITY

ABSTRACT

WANGARA DAY 33: REEVALUATION OF
LOWER ORDER TURBULENCE CLOSURE PREDICTION OF THE PBL

by Frank Freedman

The Wangara Day 33 period was resimulated to address unresolved issues concerning the accuracy of lower order turbulence closure (LOTC) planetary boundary layer (PBL) predictions. A one-dimensional, flat-terrain formulation of the TVM meso-β scale numerical model, modified to include improved PBL representations, was employed.

Predictions of daytime mean variables, turbulent fluxes, and mixed layer depth agreed with observations and with the results of higher order turbulence closure models. Predicted turbulent kinetic energy (TKE) was over-concentrated within the lower region of the PBL, attributed to the down-gradient representation of TKE flux. Inaccuracies associated with LOTC are thus isolated to predictions of PBL turbulent structure, as opposed to predictions of mean variables.

Profiles of predicted nighttime mean and turbulent variables showed decoupling of the nighttime PBL into a surface-based nocturnal boundary layer (NBL), and a quasi-adiabatic residual layer (RL) aloft. TKE within the NBL was overpredicted due to inadequate representations of turbulent length scales. TKE within the RL was highly dependent on RL stabilization rate through height variations of radiative cooling within the layer.

ACKNOWLEDGEMENTS

The author would like to thank Dr. Robert Bornstein for his guidance in all stages of this publication. Appreciation is also addressed to Dr. Ted Yamada for making available to the author the Clarke et al. (1971) Wangara report, and to Dr. B. B. Hicks for his help in locating upper level weather maps for the Wangara Day 33 period.

On a personal level, deepest gratitude is expressed to the faculty, staff, and students of the San Jose State Meteorology Department for their friendship and good-humor during the publication process, and especially to Ms. Nina Rivas for her inspiration and encouragement during the final stages of the research.

TABLE OF CONTENTS

Page

Abstract iv
Acknowledgements v
Table of Contents vi
List of Tables vii
List of Figures viii

1. INTRODUCTION 1
a. Daytime W33 simulations: HOTC models 5
b. Daytime W33 simulations: LOTC models 8
c. Nighttime W33 simulations 12
d. Scope of current W33 simulations 14

2. MODEL FORMULATION 15
a. Radiative flux 16
b. Surface temperature and specific humidity 19
c. Surface boundary layer 27
d. PBL turbulence 35

3. MODEL SETUP 42

4. RESULTS 50
a. Daytime PBL structure 52
b. Nighttime PBL structure 59
1) Nocturnal Boundary Layer 61
2) Residual Layer 64

5. CONCLUSION 68

References 74
Appendix 83

LIST OF TABLES

page

Table 1. Higher order turbulence closure models used to simulate W33 3

Table 2. Lower order turbulence closure models used to simulate W33 4

Table 3. Atmospheric and soil grid levels 43

Table 4. Surface and soil parameters 44

Table 5. Initial values for soil temperature and moisture 47

LIST OF FIGURES

Fig. 1. Time/height cross-section of observed W33 virtual potential temperature; abscissa origin corresponds to 0600 LST Day 33.

Fig. 2. Time/height cross-section of interpolated (a) zonal and (b) meridional W33 geostrophic wind components (from Yamada and Mellor 1975).

Fig. 3. Vertical profiles of (a) simulated and (b) observed daytime W33 virtual potential temperature, as computed by André et al. (1978); times are LST.

Fig. 4. Vertical profiles of simulated daytime W33 vertical kinematic heat flux, as computed by André et al. (1978); times are LST.

Fig. 5. Same as in Fig. 3, but for specific humidity.

Fig. 6. Same as in Fig. 4, but for vertical kinematic moisture flux.

Fig. 7. Same as in Fig. 3, but for horizontal wind speed.

Fig. 8. Same as in Fig. 4, but for (a) zonal and (b) meridional momentum fluxes.

Fig. 9. Vertical profiles of (a) simulated and (b) observed nighttime W33 virtual potential temperature, as computed by André et al. (1978): —— 1800 LST Day 33, ---- 2100 LST Day 33, -·-·- 0000 LST Day 34, ····· 0300 LST Day 34, -··-·· 0600 LST Day 34, —— 0900 LST Day 34.

Fig. 10. Vertical profiles of (a) simulated and (b) observed nighttime W33 horizontal wind speed, as computed by André et al. (1978). Symbols as in Fig. 9.

Fig. 11. Vertical profiles of (a) vertical and (b) horizontal nighttime W33 turbulent kinetic energy (TKE), as computed by André et al. (1978): —— 1800 LST Day 33, ---- 2100 LST Day 33, ····· 0300 LST Day 34, -·-· 0700 LST Day 34.

Fig. 12. Monin-Obukhov non-dimensional gradients $\phi_m = \phi_h$ from Webb (1970) (solid), and ϕ_m (dashed) and ϕ_h (dashed-dot) from Beljaars and Holtslag (1991)

Fig. 13. Time variation of simulated (solid) and observed (dashed) W33 (a) $T_{1.2}$, (b) $q_{1.2}$, and (c) V_{16}; abscissa origin corresponds to 0600 LST Day 33.

Fig. 14. Time variation of (a) observed and (b) simulated W33 surface energy fluxes: —— R_N, ---- H_G, -·-·- H_S, -*-*- H_L; abscissa as in Fig. 13

Fig. 15. Time variation of simulated (solid) and observed (dashed) W33 u_*; abscissa as in Fig. 13.

Fig. 16. Time/soil depth cross-sections of simulated W33 (a) T_S (°C), and (b) η (% by volume); abscissa origin as in Fig. 13. In (b), ordinate changes from linear to logarithmic at z_s = 1 cm.

Fig. 17. Vertical profiles of (a) observed and (b) simulated W33 θ_v: —— 0900 LST Day 33, ---- 1200 LST Day 33, -·-·- 1500 LST Day 33, -*-*- 1800 LST Day 33.

Fig. 18. Turbulent (solid) and radiative (dashed) heating rates at 1200 LST Day 33.

Fig. 19. Vertical profiles of W33 simulated θ_v for simulation without RFD and w_s; symbols as in Fig. 17.

Fig. 20. Vertical profiles of simulated W33 vertical kinematic heat flux: —— 1000 LST Day 33, ---- 1200 LST Day 33, -·-·- 1400 LST Day 33, -*-*- 1600 LST Day 33.

Fig. 21. Vertical profiles of (a) observed and (b) simulated W33 q; symbols as in Fig. 17.

Fig. 22. Vertical profiles of simulated W33 vertical kinematic moisture flux; symbols as in Fig. 20.

Fig. 23. Vertical profiles of (a) observed and (b) simulated W33 V: ---- 1200 LST Day 33, -·-·- 1500 LST Day 33, -*-*- 1800 LST Day 33.

Fig. 24. Vertical profiles of (a) observed and (b) simulated W33 wind direction; symbols as in Fig. 23.

Fig. 25. Vertical profiles of simulated (a) zonal and (b) meridional W33 momentum fluxes; symbols as in Fig. 20.

Fig. 26. Vertical profiles of simulated W33 TKE; symbols as in Fig. 20.

Fig. 27. Vertical profiles of simulated (solid) and mixed layer similarity-based (dashed) non-dimensional turbulent kinetic energy for 1200 LST Day 33; similarity profile computed from (52).

Fig. 28. Simulated non-dimensional TKE production budget for 1200 LST Day 33; symbols represent production rates due to: —— wind shear, ---- buoyancy, -·-·- molecular dissipation, -*-*- turbulent transport.

Fig. 29a. Profiles of non-dimensional horizontal and vertical daytime W33 TKE components as computed by André et al. (1978): —— 1200 LST Day 33, ---- 1600 LST Day 33.

Fig. 29b. Non-dimensional daytime W33 TKE production budget as computed by André et al. (1978); symbols represent production rates due to: **** wind shear, —— buoyancy, ····· molecular dissipation, ------ turbulent transport.

Fig. 30. Vertical profiles of simulated W33 (a) θ_v and (b) V: —— 1800 LST Day 33, ---- 2100 LST Day 33, -·-·- 0000 LST Day 34, -*-*- 0300 LST Day 34.

Fig. 31. Vertical profiles of simulated W33 Ri: —— 2000 LST Day 33, ---- 0200 LST Day 34; abscissa changes from linear to logarithmic at Ri = 1.

Fig. 32. Vertical profiles of simulated W33 TKE: —— 1600 LST Day 33, ---- 2000 LST Day 33, -·-·- 0000 LST Day 34, -*-*- 0400 LST Day 34; abscissa changes from linear to logarithmic at $e = 10^{-2}$ m^{2}s^{-2}.

Fig. 33. Vertical profiles of (a) observed and (b) simulated W33 q; symbols as in Fig. 30.

Fig. 34. Vertical profiles of (a) observed and (b) simulated W33 NBL θ_v; symbols as in Fig. 30.

Fig. 35. Turbulent (solid) and radiative (dashed) NBL heating rates at (a) 0000 LST Day 34 and (b) 0300 LST Day 34; caret on right oridinate denotes h_s.

Fig. 36. Time variation of W33 h_t (solid) and h_s (dashed); hour 14 is at 2000 LST Day 33

Fig. 37. Same as in Fig. 34, but for V.

Fig. 38. Vertical profiles of simulated (solid) and local similarity-based non-dimensional NBL turbulent kinetic energy for 0000 LST Day 34; similarity profiles computed from (54) for $\alpha' = 1.75$ (dashed) and 1.50 (dashed-dot).

Fig. 39. Simulated profiles of W33 NBL TKE production budget terms for 0000 LST Day 34; symbols represent production rates due to: —— wind shear, ---- buoyancy, -·-·- molecular dissipation; -*-*- time tendency term.

Fig. 40. Vertical profiles of (a) observed, and (b) simulated W33 RL θ_v; symbols as in Fig. 30.

Fig. 41. Same as in Fig. 40, but for V.

Fig. 42. Same as in Fig. 40, but for wind direction.

Fig. 43. Simulated profiles of W33 RL TKE production budget terms for (a) 2000 LST Day 33 and (b) 0200 LST Day 34; symbols represent production rates due to: —— wind shear, ---- buoyancy, -·-·- molecular dissipation; -*-*- time tendency term.

Fig. 44. Vertical profiles of W33 RL total warming rate; slope of superimposed line represents average height-variation of RL warming rate: —— 1800 LST Day 33, ---- 2200 LST Day 33, -·-·- 0200 LST Day 34.

Fig. 45. As Fig. 44, but for Case B.

Fig. 46. As Fig. 43, but for Case B.

Fig. 47a. Simulated Case B profiles of W33 RL TKE; symbols and abscissa as in Fig. 32.

Fig. 47b. Simulated Case B profiles of W33 RL Ri; symbols as in Fig. 30, abscissa as in Fig. 31.

Fig. 48. Time/height cross-section of wind speed difference V_B-V_A (cm s^{-1}); solid and dashed contours denote positive and negative values, respectively. Abscissa as in Fig. 16.

Fig. 49. Simulated vertical profiles of W33 RL K_m for (a) Case A and (b) Case B: —— 2000 LST Day 33, ---- 0000 LST Day 33, -·-·- 0400 LST Day 34.

Fig. 50. Diffusion coefficients σ_z for Pasquill-Gifford stability categories A-F, and those obtained for selected d using (56) and values of K_m representative of the range obtained from Cases A and B; ⊙ $K_m = 0.4$ m^2s^{-1}, ⊗ for $K_m = 3.5$ m^2s^{-1}. Adopted from Slade (1968).

1. INTRODUCTION

The Wangara boundary layer experiment (Clarke et al. 1971) took place from 15 July to 27 August 1967 at a largely flat and vegetation-free site near Hay, Australia (34°30' S, 144°56' W). Data compiled during the experiment include vertical profiles of wind, temperature, and mixing ratio; surface geostrophic, and 0-1 and 1-2 km thermal winds; and micrometeorological profile measurements. These data have been instrumental in aiding planetary boundary layer (PBL) research, having been used to determine surface momentum, heat, and humidity fluxes (Hicks 1981; Wetzel and Chang 1988), PBL universal functions and constants (Clarke and Hess 1974; Hicks 1976), and analytical expressions for daytime and nighttime PBL depth (Deardorff 1974a; Yamada 1979; Mahrt et al. 1979; Malcher and Kraus 1983). A complete description of the Wangara experiment can be found in Clarke et al. (1971) and Hess et al. (1981).

The most common use of the Wangara data has been to evaluate one-dimensional PBL numerical prediction models by simulation of all or part of Days 33-35 of the experiment (hereafter referred to as W33). This period was cloudless and free of synoptic frontal influence, thus satisfying many one-dimensional PBL model assumptions. In addition, the daytime PBL was highly convective and capped at ~ 1000 m by a well-defined stable layer (Fig. 1). The period thus provides an excellent opportunity to evaluate the accuracy of PBL turbulence parameterizations, as well as to quantify exchange processes between the PBL and capping stable layer.

Summaries of many W33 modeling studies are given in Table 1 for those employing higher order turbulence closure (HOTC) and Table 2 for those employing lower order turbulence closure (LOTC). HOTC models employ predictive equations for turbulent fluxes of mean variables, with terms that represent mechanical, buoyant, pressure, and transportive effects governing the time tendency of these fluxes. LOTC models, on the other hand, employ parameterizations for these fluxes that in general only capture mechanical contributions (and some pressure effects). Discrepancies between HOTC and LOTC model predictions are most evident in simulation of daytime, free-convective conditions, in which generation of turbulent fluxes is strongly influenced by non-mechanical processes. A detailed summary of turbulence closure schemes is found in Uliasz (1994).

Types of HOTC models used to simulate W33 include second-order Level 2.5, third-order, and large-eddy simulation (LES). LOTC models are, except for PX (abbreviations defined in Tables 1 and 2), based on eddy-diffusivity theory. Methods for computation of eddy diffusivity range from algebraic specification (PM, MP) to those based on prognostic determination of turbulent kinetic energy (TKE). In the latter, different methods of computing turbulent length scale l were employed.

In most simulations, surface thermodynamic forcing was specified based on either fluxes deduced from micrometeorological profiles or from surface temperature and specific humidity predictions of DE. In either case, peak daytime surface convective heat

Table 1. Higher order turbulence closure models used to simulate W33

Author/ Abbrev.	Sim. Period[1]	Surface Forcing	Large-Scale Forcing[2]	Turbulence Closure[3]
Deardorff (1974a,b), DE	0900-1800, Day 33	Predicted	$V_g = f(z)$	• Large-eddy simulation
Wyngaard and Coté (1974), WC	0900-1800, Day 33	Specified	$V_g = f(z)$	• 2nd-Order Level 4 • K-closure on triple corr.
Yamada and Mellor (1975), YM	0900-0900, Days 33-35	Specified	$V_g = f(z,t)$ θ-advection w_s	• 2nd-Order Level 3 • K-closure on triple corr.
Yamada (1977), YA	0900-0900, Days 33-35	Specified	$V_g = f(z,t)$ θ-advection w_s	• 2nd-Order Level 2.5 • K-closure on triple corr.
André et al. (1978), AN	0900-0900, Days 33-34	Specified	$V_g = f(z,t)$	• 3rd-Order
Sun and Ogura (1980), SO	0900-1800, Day 33	Specified	$V_g = f(z)$ θ-advection	• 2nd-Order Level 3 • ZL-closure on triple corr.
Chen and Cotton (1983), CC	0900-1800, Day 33	Specified	$V_g = f(z)$	• 2nd-Order Level 4 • ZL-closure on triple corr.

[1] All times LST.

[2] See Appendix for definition of symbols.

[3] Closure "level" refers to hierarchy defined by Mellor and Yamada (1974). Closure of triple correlations refers to method of parameterizing turbulent transport terms: K-closure employs local gradient diffusion method, ZL-closure employs method of Zeman and Lumley (1976).

Table 2. Lower order turbulence closure models used to simulate W33

Author/ Abbrev.	Sim. Period[1]	Surface Forcing	Large-Scale Forcing[2]	Turbulence Closure[2]
Pielke and Mahrer (1975), PM	0900-1800, Day 33	Specified	$V_g = f(z)$	• O'Brien (1970) K
McNider and Pielke (1981), MP	0900-0900, Days 33-34	Predicted	$V_g = f(z,t)$	• O'Brien / Blackadar (1979) K
Mailhot and Benoit (1982), MB	0600-0900, Days 33-34	Predicted	$V_g = f(z,t)$	• K-e • Prognostic ℓ
Therry and Lacarrère (1983), TL	0900-1800, Day 33	Specified	$V_g = f(z,t)$	• K-e • Algebraic ℓ
Ramanathan et al. (1995), RA	0900-0900, Days 33-34	Specified	$V_g = f(z)$ θ-advection w_s	• K-e • Prognostic ϵ
Pleim and Xiu (1995), PX	Day/Night Days 33-34	Predicted	$V_g = f(z,t)$	• Non-local closure

[1] All times LST.

[2] See Appendix for definition of symbols.

fluxes ranged from 220-270 Wm^{-2} and peak midday latent heat fluxes were ~ 70 Wm^{-2}. Later prognostic approaches by MB and PX yielded similar peak convective heat fluxes, but smaller peak latent heat fluxes (~ 20 Wm^{-2}).

Large scale forcing was derived from measurements of surface geostrophic, and 0-1 and 1-2 km thermal winds. In daytime-only simulations, height dependent geostrophic winds V_g (defined by vertical interpolation using surface geostrophic and thermal wind measurements) were held constant in time at the 0900 LST Day 33 values. In simulations of both the daytime and nighttime periods, interpolations were performed in time and height, as described by YM. Resulting temporal and spacial fields of zonal and meridional geostrophic wind components (Fig. 2a,b) show that the period was characterized by height-decreasing and time-increasing geostrophic speed, and a directional shift from easterly to northeasterly.

Horizontal potential temperature advection (YM, YA, SO, RA) was evaluated from horizontal temperature gradients implied by the height-variation of the geostrophic wind. Large-scale subsidence rates w_s (YM, YA, RA) were specified based on linear time/height interpolations of experimental determinations, as discussed by YM.

a. Daytime W33 simulations: HOTC models

The HOTC models used to simulate daytime W33 produced similar results, with slight degradation in the results of less sophisticated HOTC models. Because the AN

model is the highest order (non LES) closure model used to simulate W33, its results will be presented as the "best" case, with the results of other HOTC models discussed for comparative purposes.

Profiles of AN simulated and observed mean virtual potential temperature θ_v (Fig. 3a,b) show a well-mixed (adiabatic) layer bounded from below by a superadiabatic surface boundary layer (SBL) and from above by the capping stable layer. The super-adiabatic SBL and well-mixed layer comprise the convective boundary layer (CBL), which warms and grows with time as surface heat is fluxed upward and erodes the base of the capping stable layer. The cooling simulated at the CBL top h_i results from entrainment of relatively cooler CBL air into the elevated stable layer. This cooling is less apparent in the observations due probably to subsidence ($w_s < 0$), not accounted for in this simulation. The lack of imposed subsidence also explains the slight overestimation of h_i.

Profiles of simulated kinematic heat flux (Fig. 4) are linear within the CBL, leading to height-invariant CBL heating rates (Fig. 3a,b). The negative heat flux at h_i results from entrainment at h_i. This flux is on average 15% of the surface value (this ratio is hereafter referred to as r_i), a value in good agreement with the range of 5-20% derived from atmospheric and laboratory observations. (Lenschow 1974; Willis and Deardorff 1974). The value of r_i determines CBL growth rate $\partial h/\partial t$. Since CBL mean and turbulent structures scale with h_i (Deardorff 1970), accurate simulation of r_i is crucial.

Simulated and observed specific humidity profiles q (Fig. 5a,b) show drying below ~ 700 m and moistening above this height relative to the 0900 LST Day 33 profile. Explanation of this tendency is obtained from inspection of simulated vertical profiles of kinematic specific humidity flux (Fig. 6). Humidity flux is a maximum at h_i, leading to drying throughout the CBL and moistening above the CBL. Net drying below 700 m and moistening above 700 m results from the time-integrated effect of these tendencies, as the region below/above 700 m exists a sufficient/insufficient amount of time below h_i for CBL drying to counteract earlier moistening when the region was above h_i. Although the late afternoon mean mixed layer specific humidity is accurately predicted, drying is too gradual in the simulation. This suggests an overestimation of surface specific humidity flux and/or the importance of horizontal advection, not considered in the simulation.

The tendency and vertical structure of mean wind speed V are fairly well reproduced (Fig. 7a,b). The linear profile of zonal momentum flux (Fig. 8a) results from small meridional components of momentum (not shown) and geostrophic wind (Fig. 2b), while the parabolic profile of meridional momentum flux (Fig. 8b) results from a vertically uniform zonal wind (not shown) and a decreasingly negative zonal geostrophic wind component with height (Fig. 2a). As shown by WC and Arya and Wyngaard (1975), these structures can be deduced from the mean momentum equation for vertically well-mixed, steady-state flow.

Degradation of results with decreased HOTC model sophistication is most evident when comparing values of r_i. While AN computed values of ~ 15% (and DE of 14-21%), sequentially less sophisticated models computed averages as follows: CC, 12%; WC, 8-10%; SO, 5-7%; YM, < 2%. Since lower values of r_i result in less entrainment between the CBL and capping stable layer, slightly smaller values of h_i are computed by sequentially less sophisticated HOTC models. In addition, less sophisticated HOTC models slightly overestimated mean mixed layer specific humidity, as less entrainment of dry air from above h_i was simulated.

b. Daytime W33 simulations: LOTC models

LOTC schemes are usually characterized by specification of a non-negative eddy diffusivity K, a parameterized measure of atmospheric mixing efficiency. The vertical turbulent flux of a mean variable is computed as the negative product of K and the local vertical gradient of the mean variable. Proportionality of fluxes to local vertical gradients corresponds to mechanical generation of fluxes, which because K is non-negative results in down-gradient directed vertical fluxes. This closure, however, neglects buoyant and transportive processes governing the generation of fluxes, which are not proportional to local mean gradients and which cause fluxes to at times be directed *up*-gradient.

The PM model employed the O'Brien (1970) formulation for K, in which its vertical profile is prescribed based on SBL stability and h_i, the latter computed from the

DE prognostic equation. This closure more effectively models the CBL than methods that hold h_i constant and/or use K profiles based on local conditions (e.g. McPherson 1970; Pandolfo et al. 1965), as it is based on conditions within the SBL and at h_i known to be important in determining CBL characteristics. Predicted potential temperature profiles were in good agreement with observations, with slight overprediction of h_i due to the lack of subsidence in the simulation. However, since the focus of the study was on the vertical structure of *mean* variables, turbulent flux profiles were not presented.

The MB and TL studies employed K-e closure, in which K is computed as a function of prognostically determined TKE (denoted by e) and algebraically or prognostically determined l. This approach has the following advantages over K closure models, which either prescribe K (as in PM) or compute it as a function of local *mean* variables

- By including a prognostic equation for TKE, a measure of turbulent intensity (which equals TKE multiplied by two) is obtained. Knowledge of this quantity is necessary to properly describe situations in which its advection is important (e.g., in coastal regions) and is necessary for input into air pollutant dispersion models.
- Since the TKE equation is derived from the Navier-Stokes equation, the description of turbulent intensity is valid for all stabilities and flow regimes (although parameterizations of certain terms necessary for practical use of the equation result in some

loss of generality). Computation of K from TKE is thus theoretically appealing, and responds more robustly to temporal and spacial changes in stability.

The main disadvantage of the K-e approach is the necessity to compute l. Results are sensitive to the formulation of l, yet no universally accepted theoretical basis for its formulation has been established (Mellor and Yamada 1982).

Values of r_i computed by TL range from 10-15%, similar to those computed by AN (Fig. 4), while those of MB are as high as 60%. This latter value is much higher than an upper limit of ~ 20% obtained from observational, laboratory, and theoretical determinations (Lenschow 1970, 1974; Willis and Deardorff 1974; Zeman 1975). As a result of overpredicting r_i, the MB simulated maximum h_i (~ 1600 m) is much higher than observed, and than those computed in other modeling studies. The dissimilarity of results obtained by TL and MB is attributed to their different formulations of l; TL computed it by use of algebraic equations, derived with regard to CBL observations and HOTC model results, while MB employed a prognostic equation based on SBL induced convection (Busch et al. 1976), with no special regard to the CBL dynamics.

To eliminate the need for computing l in K-e closure, a predictive equation for eddy dissipation rate ϵ can be used, with K expressed as a function of prognostically determined values of TKE and ϵ. This scheme was employed by RA to simulate daytime W33; however, the model produced overly large values of both r_i (~ 25%) and h_i. This is

most likely due to underpredicted values of ϵ (see Fig. 8 in RA), as compared with observations and mixed layer scaling theory (Kitchen et al. 1983; Guillement et al. 1983). These results illustrate the difficulty associated with formulating a prognostic equation for ϵ suitable for atmospheric applications (Detering and Etling 1985; Stull 1988).

The importance of buoyant and transportive turbulent processes within the CBL has led to the use of "non-local" or "integral" closure CBL models (e.g. Estoqué 1968; Zhang and Anthes 1982; Stull 1984). This closure containes explicit parameterization of turbulent exchange between all model layers, as opposed to *K* and *K-e* closures, which describe exchange only between adjacent layers. In the non-local model used by PX for daytime W33, multi-layer, non-local transfer was used only for upward mixing, while a local, layer-by-layer approach was used for downward mixing, consistent with the idea of "bottom-up" and "top-down" convection proposed by Wyngaard and Brost (1984) and further developed by Zilitinkevich (1994). Values of h_i computed by PX, however, were underpredicted by ~ 200 m. with no cooling simulated at the base of the capping stable layer. As discussed above, such cooling is a signature of entrainment, which acts to deepen the mixed layer.

In summary, results obtained by LOTC simulations of daytime W33 show great dissimilarity, with significant inaccuracies in the results of many models. Because of this, assessment of the practical consequences of the limited physics represented in LOTC, at least based on daytime W33 simulation, is difficult. This assessment is,

however, important due to the predominant use of LOTC parameterizations in practically applied three-dimensional meteorological prediction models.

c. Nighttime W33 simulations

Nighttime W33 has been less simulated than its daytime counterpart, with only limited, qualitative descriptions of results. In addition, since nighttime turbulence is weak and predominantly mechanically driven, results obtained by HOTC and LOTC models are similar. Separate discussions of nighttime W33 results obtained by HOTC and LOTC models are thus not necessary. AN results will again be highlighted, as these are generally representative of those obtained from all nighttime W33 simulations.

AN simulated nighttime θ_v (Fig. 9a) show a highly stable layer below ~ 200 m, which cools and grows vertically throughout the evening due to turbulent and radiative flux divergences. Above 200 m, the atmosphere cools gradually and approximately uniformly with height due to radiative flux divergence. Qualitative agreement with observations (Fig. 9b) is found, with discrepancies (mainly above 200 m) most likely resulting from the lack of horizontal advection in the simulation.

Simulated and observed V (Fig. 10a,b) increase throughout the evening, producing a low level jet (LLJ) at the top of the surface based stable layer. This acceleration is due to an inertial oscillation in the wind field, which develops after sunset in response to a rapid decrease in turbulent energy. The simulated LLJ height is underpredicted, shown by AN to be caused by an overly small value of roughness length used in the simulation.

Near-elimination of TKE at sunset is shown in simulated nighttime horizontal and vertical TKE components (Fig, 11a,b). This rapid decrease is caused by suppression of buoyant motion near the surface (due to the high thermal stability in this region), and subsequent dissipation of TKE aloft. Regeneration of TKE occurs later in the evening near the surface and in certain regions above 400 m. Anisotropy in horizontal and vertical TKE components results from the combined effects of nighttime thermal stability (Fig. 9a,b), which destroys vertical TKE, and wind shear (Fig. 10a,b), which produces horizontal TKE.

Whereas the daytime W33 PBL structure is characterized by strong, dominant turbulent mixing, the corresponding nighttime structure is reflective of a variety of meteorological processes, such as horizontal advection, radiative flux divergence, pressure gradient/Coriolis force imbalances, and turbulence. Many of these processes either result from or are highly influenced by the three-dimensional, meso and synoptic scale structure of the atmosphere. The fact that data on these scale were not extensively measured during the Wangara field study, coupled with the sparsity of detailed knowledge on nocturnal PBL dynamics at the time of most of the W33 modeling studies, explains the limited number and scope of nighttime simulations. The accumulation of detailed knowledge on nighttime PBL structure/dynamics enables the simulation of the nighttime period to be expanded.

d. Scope of current W33 simulations

In the above review, two weaknesses concerning previous W33 modeling studies were identified:

- Daytime W33 results of LOTC models were ambiguous and in some cases erroneous, making their comparison with observations and HOTC model results difficult.
- The scope of the nighttime W33 simulations was limited.

In light of these points, the W33 case will again be simulated. The model to be used employs *K-e* LOTC, with *l* computed following TL algebraic equations modified for nocturnal conditions. Resimulation of the daytime period with this closure will allow for an in-depth investigation to more carefully assess the degradation involved with the use of LOTC. In the nighttime phase, the closure gives information on both the mean and turbulent states of the nocturnal PBL, which can be evaluated and explained based on knowledge of the nocturnal PBL not available at the time of the majority of previous W33 studies.

2. MODEL FORMULATION

The current study employs the Topographic Vorticity Mode (TVM) meso-β scale model described by Schayes et al. (1996; hereafter referred to as S96). The model differs from more commonly used primitive equation models in that vorticity is conserved rather than momentum. Prognostic equations for the two horizontal vorticity components are thus solved, with updated values used to diagnose the wind field through a stream function vector. The model can be formulated in either a hydrostatic or non-hydrostatic mode (Thunis 1995). Its basic equations and methods of numerical solution are given in the two above references. Predicted model fields have compared favorably with those derived from idealized cases and observational field studies (Panayiotou 1995; Thunis 1995; Bornstein et al. 1996).

A one-dimensional, hydrostatic version of TVM will be used in the current simulation. This configuration is well suited for W33, as mesoscale forcing due to horizontal gradients of topography and surface characteristics were generally small. Important processes include vertical turbulent mixing associated with surface heating and cooling, radiative flux divergence, and those forced by the tendency and vertical structure of large scale synoptic fields, which must all be either parameterized or specified in one-dimensional PBL model applications. Because accurate parameterization and specification of these processes are crucial to successfully simulate W33, changes were made to appropriate portions of the model. Equations will be given for new schemes, along with

descriptive explanations of old schemes to highlight their limitations; equations for the old schemes are given in S96.

a. Radiative flux

Both solar (shortwave) and terrestrial (longwave) radiative fluxes for cloudless conditions are computed each time step based on modeled vertical profiles of temperature and specific humidity. Shortwave fluxes are computed following the method outlined in Pielke (1984), which accounts for attenuation due to Raleigh scattering, water vapor absorption, and surface albedo. In S96, longwave fluxes were computed following the grey-body model of Sasamori (1968), in which atmospheric emissivities for water vapor and carbon dioxide in all longwave bands are represented by single analytical equations for each gas. This formulation was changed to include more modern versions of these equations, and to better account for downward emitted longwave radiation from above the model top.

Downward and upward longwave radiative fluxes are computed, respectively, from

$$F_D(z) = F_D(z_T)[1 - \epsilon_D(z)] + \int_{\epsilon_D(z_T)}^{\epsilon_D(z)} B[T(z)]d\epsilon_D \qquad (1a)$$

$$F_U(z) = F_U(0)[1 - \epsilon_U(z)] + \int_0^{\epsilon_U(z)} B[T(z)]d\epsilon_U \ , \qquad (1b)$$

where all symbols are defined in the Appendix. Emissivities ϵ_D and ϵ_U are given by the sum of emissivities from water vapor and carbon dioxide, which, following Kondratyev (1969) and Welch and Zdunkowski (1976), are given as

$$\begin{aligned} \epsilon_{vD} &= \sum_{i=0}^{4} a_i (\ln \omega_{vD})^i \\ \epsilon_{vU} &= \sum_{i=0}^{4} b_i (\ln \omega_{vU})^i \end{aligned} \tag{2}$$

$$\begin{aligned} \epsilon_{cD} &= 1 - \exp(-0.3319\, \omega_{cD}^{0.4}) \\ \epsilon_{cU} &= 1 - \exp(-0.3319\, \omega_{cU}^{0.4}) \end{aligned} \tag{3}$$

$$\begin{aligned} \epsilon_D &= \epsilon_{vD} + \epsilon_{cD} - \epsilon_{vD}\epsilon_{cD} \\ \epsilon_U &= \epsilon_{vU} + \epsilon_{cU} - \epsilon_{vU}\epsilon_{cU} \,. \end{aligned} \tag{4}$$

The third terms on the right hand sides of (4) correct for the spectral overlap of water vapor and carbon dioxide emission. Optical pathlengths for water vapor and carbon dioxide in (2) and (3) are given by

$$\begin{aligned} \omega_{vD}(z) &= \omega_{vD}(z_T) + \int_{z_T}^{z} \rho q (p/p_0)^{0.9}\, dz' \\ \omega_{vU}(z) &= \int_{0}^{z} \rho q (p/p_0)^{0.9}\, dz' \end{aligned} \tag{5a}$$

$$\begin{aligned} \omega_{cD}(z) &= \omega_{cD}(z_T) + \rho_c \int_{z_T}^{z} \rho/\rho_0 (p/p_0)^{0.9}\, dz' \\ \omega_{cU}(z) &= \rho_c \int_{0}^{z} \rho/\rho_0 (p/p_0)^{0.9} dz' \,, \end{aligned} \tag{5b}$$

where pressure p is computed by hydrostatic integration. Note that the concentration of carbon dioxide ρ_c is assumed constant.

In the application of (1)-(5), values for F_D, ϵ_D, ω_{vD}, and ω_{cD} at z_T must be specified. This is a problem in models in which z_T is located within the lower troposphere, as such values are difficult to determine. Calculation of F_D is thus carried out in an extended vertical domain, with a top z_R located at ~ 15 km. Approximately 15 additional grid levels are thus utilized, with required values of θ and q either interpolated from a local radiosonde sounding, or extrapolated from z_T upward through the extended domain. In the latter case, θ is linearly extrapolated assuming a gradient identical to its initial condition at z_T, while q is assumed to exponentially decrease with height above z_T. Resulting θ and q values within the extended domain are then held fixed throughout the simulation.

Extension from z_T to z_R necessitates specification of F_D, ϵ_D, ω_{vD}, and ω_{cD} at z_R. $F_D(z_R)$ is set to a constant value (~ 75 Wm^{-2}), consistent with climatological emissions by stratospheric water vapor, carbon dioxide, and ozone. The specification of a non-zero value for $F_D(z_R)$ implies the presence of emitting gas above z_R, and hence non-zero values for $\epsilon_D(z_R)$, $\omega_{vD}(z_R)$, and $\omega_{cD}(z_R)$. However, negligible influences on lower tropospheric values of F_D were found in association with specification of both zero and non-zero values of these parameters. For simplicity, $\epsilon_D(z_R)$, $\omega_{vD}(z_R)$, and $\omega_{cD}(z_R)$ are thus set to zero.

b. Surface temperature and specific humidity

The primary mechanism driving the temporal variation of meteorological variables within the PBL is heating and evaporation at the earth surface. Resulting changes in surface temperature T_0 and specific humidity q_0 produce fluxes of heat and moisture between the surface and atmosphere. Accurate prediction of atmospheric variables over broad range of conditions necessitates prediction of T_0 and q_0 through use of surface energy and moisture balance equations, which for unvegetated soil can be expressed, respectively, as

$$R_S + R_D = R_U(T_0) + H_S(T_0) + H_L(T_0, q_0) + H_G(T_0, q_0) \tag{6}$$

$$P = E_0(T_0, q_0) + W_0(T_0, q_0) \ . \tag{7}$$

The left hand side of (6) represents shortwave and longwave radiation absorbed at the surface, while the terms on the right hand side represent, respectively, upward emitted longwave radiation from the surface, convective heat flux between the surface and atmosphere, latent heat flux from surface evaporation or condensation, and conductive heat flux between the surface and soil. The left hand side of (7) represents precipitation, while the terms on the right hand side represent, respectively, evaporation/condensation and the transport of liquid and water vapor between the surface and soil.

Because of the non-linear coupling between (6) and (7), solutions for T_0 and q_0 must be obtained by use of iterative procedures (Sasamori 1970; McCumber and Pielke 1981; Camillo et al. 1983; Passerat de Silans et al. 1989). Due to frequent non-

convergence of these procedures when applied to these equations (Trembeck and Kessler 1985), most researchers have either simplified the terms in (6) and (7) to lessen their coupling or parameterized these equations. However, oversimplified or highly parameterized treatments restrict the conditions in which accurate simulations can be made (Deardorff et al. 1978; Mahouf and Noilhan 1991; Huang and Lyons 1995).

In S96, the Force-Restore (hereafter referred to as FR) prognostic equation for T_0 (Deardorff 1978) was used in place of (6), and the Penman-Monteith (Monteith 1981, hereafter referred to as PE) diagnostic equation for surface evaporation rate E_0 was used in place of (7). q_0 was then predicted from a flux divergence formulation using the surface layer specific humidity flux (computed using surface layer theory) and E_0. The main advantage of this approach is that it eliminates the need for a soil temperature and moisture transfer model to explicitly calculate H_G and W_0, for which initial soil temperature and moisture profiles are not routinely available.

In the FR scheme, H_G is parameterized by an assumed soil boundary layer depth, below which diurnal temperature changes are zero; a deep soil temperature equal to the average T_0 over the prior 24 hours; and the soil heat capacity. Because results are sensitive to the choice of these parameters (Grossi 1993), tuning is required to produce accurate results. The PE scheme was designed to describe evaporation from surfaces in which moisture is infinitely available, such as free water surfaces and certain vegetative covers. It uses measurements of near-surface air temperature and only crudely accounts for the energy available *at the surface* for evaporation (Monteith 1981). The scheme is

unsuitable for more common cases in which moisture availability is limited by the ability of the soil to supply moisture to the surface (Philip 1957; Sasamori 1970; Brutsaert 1982).

In the current T_0 and q_0 prediction scheme, (6) and (7) are represented as

$$0 = R_S + R_D - \epsilon_0 \sigma T_0^4 + \rho_0 c_p u_\star \theta_\star + \rho_0 L_E u_\star q_\star + \lambda(\eta_0) \frac{T_s(h_g) - T_0}{h_g} \tag{8}$$

$$0 = -\rho_0 u_\star q_\star - \left[\rho_w D_\eta(\eta_0) \frac{\eta(h_g) - \eta_0}{h_g} - \rho_w K_\eta(\eta_0) \right], \tag{9}$$

where (9) is formulated without precipitation. R_U is represented by the Stefan-Boltzman law, and H_S and H_L are expressed in terms of SBL theory, as explained in Section 2c. The last term on the right hand side of (8) and the bracketed term on the right hand side of (9) represent, respectively, H_G and W_0. They are formulated as forward finite-differenced representations (evaluated at the surface) of the following soil heat and moisture flux equations:

$$Q_S = -\lambda(\eta) \frac{\partial T_S}{\partial z} \tag{10}$$

$$W_S = -\rho_w \left[D_\eta(\eta) \frac{\partial \eta}{\partial z} - K_\eta(\eta) \right]. \tag{11}$$

In (10), only thermal heat conduction is considered, and latent heat transfer is neglected. The terms on the right hand side of (11) represent capillary movement and gravitational

settling of liquid water, respectively; additional terms that account for water vapor transfer and effects of soil temperature gradients are neglected. Details concerning the terms in (10) and (11), as well as justifications for neglecting terms, are found in Philip (1957).

Soil parameters λ, D_η, and K_η are dependent on soil moisture content. λ is calculated following Al Nakshabandi and Kohnke (1965) as

$$\lambda = \begin{cases} 419 \exp[-(P_f + 2.7)] & P_f \leq 5.1 \\ 0.172 & P_f > 5.1 \end{cases}, \tag{12}$$

where P_f is the base ten logarithm of the soil matrix potential ψ, a measure of the work necessary to move liquid water upward against tension forces that bind it to soil particles. D_η, K_η, and ψ are computed from the following empirical functions of Clapp and Hornberger (1978), hereafter CH:

$$D_\eta = -\frac{bK_{\eta_s}\psi_s}{\eta}\left(\frac{\eta}{\eta_s}\right)^{b+3} \tag{13a}$$

$$K_\eta = -K_{\eta_s}\left(\frac{\eta}{\eta_s}\right)^{2b+3} \tag{13b}$$

$$\psi = \psi_s\left(\frac{\eta}{\eta_s}\right)^{-b}, \tag{13c}$$

where values at saturation (denoted by subscript s) and exponent b are constants

dependent on soil type. To prevent excessive, unrealistic surface drying during the day, a minimum value for D_η of 10^{-9} m^2s^{-1} is imposed.

$T_s(h_g)$ and $\eta(h_g)$ are computed from a multilevel model that solves the following conservation equations for heat and moisture transfer, respectively, within the soil:

$$C_s \frac{\partial T_s}{\partial t} = - \frac{\partial Q_s}{\partial z_s} \tag{14}$$

$$\frac{\partial \eta}{\partial t} = - \frac{\partial W_s}{\partial z_s} \ , \tag{15}$$

where Q_s and W_s are computed from (10) and (11), respectively, and C_s is computed as the following weighted sum of the heat capacities of dry soil and liquid water:

$$C_s = (1 - \eta_s) C_d + \eta C_w \ . \tag{16}$$

Equations (14) and (15) are solved using a backward implicit differencing scheme, with T_s, η, and C_s located at the midpoint between grid levels, and λ, D_η, and K_η located at grid levels. The latter three parameters are calculated from (13a-c) using the average of η within the two adjacent grid layers. T_s and η within the bottom soil layer are held fixed.

Equations (8) and (9) are in the three unknowns, T_o, q_o (through q_*), and η_o. To reduce the number of unknowns, the atmospheric moisture flux in (9) is replaced with (24), (26), and (31) (described in Section 2c) to yield

$$0 = -C[q(3h/2) - q_0 - C'] - \left[\rho_w D_\eta(\eta_0)\frac{\eta(h_g) - \eta_0}{h_g} - \rho_w K_\eta(\eta_0)\right].$$

Functions C and C' are defined as

$$C = \frac{\rho u_\star k}{\phi_h(h) + \int_{z_0}^{h/2}\frac{\phi_h}{z}dz}$$

$$C' = \frac{q_\star}{k}\ln\left(\frac{z_0}{z_q}\right),$$

with values of $u_\star$ and $q_\star$ from the previous time step. The surface wetness function of Mihailovic et al. (1995),

$$\alpha \equiv \frac{q_0}{q_s(T_0)} = 1 - \left(\frac{\eta_{fc} - \eta}{\eta_{fc}}\right), \tag{17}$$

is then used for q_0 to yield

$$\begin{aligned} 0 = -C\left\{q(3h/2) - q_s(T_0)\left[1 - \left(\frac{\eta_{fc} - \eta_0}{\eta_{fc}}\right)\right] - C'\right\} \\ - \left[\rho_w D_\eta(\eta_0)\frac{\eta(h_g) - \eta_0}{h_g} - \rho_w K_\eta(\eta_0)\right]. \end{aligned} \tag{18}$$

Equations (8) and (18) represent two coupled expressions (for unknowns T_o and η_o) that are solved iteratively at each time step. Letting n equal the nth iteration in the procedure, and initially setting values at n-1 to those at the previous time step, the iteration proceeds as follows:

1. Using $T_0(n-1)$, solve (18) by a single iterative Newton-Raphson scheme to give $\eta_0(n)$, and use it in (11) and (13a,b) to evaluate $W_0(n)$, and in (13c) to evaluate $\lambda(n)$ from (12).
2. Evaluate $q_0(n)$ from $\eta_0(n)$ and (17), and use it in (24), (26), and (31) to evaluate $E_0(n)$ and $H_L(n)$.
3. Solve (8) by a single iterative Newton Raphson scheme using $H_L(n)$ and $H_S(n-1)$ to give $T_0(n)$, and use it in (10) to evaluate $H_G(n)$.
4. Use $T_0(n)$ in Poisson's equation to evaluate $\theta_0(n)$ for use in (33), (34b), and (38) to evaluate $H_S(n)$.
5. Compute $|H_S(n) - H_S(n-1)|$. If this is greater than ~ 1Wm^{-2}, set $T_0(n-1) = T_0(n)$ and repeat Steps (1)-(5). If less than 1Wm^{-2}, the procedure is completed resulting in final values of T_0, q_0, η_0, H_S, H_L, H_G, E_0, and W_0 at the current time step.

In application of the above iterative procedure, (18) sometimes does not converge. Non-convergence is associated with sharp second derivatives of (18) with respect to η_o during periods of rapid surface drying or moistening (usually during late-morning

and late-afternoon). The Newton-Raphson successive correction term (which makes use of the function and its *first* derivative) can be excessively large during these periods, and can lead to negative values of η_o during the iterative process. The absolute value of the correction term is thus bounded to be less than 0.05 cm^3cm^{-3} during iteration of (18). Remaining instances in which convergence was not obtained were corrected by reducing h_g; a value of 1 mm has thus far ensured convergence.

Linkage between q_* and η_o at the surface is achieved by (17). This function expresses a rapid decrease in available moisture for evaporation as η_o drops below the field capacity η_{fc}, below which soil moisture can be held in soil pores against gravity (Lee and Pielke 1992). This equation is one of several empirical formulations describing this process developed to replace the traditionally used Philip (1957) equation, which is invalid at the surface (Wetzel and Chang 1987; Kondo et al. 1990; Lee and Pielke 1992). These empirical formulations appear as α or β in the literature. As described by Mahouf and Noilhan (1991), α expresses the moisture transfer between the *surface* and atmosphere, while β expresses the moisture transfer between the *air over the free water surface within the surface soil pores* and the atmosphere. The β method is thus conceptually more difficult to implement, and has been shown to underestimate nocturnal condensation rates (Mahouf and Noilhan 1991; Mihailovic et al. 1995). An α formulation is thus preferred, and (17) is currently used, due to its ease of use and accuracy (Mihailovic et al. 1995).

c. Surface boundary layer

In numerical models of the atmosphere, the layer adjacent to the surface cannot be modeled using finite differencing approximations (Taylor and Delage 1971). Analytic formulations describing the vertical structure of mean and turbulent quantities within the surface boundary layer (SBL) are thus used to provide the lower boundary conditions for the numerical computations of variables above the SBL. The most commonly used formulations are those derived from Monin-Obukhov (MO) similarity theory (see review of Garratt 1992), in which turbulent fluxes are assumed constant with height, and the vertical structures of V, θ, and q are described, respectively, by

$$\frac{\partial V}{\partial z} = \frac{u_\star}{kz}\phi_m \tag{19}$$

$$\frac{\partial \theta}{\partial z} = \frac{\theta_\star}{kz}\phi_h \tag{20}$$

$$\frac{\partial q}{\partial z} = \frac{q_\star}{kz}\phi_q \,. \tag{21}$$

Non-dimensional gradients ϕ_m, ϕ_h, and ϕ_q are experimentally determined functions of stability parameter $\zeta = z/L$, where Monin-Obukhov length L is given by

$$L = \frac{u_\star^2 \theta_a}{gk\theta_\star} \,.$$

Through integration of (19)-(21), both surface fluxes of momentum, heat, and moisture, and SBL values of V, θ, and q are computed.

Previous TVM treatment of the SBL employed MO similarity theory, with ϕ_m, ϕ_h, and ϕ_q taken from Businger et al. (1971) for unstable conditions and from Webb (1970) for stable conditions. This treatment, however, is not reflective of recent refinements to SBL and MO similarity theories. For example, roughness lengths for momentum, heat, and humidity in S96 are assumed equal, although this has been shown to be false (e.g., Garratt and Francey 1978; Brutsaert 1982; Garratt 1992; Blyth 1992). Also, more recent determinations of ϕ_m, ϕ_h, and ϕ_q make use of data over a wider range of stabilities than that used to develop previous formulations. The SBL treatment was therefore modified to account for these various corrections and improvements.

Computation of SBL fluxes and mean variables requires evaluation of u_*, θ_*, and q_*, usually accomplished through integration of (19)-(21) from aerodynamic roughness length z_0 to the first model level above the ground, denoted by h. However, in order to maintain consistency between analytically computed variables below h and those computed by finite-difference above h, the integration is performed with the constraint that analytic and numerical derivatives are matched at h. Assuming that the first two model levels are equally spaced gives the following:

$$\left.\frac{\partial V}{\partial z}\right|_{h} = \frac{u_\star}{kh}\phi_m(h/L) = \frac{V(3h/2) - V(h/2)}{h}$$

$$\left.\frac{\partial \theta}{\partial z}\right|_{h} = \frac{\theta_\star}{kh}\phi_h(h/L) = \frac{\theta(3h/2) - \theta(h/2)}{h}$$

$$\left.\frac{\partial q}{\partial z}\right|_{h} = \frac{q_\star}{kh}\phi_q(h/L) = \frac{q(3h/2) - q(h/2)}{h} .$$

Integration of (19)-(21) to express variables at $h/2$ yields

$$\frac{u_\star}{kh}\phi_m(h/L) = \frac{V(3h/2) - \frac{u_\star}{k}\int_{z_0}^{h/2}\frac{\phi_m}{z}dz}{h}$$

$$\frac{\theta_\star}{kh}\phi_h(h/L) = \frac{\theta(3h/2) - \left[\theta(z_0) + \frac{\theta_\star}{k}\int_{z_0}^{h/2}\frac{\phi_h}{z}dz\right]}{h}$$

$$\frac{q_\star}{kh}\phi_q(h/L) = \frac{q(3h/2) - \left[q(z_0) + \frac{q_\star}{k}\int_{z_0}^{h/2}\frac{\phi_q}{z}dz\right]}{h} ,$$

which when rearranged give the following expressions for $(\,)_\star$ quantities:

$$u_\star = \frac{kV(3h/2)}{\phi_m(h/L) + \int_{z_0}^{h/2} \frac{\phi_m}{z} dz} \tag{22}$$

$$\theta_\star = \frac{k[\theta(3h/2) - \theta(z_0)]}{\phi_h(h/L) + \int_{z_0}^{h/2} \frac{\phi_h}{z} dz} \tag{23}$$

$$q_\star = \frac{k[q(3h/2) - q(z_0)]}{\phi_q(h/L) + \int_{z_0}^{h/2} \frac{\phi_q}{z} dz} . \tag{24}$$

$\theta(z_0)$ and $q(z_0)$ are evaluated as

$$\theta(z_0) = \theta_0 + \frac{\theta_\star}{k} \ln\left(\frac{z_0}{z_\theta}\right) \tag{25}$$

$$q(z_0) = q_0 + \frac{q_\star}{k} \ln\left(\frac{z_0}{z_q}\right) , \tag{26}$$

where thermal and humidity roughness lengths z_θ and z_q are each assumed equal to $0.10z_0$ (Garratt and Francey 1978), θ_o and q_o are evaluated as discussed in Section 2b, and values of $\theta_\star$ and $q_\star$ at the previous time step are used. Equations (25) and (26) were derived by matching profile relationships for the roughness sublayer and SBL at the roughness sublayer height (Brutsaert 1982). They replace the commonly used Zilitinkevich (1970) equations, valid only for aerodynamically smooth flow.

The MO similarity functions of Businger et al. (1971) for unstable conditions are retained

$$\phi_m = (1 - \gamma_m \zeta)^{-1/4} \tag{27a}$$

$$\phi_h = \phi_q = (1 - \gamma_h \zeta)^{-1/2}, \tag{27b}$$

where the values of γ_m and γ_h (see Appendix) reflect the change of k from the Businger et al. (1971) value of 0.35 to 0.40 (Högstrom 1988). Formulations for ϕ_m and ϕ_h in stable conditions, from Beljaars and Holtslag (1991), are given as

$$\phi_m = 1 + \beta_1 \zeta + (1 + \beta_3 - \beta_4 \zeta)\, \beta_2 \zeta \exp(-\beta_4 \zeta) \tag{28a}$$

$$\phi_h = \phi_q = 1 - \beta_1 \zeta \sqrt{1 + 0.667 \beta_1 \zeta} + (1 + \beta_3 - \beta_4 \zeta)\, \beta_2 \zeta \exp(-\beta_4 \zeta)\ . \tag{28b}$$

These functions are modifications of those derived by Holtslag and DeBruin (1988), and are consistent with a theoretical upper limit of the flux Richardson number of 1.0. They fit the functions of Carson and Richards (1978), who used data from Hicks (1976) to develop three separate formulations for different stability ranges. Whereas the Webb (1970) function (used in S96) discontinuously describes a transition from a log-linear to logarithmic profile shape at $\zeta = 1$, (37a,b) give a continuous transition from log-linear to *nearly* logarithmic at $\zeta \sim 0.5$, and back to nearly log-linear at $\zeta = 5$ (Fig. 12). Physically,

the approach from log-linear to nearly logarithmic describes the inability of the SBL to establish a laminar state (i.e., a purely linear profile), due to intermittent generation of turbulence when the flux Richardson number is beyond its limiting value (~ 0.25) for continuous turbulence (Carson and Richards 1978).

Since determination of u_*, θ_*, and q_* involves evaluation of ϕ_m and ϕ_h, in turn functions of u_* and θ_* through L, (22)-(24) are solved iteratively. A first-guess value of L, based on u_* and θ_* from the previous time step, is initially used to evaluate (22)-(24). L is then recomputed based on updated values of u_* and θ_*. If the absolute difference between the new and updated values of $L^{-1} > 5.0 \times 10^{-3}$, (22)-(24) are re-evaluated using the new value of L. This process is repeated until $L^{-1} \leq 5.0 \times 10^{-3}$, which generally occurs in less than three iterations.

Values of u_*, θ_*, and q_* are used to compute SBL momentum, heat, and moisture fluxes as

$$M_0 = -\rho u_*^2 \tag{29}$$

$$H_S = -\rho c_p u_* \theta_* \tag{30}$$

$$E_0 = -\rho u_* q_* \ , \tag{31}$$

and SBL eddy diffusivities as

$$K_m = \frac{u_\star l_{sbl}}{\Phi_m} \tag{32a}$$

$$K_h = K_q = \frac{u_\star l_{sbl}}{\Phi_h} , \tag{32b}$$

with

$$l_{sbl} = kz . \tag{33}$$

These are then inserted into (19)-(21) to solve for V, θ, and q at locations between the surface and h. Zonal and meridional components of velocity u and v are calculated assuming wind direction is invariant with height within the SBL, with a value equal to that at the first finite-differenced level above h.

TKE is assumed constant with height within the SBL, and was evaluated in S96 as $4u_\star^2$ for all stabilities. Whereas sole dependence on $u_\star$ is valid for predominantly mechanically produced TKE during stable conditions, it is invalid during unstable conditions, when buoyancy also generates TKE. The formulation is thus changed to the following:

$$e(h) = \begin{cases} \dfrac{[A_1^2 + A_2^2 + A_3^2]u_\star^2}{2} , & \zeta \geq 0 \\ \dfrac{[A_1^2 + A_2^2 + A_3^2(1-3\zeta)^{2/3}]u_\star^2}{2} , & \zeta < 0 . \end{cases} \tag{34}$$

These equations are derived by summing horizontal and vertical components of momentum variance and dividing by two, consistent with the definition of TKE. The first two terms in the numerator of both right hand sides of (34) represent horizontal variance components, while the third terms represent the vertical components.

Horizontal variances in (34) are from Kader and Yaglom (1990), and retain u_* scaling for both stable and unstable conditions. Although it is well-known that SBL horizontal variances scale with free convective scale velocity w_* during unstable conditions (Businger 1973; Panofsky et al. 1977), results from recent field studies (e.g. Kader and Yaglom 1990) have produced uncertainty concerning the validity of previously derived scaling constants. Furthermore, w_* scaling would be inconsistent with the model turbulence parameterization above the SBL (discussed in Section 2d), which does not account for the semi-coherent, buoyantly driven plumes that give rise to the w_* scaling. Free convective velocity scaling for horizontal variances is thus, for now, not included.

Vertical variances in (34) for stable and unstable conditions are from Kader and Yaglom (1990) and Panofsky et al. (1977), respectively. The term in the unstable formulation accounts for the predominance of buoyant production of vertical TKE during such conditions.

d. PBL turbulence

Whereas the SBL is modeled using analytic expressions for mean meteorological variables and turbulent quantities, the rest of the PBL is modeled through finite-difference approximation of the dynamic and thermodynamic Reynolds averaged conservation equations. Included in these equations are terms involving divergences of second order turbulent correlations of velocity and appropriate mean meteorological parameter A, which must be parameterized. The most common parameterization is to express these correlations as the negative product of the mean gradient of A and an eddy diffusivity K_A, which for correlation with the vertical component of turbulent velocity is given by

$$\overline{w'A'} = -K_A \frac{\partial A}{\partial z} . \tag{35}$$

Correlations with horizontal components of turbulent velocity in general have far less significant effects on meteorological fields than those with vertical turbulent velocity, and are therefore not discussed.

The current study employs K-e closure, where K_A is related to TKE by

$$K_A = C_A l_k \sqrt{e} . \tag{36}$$

TKE is solved prognostically from

$$\frac{\partial e}{\partial t} = K_m \left[\left(\frac{\partial u}{\partial z} \right)^2 + \left(\frac{\partial v}{\partial z} \right)^2 \right] - \frac{g}{\theta_a} K_h \frac{\partial \theta}{\partial z} - C_\epsilon \frac{e^{3/2}}{l_\epsilon} + \frac{\partial}{\partial z} \left(K_e \frac{\partial e}{\partial z} \right) , \tag{37}$$

where the terms on the right hand side represent, respectively, shear production, buoyancy production, molecular dissipation, and the combination of turbulent transport and pressure redistribution of TKE. Closure of model equations thus reduces to specification of turbulent length scales l_k and l_ϵ, and constant C_A.

S96 utilized the following algebraic expressions of TL for l_k and l_ϵ

$$\frac{1}{l_k} = \frac{1}{l_{sbl}} + \frac{C_{1k}}{h_i} - \left(\frac{1}{l_{sbl}} + \frac{C_{2k}}{h_i} \right) m_{1k} m_{2k} + \frac{C_{5k}}{l_s} \tag{38a}$$

$$\frac{1}{l_\epsilon} = \frac{1}{l_{sbl}} + \frac{C_{1\epsilon}}{h_i} - \left(\frac{1}{l_{sbl}} + \frac{C_{2\epsilon}}{h_i} \right) m_{1\epsilon} m_{2\epsilon} + \frac{C_{5\epsilon}}{l_s} , \tag{38b}$$

with factors m given as

$$m_{1k} = \frac{1}{1 + C_{3k} \dfrac{h_i}{l_{sbl}}}$$

$$m_{1\epsilon} = \frac{1}{1 + C_{3\epsilon} \dfrac{h_i}{l_{sbl}}}$$

$$m_{2k} = \begin{cases} \dfrac{1}{1 - C_{4k} \dfrac{L}{h_i}} , & L < 0 \\ 0 , & L \geq 0 \end{cases}$$

$$m_{2\epsilon} = \begin{cases} \dfrac{1}{1 - C_{4\epsilon}\dfrac{L}{h_i}} & , \quad L < 0 \\ 0 & , \quad L \geq 0 \end{cases} .$$

The first two terms on the right hand sides of (38a,b) represent interpolation between the SBL and free atmospheric length scales, while the last two represent corrections for unstable and stable conditions, respectively. The correction for stable conditions is represented by length scale l_s, given by

$$\frac{1}{l_s} = \begin{cases} 0 & , \quad \dfrac{\partial\theta}{\partial z} \leq 0 \\ \sqrt{\dfrac{g\partial\theta/\partial z}{\theta_a e}} & , \quad \dfrac{\partial\theta}{\partial z} > 0 \end{cases} . \tag{39}$$

In S96, h_i was defined during unstable conditions as the height at which e is 10% of its surface value, while during stable conditions it was computed as $0.3u_*/f$.

Equations (38a,b) were designed primarily for the CBL, for which they were shown by TL to properly capture many properties of daytime convective mixing when compared with field studies and HOTC model results. Current application of (38a,b) to a wide variety of *nighttime* conditions (e.g., fast/slow winds, high/low surface cooling rates), however, resulted in immediate elimination of TKE throughout the PBL shortly after evening transition, with lack of later regeneration in appropriate regions within the PBL. While an abrupt decrease in TKE at evening transition is expected (Fig. 11a,b), its

complete temporal and spatial elimination is suspicious. Specifically, nighttime TKE is expected to be maintained and/or regenerated within the surface driven nocturnal boundary layer (NBL), where shear production is strong, and within portions of the residual layer (RL) aloft, characterized by the remnant effects of daytime mixing.

Erroneous elimination of TKE within the RL was found due to the representation of free atmospheric length scale l_∞ [second term on the right-hand side of in (38a,b)], which is expressed in terms of h_i. This representation is invalid in nocturnal conditions, when h_i (representive of the NBL height) does not denote the lower boundary of the free atmosphere, but rather the lower boundary of the RL. To more accurately compute l_∞ during stable conditions, the Blackadar (1962) expression

$$\frac{1}{l_\infty} = \alpha_0 \frac{\int_0^{\bar{z}} \sqrt{e}\, z dz}{\int_0^{\bar{z}} \sqrt{e}\, dz} \tag{40}$$

is used, where $\alpha_o = 0.10$. Because (40) involves vertical integration throughout the model domain, which includes the NBL and RL, a more accurate representation of l_∞ is obtained, in turn leading to a better description of processes governing TKE production within the RL.

The lack of TKE generation within the NBL was found to result from a discontinuity in K_A at h. This resulted from inequality of l_{sbl} and l_k at $z = h$, which at evening transition led to a much larger value of K_A at h [computed by using (33) for l_{sbl} in (32a,b)] than at the adjacent layer above h [computed by using (38a) for l_k in the appropriate form of (36)]. Subsequent large positive stress divergences within the first layer above h

sequentially caused: strong deceleration of V within the layer, weaker values of u_* from (22), and eventually negligible TKE values in the SBL from (34), and throughout the NBL from (37).

To link l_k and K_A at h, separate SBL length scales for momentum and heat are defined as

$$l_{sbl}^{m} = \frac{kz}{\Phi_m} \tag{41a}$$

$$l_{sbl}^{h} = \frac{kz}{\Phi_h} \,. \tag{41b}$$

The inclusion of ϕ_m and ϕ_h in these definitions was proposed by Yu (1978) as a stability correction to the Prandtl length scale kz. Equations (38a,b), (40), and (41a,b) are then used to derive expressions for turbulent length scales matched at h, which for unstable SBL conditions ($\zeta < 0$) are given by

$$\frac{1}{l_m} = \frac{1}{l_{sbl}^{m}} + \chi \left[\frac{C_{1k}}{h_i} - \left(\frac{1}{l_{sbl}^{m}} + \frac{C_{2k}}{h_i} \right) m_{1m} m_{2k} + \frac{C_{5k}}{l_s} \right] \tag{42}$$

$$\frac{1}{l_h} = \frac{1}{l_{sbl}^{h}} + \chi \left[\frac{C_{1k}}{h_i} - \left(\frac{1}{l_{sbl}^{h}} + \frac{C_{2k}}{h_i} \right) m_{1h} m_{2k} + \frac{C_{5k}}{l_s} \right] \tag{43}$$

$$\frac{1}{l_\epsilon} = \frac{1}{l_{sbl}^{m}} + \chi \left| \frac{C_{1\epsilon}}{h_i} - \left(\frac{1}{l_{sbl}^{m}} + \frac{C_{2\epsilon}}{h_i} \right) m_{1m} m_{2\epsilon} + \frac{C_{5\epsilon}}{l_s} \right| , \tag{44}$$

where m_{lm} and m_{lh} are factors for momentum and heat, respectively, analogous to m_{lk}. For stable and neutral SBL conditions ($\zeta \geq 0$), length scales are given by

$$\frac{1}{l_m} = \frac{1}{l_{sbl}^m} + \chi\left[\frac{1}{l_\infty} + \frac{C_{sk}}{l_s}\right] \tag{45}$$

$$\frac{1}{l_h} = \frac{1}{l_{sbl}^h} + \chi\left[\frac{1}{l_\infty} + \frac{C_{sk}}{l_s}\right] \tag{46}$$

$$\frac{1}{l_\epsilon} = \frac{1}{l_{sbl}^m} + \chi\left[\frac{1}{l_\infty} + \frac{C_{s\epsilon}}{l_s}\right], \tag{47}$$

where l_∞ is computed from (40). Note that due to the inequality of ϕ_m and ϕ_h [see (27a,b) and (28a,b)], separate equations for l_m and l_h are produced. This distinction is not present in (38a,b).

The scaling factor χ in (42)-(47) is arbitrarily defined as

$$\chi = \begin{cases} \dfrac{z-h}{\tilde{z}-h} & , \quad z \leq \tilde{z} \\ 1 & , \quad z > \tilde{z} \ , \end{cases} \tag{48}$$

which, because $\chi = 0$ at h, allows for equality between SBL and PBL length scales at this level. $\tilde{z}$ is set to $0.10h$, roughly the SBL depth. For $\zeta \geq 0$, however, a lower bound on $\tilde{z}$ of ~ 40 m is implemented to ensure that an appreciable number of grid levels (at least 3) are influenced by the imposed continuity constraint. This bound is necessary due to

course model resolution of the NBL, i.e. at night h (~ 10 m) can often be greater than $0.10h_t$.

PBL height h_t, needed in (42)-(44) and (48), is now defined as the lowest height above which TKE is less than 1% of the surface value. This ensures that h_t is reflective of the depth of the surface driven turbulent layer, corresponding to the CBL during the day and to the NBL at night. For $\zeta < 0$, h_t is bounded by the base of the any elevated stable layer. This allows for a precise treatment of the CBL, as scaling of turbulent energy and fluxes with h_t ceases above the base of the elevated stable layer.

Using the representations for length scales given above, formulations for K_A within the SBL [given by (32a,b)] and within the remaining part of the PBL [given by appropriate forms of (36)] are equated at h to yield:

$$C_A l_m(h)\sqrt{e(h)} = u_\star l_{sbl}^m(h)$$

$$C_A l_h(h)\sqrt{e(h)} = u_\star l_{sbl}^h(h)\,,$$

which results in the following expression for C_A

$$C_A = \frac{u_\star}{\sqrt{e(h)}}\,. \tag{49}$$

This, together with l_m and l_h from (42)-(47), are then used to evaluate (36), giving values for K_m and K_h throughout the PBL. With the assumptions that $K_q = K_h$, and $K_e = 1.20K_m$, where the constant 1.20 accounts for pressure redistribution terms implied in the last term on the right-hand side of (37), the model equations are closed.

3. MODEL SETUP

The period simulated in the current W33 modeling study was 0600 LST Day 33 to 1200 LST Day 34 (17-18 Aug. 1967). Nearly all previous W33 simulations started at 0900 LST Day 33 (Tables 1 and 2). This is inconvenient, however, as the PBL is non-stationary at this time, making initialization of TKE difficult. Since the PBL is largely stationary near sunrise, initialization at 0600 LST is less difficult.

The model grid consisted of 51 atmospheric levels and 17 soil levels with spacings stretched to obtain highest resolution near the surface (Table 3). Atmospheric variables are staggered within grid layers, with u, v, θ and q held at the midpoint between grid levels; and TKE, vorticity components, and turbulent fluxes of momentum, heat, and moisture held on grid levels.

Surface and soil parameters are shown in Table 4. Aerodynamic roughness z_0 was chosen as 1 cm, a representative value for the Wangara site (Clarke et al. 1971; Hicks 1981). Soil parameters K_s, b, and η_s are mean values obtained by CH for a loam soil, the predominant type in the Wangara region. The value for ψ_s, however, is the modal value obtained by CH. Considerable skewness was obtained in CH measurements of ψ_s, and the modal rather than mean value was chosen so that a value representative of a "typical" loam soil was used in the simulation. C_t and η_{fc} were taken from Pielke (1984) and Lee and Pielke (1992), respectively, for a loam soil.

Table 3. Atmospheric (z) and soil (z_s) grid levels

Level	z(m)	z_s(cm)
1	0	0.0
2	10	0.2
3	20	0.5
4	31	1.2
5	43	2.0
6	55	3.1
7	68	4.5
8	81	6.4
9	95	8.8
10	110	11.9
11	126	16.0
12	142	21.3
13	159	28.2
14	177	37.2
15	196	48.8
16	216	64.0
17	237	83.9
.	.	
.	.	
37	958	
38	1016	
39	1077	
40	1141	
41	1208	
.	.	
.	.	
.	.	
51	2093	

Table 4. Surface and soil parameters

Parameter [1]	Value
z_0 (cm)	1.00
ϵ_0	0.90
C_d (J m^{-3} K^{-1})	1.21×10^{5}
η_s (cm^3 cm^{-3})	0.451
η_{fc} (cm^3 cm^{-3})	0.240
K_s (cm s^{-1})	7.00×10^{-4}
ψ_s (cm)	-14.70
b	5.39

[1] See Appendix for definition of symbols

Time and height varying geostrophic winds (Fig. 2) were defined by interpolation of measured surface geostrophic, and 0-1 and 1-2 km thermal winds, as described in Section 1. While surface geostrophic wind values are accurate, thermal wind values are not accurate due to the wide separation of the upper air observations used in their derivation. Later attempts to derive more accurate thermal winds (Hess et al. 1981) did not yield significantly more accurate values than those originally reported in Clarke et al. (1971). For convenience, the originally reported thermal winds were thus used to determine the time/height variation of the geostrophic wind. Potential temperature advection consistent with the thermal winds was not included.

From the time/height cross-sections of observed meteorological variables, and based on the overprediction of h, in the AN simulation (Fig. 3a,b), it is believed that large-scale subsidence was an important factor in the determination of PBL structure throughout the W33 period. However, since experimental determinations of vertical velocity are known to be inaccurate (Hess et al. 1981), these vertical velocities were not used. Instead a steady state parabolic profile was defined by setting w_s to zero at the surface and at 100 mb, and to a value of -0.5 cm s^{-1} at 600 mb. A parabolic profile is qualitatively consistent with lower-level divergence compensating upper-level convergence, giving rise to negative vertical velocity (Hess 1978). The 600 mb value was chosen from qualitative inspection of upper-level large scale maps of geopotential height for the W33 period. The imposed w_s was used to calculate large-scale vertical advection through

$$\left(\frac{\partial A}{\partial t}\right)_s = -\frac{\partial(w_s A)}{\partial z} + A\frac{\partial w_s}{\partial z} \quad . \tag{50}$$

The last term of (50) represents large-scale horizontal divergence (convergence) needed to balance vertical convergence (divergence) implied in the previous term (so that the imposed w_s obeys continuity). Without this term, erroneous generation (decay) of A at the bottom (top) of the tropopause results.

Initial values of u and v were defined as the weighted average of interpolated and geostrophic values as

$$u = \chi' u_i + (1-\chi') u_g$$
$$v = \chi' v_i + (1-\chi') v_g \quad ,$$

where χ' equals one below 1400 m, and then decreases linearly to zero at z_T. Interpolated values (denoted by subscript i) were defined by cubic spline interpolation of observed 0600 LST values, smoothed by five-point weighted averaging. The adjustment towards geostrophic values above 1400 m ensures an initially smooth transition to the geostrophic upper boundary condition on u and v.

Initial values of θ and q were defined by cubic spline interpolation 0600 LST observations. The slightly superadiabatic layer between 500-700 m resulting from the interpolation was reset to a slightly stable profile consistent with the model formulation, which neglects horizontal advection, and tends to produce slightly stable stratification

within this region throughout the night due to differential radiative cooling. TKE was initially set to zero at all grid levels.

The initial T_s profile (Table 5) was defined by assuming $(\partial T_s/\partial z_s)_0$ decreases exponentially with depth, i.e.

$$\frac{\partial T_s}{\partial z_s} = \left(\frac{\partial T_s}{\partial z_s}\right)_0 e^{-b' z_s} .$$

After integration from the surface to z_s, the following equation for initial T_s values is derived:

$$T_s(z_s) = T_0 + \frac{1}{b'}\left(\frac{\partial T_s}{\partial z_s}\right)_0 [1 - e^{-b' z_s}] . \qquad (51)$$

The initial surface soil temperature gradient $(\partial T_s/\partial z_s)_0$ was specified to match the 0600 LST observations of H_G (Clarke et al. 1971), and b' was set so (51) equals the specified constant temperature at the bottom soil layer.

The initial η profile (Table 5) was generated from the final results of a 24 hour simulation, initialized at 0600 LST with an initial depth-invariant value of η of 0.125 cm^3 cm^{-3}. This value is less than the wilting point (loam, 0.155 cm^3 cm^{-3}), commonly used value to initialize dry bare soil. However, since the Wangara region was affected by drought preceding the experiment, and because it had not rained for a week leading up to Days 33-34, the soil was likely dryer than the wilting point. The initial η profile

Table 5. Initial values for soil temperature (T_s) and moisture (η_s)

Level	z_s (cm)	T_s (K)	η_s ($cm^3\ cm^{-3}$)
1	0.00	272.42	0.117
2	0.10	272.48	0.111
3	0.35	272.63	0.086
4	0.85	272.92	0.092
5	1.60	273.35	0.115
6	2.55	273.86	0.124
7	3.80	274.49	0.125
.	.	.	.
.	.	.	.
.	.	.	.
12	18.65	279.30	0.125
.	.	.	.
.	.	.	.
.	.	.	.
14	32.70	281.23	0.125
.	.	.	.
.	.	.	.
.	.	.	.
17	73.95	283.57	0.125

generated in this manner exhibits common early morning structure in the upper 2 cm of the soil.

Given the above initial conditions and internal forcings, the model was run for one simulated hour with: (a) T_0, q_0, T_s, η held constant, (b) the large-scale geostrophic wind held constant, (c) no radiative flux divergence, and (d) no w_s, to generate realistic, consistent initial values for variables (primarily TKE) within the model atmospheric domain. The main time varying simulation then proceeded with a time step of 30 s.

Time varying upper boundary conditions on u and v were defined equal to their respective time varying observed geostrophic values. Within the model domain, u and v were similarly adjusted towards their geostrophic values at each time step by

$$\frac{\partial u}{\partial t} = (1-\chi')\left(\frac{\partial u_g}{\partial t}\right)$$

$$\frac{\partial v}{\partial t} = (1-\chi')\left(\frac{\partial v_g}{\partial t}\right) ,$$

where χ' is defined as described above. Time varying upper boundary conditions on θ and q were assumed due to subsidence, and computed from (50) with θ and q above z_T defined by extrapolation as described in Section 2a. TKE at z_T was set to zero. Bottom soil layer values for T_s and η were held fixed at their initial values.

4. RESULTS

Before discussing the predicted daytime and nighttime W33 vertical and temporal PBL structure, evaluation of the predicted surface forcing is necessary. Observed and simulated 1.2 m temperature $T_{1.2}$, 1.2 m specific humidity $q_{1.2}$, and 16 m wind speed V_{16} (Fig. 13a-c) are in qualitative agreement. The most obvious discrepancies are the overprediction of daytime $q_{1.2}$, and underpredictions of $T_{1.2}$ and $q_{1.2}$ during the evening. The former is attributed to overprediction of surface specific humidity flux, and the latter to horizontal advective effects, absent in the simulation, which strongly characterized the observed nighttime W33 PBL structure. Further discussion of these accuracies is given later in this section.

Comparison of observed and simulated surface heat fluxes is made difficult, as only R_N and H_G were directly measured during the experiment. H_S was later computed by Hicks (1981) from observed 1 to 4 m temperature and wind speed differences using SBL profile laws and similarity functions (similar to those in Section 2c), with H_L computed as the residual of R_N, H_G, and H_S. This method, however, is less accurate than methods that employ direct flux measurements with eddy correlation equipment (Stull 1988). Although the error in Hicks' method was small during the moderately convective first 10 days of the experiment (when eddy correlation measurements were available for comparison; Hicks 1981), the accuracy of the method in free convective conditions

present during Day 33 is unproven. Nonetheless, simulated heat fluxes will be compared with this set of "observed" fluxes.

Inspection of observed and predicted surface heat fluxes (Fig. 14a,b) shows that most qualitative features are captured. For example, the value and time of daytime peaks of R_N and H_s are matched, and the value of flux components during the night are ordered from smallest to largest consistent with observations. The most noticeable discrepancy is for daytime H_L. While the simulation produces a peak value of ~ 50 Wm^{-2} (consistent with specifications in previous W33 modeling studies, as discussed in Section 1), Hicks (1981) values are slightly negative implying surface condensation. Such a phenomenon is unlikely during the day, when surface heating promotes evaporation. However, overprediction of H_L, and hence E_0, is consistent with daytime overprediction of $q_{1.2}$ (Fig. 13b). It is thus believed that H_L and E_0 are overpredicted, although not to the extent implied by the discrepancy between Hicks' and simulated H_L.

Observed and simulated u_* (Fig. 15) show good agreement during the day and overprediction during the night. The observations were derived by Hicks (1981) from 1 to 4 m wind speed differences, yet modeled values were computed from 15 m winds. As this latter level is above the likely nighttime SBL depth of 5-10 m (approximating the SBL depth as $0.10h_i$; see Fig. 36), modeled values may not be representative of nighttime SBL values.

Modeled time/height cross-sections of T_s and η (Fig. 16a,b) show typical decreased wave amplitudes and increased phase lags with soil depth. Whereas the depth

of diurnal change of T_s is ~ 40 cm, the corresponding depth for η is only ~ 1 cm. This feature, also found by Sasamori (1970), is due to the inefficiency of upward hydraulic capillary movement relative to thermal conduction within dry soil.

a. Daytime PBL structure

Vertical profiles of observed and simulated daytime θ_v (Fig. 17a,b) show typical CBL development, as described in Section 1. Two discrepancies between observed and simulated profiles are noticed: mixed layer θ_v is underpredicted by ~1 °C throughout most of the daytime period, and simulated mixed layer afternoon profiles are superadiabatic, instead of adiabatic as observed and simulated by AN (Fig. 3b).

Underprediction of mixed-layer θ_v is interesting given its apparent accurate prediction in previous W33 modeling studies. However, most previous studies did not include RFD in their daytime calculations. Turbulent and radiative heating rates for 1200 LST (Fig. 18) show a mixed layer radiative cooling rate of ~ 0.15 K hr^{-1}, which projected over the entire well-mixed period (~ 6 hours) gives total cooling comparable to the discrepancy between the current model results and both observations and results of previous modeling studies. Profiles of θ_v (Fig. 19) for a run without RFD and w_s (the latter omitted to better compare with AN) show mixed layer values in agreement with observations and AN. Since radiative cooling of the above magnitude is typical for an adiabatic PBL (Paltredge and Platt 1976), these results suggest that *both* the current and previous modeling studies underpredict mixed layer θ_v. A possible explanation for such

underprediction is improper partition of surface heat fluxes due to overprediction of H_L, as discussed above.

The cause for the predicted superadiabatic θ_v profiles is deduced from vertical profiles of simulated kinematic heat flux (Fig. 20). Profiles are nearly identical to those of AN (Fig. 4), with linearly decreasing positive values throughout the CBL. A linear heat flux profile arises from of the efficiency of turbulent mixing within the CBL, in which surface heating is spread uniformly with height causing height-invariant heating rates. This CBL feature is correctly captured by both the AN HOTC model and the current LOTC model. Yet, since the AN model includes buoyant and transportive contributions to heat flux generation, modeled positive heat fluxes can exist in locally adiabatic or sub-adiabatic conditions (i.e. zero-gradient or countergradient heat fluxes are possible). The current model, however, only includes mechanical (down-gradient) contributions to heat flux generation, and thus generation positive heat fluxes must coincide with $\partial\theta_v/\partial z < 0$ (i.e. a superadiabatic profile).

As discussed in Section 1, accurate prediction of h_i and r_i are essential for accurate CBL simulation. Time variation of h_i is in good agreement with observations (Fig. 17a,b), and when omitting RFD and w_s is only slightly less than AN predictions (Figs. 3b versus 19). Ratio r_i (Fig. 20) is between 12-15% throughout the period, in similar excellent agreement with previous observational, laboratory, and modeling studies (see references in Section 1). The primary source of TKE for entrainment, necessary to deepen the mixed layer, is turbulent transport (Lenschow 1974; Willis and

Deardorff 1974). This term [fourth term on right-hand side of (37)], however, is parameterized in the currently employed K-e closure using K-closure, known to underpredict transport within the CBL (Zeman and Lumley 1976). YM and YA employed K-closure on turbulent transport terms and produced values of $r_t < 2\%$. Accurate prediction of r_t and h_t in the current study is thus attributed to the model l formulation, given by (42)-(44) for daytime convective conditions. This formulation, based on theoretical and observational knowledge of the CBL (see TL), evidently captures CBL processes not explicitly treated in other portions of the turbulence parameterization.

Vertical profiles of observed and simulated q (Fig. 21a,b) show agreement between the magnitude of drying/moistening below/above 700 m. This implies that mixing of air between the CBL and elevated stable layer is properly simulated, further demonstrated by agreement of vertical kinematic humidity fluxes (Fig. 22) with those of AN (Fig. 6). Simulated mixed layer q, however, is overpredicted by ~ 1 gm kg^{-1}, attributed to the model inability to reproduce rapid drying that occurred within the lowest 700 m between 0600-0900 LST (a period not simulated in the AN simulation). This drying must be due to horizontal advection, as surface and upper level sources of dry air were not present during this period for vertical mixing to produce this feature.

Profiles of observed and computed wind speed V (Fig. 23a,b) and wind direction (Fig. 24a,b) show qualitative agreements: daytime V is small and well-mixed below h_t (~ 1000-1200 m), with faster winds developing by 1800 LST due to the onset of the

nighttime inertial oscillation. The qualitative mixed layer directional tendency is captured, although with a stronger amplitude in the simulation. This latter disagreement, as well as those associated with the speed and direction above h_i (Fig. 23a,b), are most likely due to thermal wind inaccuracies, and possibly to horizontal advective effects. Because of the importance of large-scale external forcing on the wind field, and the likely inaccuracy in its specification (via the thermal wind), quantitative agreement between observed and simulated wind velocities (especially during the weak wind conditions within the CBL and above h_i) should not be expected.

Vertical profiles of zonal and meridional components of vertical momentum flux (Fig. 25a,b) show shapes similar to those of AN (Fig. 8a,b), consistent with theoretical expectations for a well-mixed steady state PBL as discussed in Section 1. Differences in surface momentum flux values are ascribed to different values of z_0 used in the current simulation (1 cm) and by AN (1.2 mm, valid only for the central Wangara site). The larger z_0 gives rise to slightly more cross-isobaric flow (higher v) and in turn slightly larger negative slopes in zonal momentum flux profiles in the current simulation.

Simulated daytime TKE (Fig. 26) grows rapidly during the morning hours to a quasi-stationary early afternoon state, and then decays in the late afternoon. Maximum values throughout the period located at ~ $0.25h_i$. This temporal and spatial structure is explained by the relative magnitudes of buoyant production (P_B) and molecular dissipation (P_ϵ) of TKE [second and third terms on the right-hand side of (37)]. During the morning $P_B > P_\epsilon$, consistent with large, increasing values of PBL heat flux (Fig. 20)

and hence P_B, and small values of TKE and hence P_ϵ, leading to $\partial e/\partial z > 0$. During the early afternoon, TKE has grown to the point where $P_B \sim P_\epsilon$, and hence $\partial e/\partial z \sim 0$. During late afternoon $P_B < P_\epsilon$, due to the decrease PBL heat flux, leading to $\partial e/\partial z < 0$. Although maximum values of P_B occur at the surface (where heat flux is maximum), maximum TKE occurs above this height (at $\sim 0.25 h_i$) due to larger l_ϵ and thus smaller values of P_ϵ in this region.

Turbulence data were not measured during the Wangara experiment, and thus it is not possible to directly compare modeled TKE values against observations. However, observational data measured during other CBL field campaigns (e.g., Lenschow 1974; Kaimal et al. 1976; Caughey and Palmer 1979; Lenschow et al. 1980) support the following similarity relationships (based on mixed layer scaling) to describe velocity variances:

$$\frac{\sigma_w}{w_\star} = 1.08 (z/h_i)^{1/3} (1 - z/h_i)^{1/3} \tag{52a}$$

$$\frac{\sigma_u}{w_\star} = \frac{\sigma_v}{w_\star} = 0.40 - 0.15 (z/h_i) \ , \tag{52b}$$

where free convective scale velocity $w_\star$ is given by

$$w_\star = \left(\frac{g H_s h_i}{\theta_a \rho c_p} \right)^{1/3} .$$

Non-dimensional TKE is obtained from (52a,b) by summation of the squares of the individual components and dividing by two.

Simulated non-dimensional TKE at 1200 LST and that obtained from (52a,b) are shown in Fig. 27. The surface TKE value is much lower than that predicted by mixed layer similarity. This is attributed to the formulation of SBL TKE given by (34), which neglects w_* scaling of horizontal variances for unstable SBL conditions. Within the CBL, the simulated TKE is too high below $z/h_i = 0.4$ and too low above this height. This inaccuracy is due to K-closure on turbulent transport employed by the model, which as stated above underestimates transport within the CBL. This formulation represents TKE flux as proportional to $\partial e/\partial z$, although it is known that this flux is directed upwards *throughout* the CBL irrespective of the local sign of $\partial e/\partial z$ (Lenschow 1974; Willis and Deardorff 1974).

The effects of improper TKE flux representation are further seen in the non-dimensional TKE budget for 1200 LST (Fig. 28). Here, the transport term is negative when integrated over h_i, physically impossible as turbulent transport cannot create or destroy TKE but only transport it. The negative integrated value is amplified by the improper lower boundary condition on TKE, as underpredicted TKE values within the SBL lead to an overly large transportive loss within the lower CBL as TKE is overly diffused downward into the SBL.

The AN model does not have the above described deficiencies regarding predicted TKE. Its predicted profiles are in agreement with mixed layer scaling, and

predicted turbulent transfer is ~ 0 when integrated over h_t (Fig. 29a,b). This results from its prognostic determination of TKE flux, which includes non-mechanical processes that enable upward directed, countergradient TKE flux.

The inaccuracies that exist in the daytime TKE structure have only small effects on the predictions of mean variables and their turbulent fluxes within the mixed layer. Except for erroneously predicted slight superadiabatic daytime θ_v profiles, predictions of these variables have been shown above to be consistent with observations and with AN results. Evidently, the large values of TKE experienced during the day are sufficient to produce an accurate mean well-mixed CBL structure regardless of the details concerning the corresponding TKE vertical structure. In fact, knowledge of TKE is unnecessary to successfully represent mean quantities within the one-dimensional CBL; an accurate description of mean quantities can usually be obtained from properly chosen LOTC parameterizations (Pielke 1984). However, a fundamental reason for the inclusion of a prognostic equation for TKE is its application to the two and three dimensional PBL, where horizontal TKE advection can significantly alter vertical mixing in regions where the local vertical θ_v and V profiles would otherwise produce different characteristics. To this end, it is important to properly quantify the magnitude and vertical structure of TKE in regions where, and periods when, its significant production takes place (e.g., within the daytime CBL). Based on the current W33 model results, improvements to *K-e* closure are needed to achieve this.

b) Nighttime PBL structure

Strong cooling and stabilization near the surface at the evening transition eliminates positively buoyant turbulent motions associated with the daytime PBL. Coupling between the upper and lower regions of the PBL thus ceases, and TKE within the mixed layer rapidly dissipates. The nighttime PBL is thus only weakly turbulent, and as such can be highly influenced by RFD, advection, baroclinicity, and/or gravity waves.

Nighttime profiles of simulated θ_v and V (Fig. 30a,b) show the division of the nighttime PBL into two regions. Below ~ 200 m is the nocturnal boundary layer (NBL), characterized by strong thermal stability and wind shear. Above the NBL and capped by the elevated stable layer is the deep, quasi-adiabatic residual layer (RL), remnant of the daytime mixed layer. V increases throughout the evening in both layers due to the large day-to-night decrease in frictional stress (as turbulence becomes weak) and resulting imbalance between pressure gradient and Coriolis forces. This acceleration is greatest at the NBL top, giving rise to a low-level jet (LLJ) at this level.

The vertical structure and tendency of TKE throughout the nighttime PBL are largely determined by the θ_v and V fields through their effects on buoyant destruction and shear production of TKE. The ratio of these terms is proportional to the gradient Richardson number

$$Ri = \frac{g}{\theta_a} \frac{\Delta\theta}{(\Delta V)^2} \Delta z \ . \tag{53}$$

Turbulent production ceases when Ri exceeds a critical value Ri_c, which from theoretical considerations and observations (Miles et al. 1961; Shir and Bornstein 1977; Gedzelman and Rilling 1978) ranges between 0.25-0.50 in the PBL. Vertical profiles of simulated Ri (Fig. 31) for early and late evening hours show regions of sub-critical Ri (< 0.50) within the lower half of the NBL and within a portion of the RL. Between these regions (~ 200-400 m) Ri is super-critical, consistent with the proximity of the LLJ, which represents a region of zero wind shear and hence high Ri. The NBL and RL are thus turbulently decoupled, as shown in TKE fields in Fig. 32, and mean and turbulent NBL ab=nnd RL structures are thus discussed separately below.

The importance of horizontal advection throughout nighttime W33 is illustrated in profiles of observed specific humidity (Fig. 33a). Observations are characterized by $\partial q / \partial t > 0$ throughout the PBL, with the development of a pronounced moisture maximum at ~ 150 m. As with the early morning (0600-0900 LST) drying that influenced the observed daytime q field, such a feature must be caused by horizontal advection, as clouds (that could evaporate) and surface and upper level sources of moist air (for vertical mixing) were not present during the period. Obviously, it is impossible for 1-D model simulated profiles to match observations in this case. Instead, simulated profiles (Fig. 33b) show drying within the NBL due to surface dew formation and the resulting flux of q from the NBL to the surface, a maintenance of daytime values within the RL, and drying within the elevated stable layer due to subsidence. The inability of the model to simulate this horizontal moisture advection leads to nighttime underpredictions of $q_{1.2}$

and $T_{l,2}$ (Fig. 13a,b), the latter due to underprediction of radiatively attenuating gas and hence R_D.

1) Nocturnal Boundary Layer

In the ensuing discussion, the NBL is defined to extend to the level above the surface at which $\partial\theta'/\partial z$ first becomes less than 3.5 K km^{-1}, denoted as h_s. This definition, also used by Garratt and Brost (1981), allows the region of strong radiative cooling above the turbulent region of the NBL (shown below) to be included within its definition.

Nighttime profiles of observed and simulated θ_v within the NBL (Fig. 34a,b) show similar cooling rates and NBL growth. Cooling within the NBL results from both turbulent and radiative flux divergences (Fig. 35a,b), dominated by the former between approximately 0.1-0.8h_s, and the latter between 0.8-1.0h_s and upward into the RL. Such a structure is consistent with the "three-layer" model proposed by Garratt and Brost (1981) based on their fine-scale (~ 1 m resolution near surface) NBL model results, except that their layer dominated by RFD between 0.0-0.1h_s is not captured here due to the course model resolution within this region. Because of the importance of RFD in the upper part of the NBL, h_s is often deeper than the *turbulent* NBL depth h_t (Mahrt et al. 1979), defined as the level where TKE becomes negligibly small (e.g., 1% of the surface value). Predicted time variations of h_s and h_t for the nighttime period (Fig. 36) show this feature.

Comparison of observed and simulated V within the NBL (Fig. 37a,b) show good agreement in LLJ magnitude through 0000 LST Day 34 (with slight underprediction after

this time) and underestimations of LLJ height by 25-50 m throughout the period. Momentum tendency within the nighttime PBL is largely determined by the external pressure gradient force. Since great uncertainty exists in the specification of this force (through the geostrophic wind specification discussed in Section 3), it is unwarranted to attribute inaccuracies in simulated V to flaws in the model formulation without further tests performed in other cases.

Due to small nighttime values of TKE, high quality measurements of this parameter are difficult to obtain. Data used to derive similarity relationships for NBL TKE thus contain more scatter than those for the CBL given by (52a,b). Measured data do however lend credence to the "local" or "z-less" scaling proposed by Nieuwstadt (1984), and further developed by other investigators (e.g., Sorbjan 1986; Lenschow et al. 1988). Here, explicit scaling with z (as in MO similarity) ceases, and turbulent quantities scale with local stress and length scales. The general form of non-dimensional equations for momentum variances, matched with those for MO similarity at h, are as follows:

$$\frac{\sigma_i^2}{u_\star^2} = B_i \left(1 - \frac{z-h}{h_t} \right)^{\alpha'} , \qquad (54)$$

where i is any of the three momentum components, and B_i and α' are numerical constants.

Simulated non-dimensional TKE within the NBL at 0000 LST Day 34 is shown in Fig. 38 with predictions by (54) for values of α' representative of the range of measured values, and B_i appropriately set such that (54) and (34) match at h. Simulated TKE above

$\sim 0.4h_t$ is higher than local similarity predictions. Although the observed NBL TKE structure often does not obey local similarity due, for example, to advective effects and intermittency, no such reason for the discrepancy with local similarity predictions exists in the current model formulation. This discrepancy must thus be due to a flaw in the model formulation.

Explanation for the inaccurate TKE predictions within the NBL is obtained from inspection of the simulated nighttime TKE production budget for 0000 LST Day 34 in Fig. 39. TKE is almost completely stationary, leading to the following diagnostic equation for TKE within the NBL

$$e = \frac{C_A l_\epsilon l_m}{C_\epsilon} \left(\frac{\Delta V}{\Delta z} \right)^2 [1\text{-}Ri] \quad . \tag{55}$$

This equation was derived by assuming a balance between molecular dissipation, buoyant destruction, and shear production of TKE, making use of (36) for K_m and K_h. Proper proportionality of TKE to local conditions (i.e., $\Delta V/\Delta z$, Ri) thus necessitates l_m and l_ϵ formulations appropriate for the NBL. The stable-condition correction terms C_{sk}/l_s and $C_{s\epsilon}/l_s$ in (45)-(47), however, were derived primarily for use within the CBL-capping elevated stable layer to describe the penetration-depth of *vertical* turbulent motions from the CBL into the elevated stable layer (Sun and Ogura 1980). This correction term is thus inappropriate for use within the NBL, in which turbulent motion is primarily *horizontal* due to shear production and strong thermal stability (which inhibits vertical

turbulent motions). Because of the implied assumption that vertical TKE is dominant, it is believed that (45)-(47) overpredict NBL length scales, and hence TKE.

2) Residual Layer

Vertical profiles of observed and simulated RL θ_v (Fig. 40a,b) both show maintenance of daytime near-neutrality. Simulated radiative cooling is, however, not observed, believed due to warm horizontal advection. The presence of warm advection is supported by the structure of the observed thermal winds (Fig. 2a,b). These are comprised of increasing u_g with height, corresponding to $\partial T/\partial y > 0$ in the Southern Hemisphere (warmer air to North). Since RL V has a strong northerly component throughout much of the evening, warm air advection would result (Hess 1978). A simulation including thermal wind-based temperature advection (not shown) produced a better match between observed and simulated RL θ_v.

Better agreement is found between observed and simulated RL V (Figs. 41a,b and 42a,b). Inertial accelerations are generally well-captured, although the amplitude of the directional oscillation is slightly overpredicted. Again, uncertainties in input thermal wind values preclude attribution of this error to deficiencies in the model formulation.

Quasi-neutral stability and non-zero wind shear within the RL result in sub-critical Ri values within a large portion of the RL (Fig. 31), allowing for maintenance of a portion of daytime TKE and/or regeneration of TKE later in the evening. TKE production budgets for representative early and late evening hours (Fig. 43a,b) show that the

the RL is characterized by persistent shear production of TKE and a sign change in buoyancy production from positive during early evening hours to negative in later hours. This transition is correlated with an identical sign change in the time tendency term, leading to decreased amounts of TKE throughout the RL in the late evening.

The transition from buoyancy production to destruction implies stabilization within the RL throughout the night. Profiles of warming rate (i.e., sum of turbulent, radiative, and subsidence warming) within the RL (Fig. 44) show that RL cooling decreases slightly and approximately linearly with height at a rate of $\sim 2.2 \times 10^{-5}$ K hr^{-1}/m (deduced from line superimposed onto Fig. 44). Because $\partial/\partial z(\partial\theta_v/\partial t) = \partial/\partial t(\partial\theta_v/\partial z)$, this value can be interpreted as the RL stabilization rate. This stabilization is attributed to the height variation in RFD, determined through (1)-(5) by the magnitude and height variations of thermodynamic variables θ_v and q.

From the above results, RL TKE structure seems highly influenced by slight variations in stability centered around neutrality, in turn determined by variations in the vertical structure of mean thermodynamic variables. To partially test the sensitivity of TKE generation to such variations, a simulation was performed with the initial value of $\partial q/\partial z$ above 1400 m decreased by 10% (i.e., a larger negative value), resulting in a dryer elevated stable layer. The original and new cases will be referred to as A and B, respectively.

Warming rates within the RL for Case B (Fig. 45) show destabilization in the upper RL during early evening, followed by a slightly smaller stabilization rate

throughout the night (Fig. 44) compared to the Case A (Fig. 43). The decreased stabilization rate in turn leads to a maintenance of buoyant TKE production throughout the night (Fig. 46a,b), higher values of RL TKE (Fig. 47a, Fig. 32), and a persistence of negative *Ri* values throughout the night in Case B (Fig. 47b).

Decreased stabilzation and larger TKE values in Case B result from the impact of upper level moisture on the vertical structure of downward emitted longwave radiation. The decreased q within the elevated stable layer leads to decreased downward radiative flux from the elevated stable layer into the RL. Subsequently, increased radiative cooling in the upper RL occurs, as there is less downward flux into the upper RL to counterbalance that emitted downward from there into the lower region of the RL. Because cooling is increased in the upper RL, stability within the entire RL is weaker, and hence TKE is more easily maintained/regenerated. In addition to illustrating the impact that variations in RL stabilization have on TKE generation within this region, the Case B results also show that such variations need not be caused by changes to the *local* mean thermodynamic structure within the RL. Such variations can result from changes in mean thermodynamic profiles *outside* the RL, e.g., in the elevated stable layer.

Although relative case-to-case variations in RL TKE values can be high depending on the stabilization rate within the RL, the amount of TKE within the RL is only ~ 1% of that within the CBL (Figs. 26 and 32). To address whether such case-to-case variations in the amount of RL TKE are significant, horizontal wind speed differences between Case B and A (V_B - V_A) were computed (Fig. 48). Impacts on V due to the larger TKE values in Case B are most pronounced during late evening and early

34, where slower V results in the lower RL, and faster V results in the upper RL. This pattern is a consequence of increased mixing of momentum upwards from the lower to upper RL in Case B. The change in V relative to Case A speeds ranges from 3-10%, with the maximum change at the interface between the RL and elevated stable layer. Alteration of V at this location could have significant impact of mixing between the PBL and elevated stable layer, as corresponding changes in Ri could allow Ri to become greater or less than Ri_c, depending on the orientation of wind shear across the interface.

The importance of case-to-case RL TKE variations can also be assessed through the effects on the vertical diffusion of pollutants (e.g., from a point source with an effective stack height within the RL). Vertical diffusion is often characterized by diffusion coefficient σ_z, related to eddy diffusivity by

$$\sigma_z = \sqrt{2K_m \frac{d}{V}}, \tag{56}$$

where d represents downwind travel distance. Values of σ_z at selected values of d for minimum (0.4 m^2s^{-1}) and maximum (3.5 m^2s^{-1}) peak values of K_m (from Fig. 49a,b) and $V = 8$ ms^{-1} (a value close to that simulated within the RL for the W33 case) are plotted in Fig. 50, along with curves for various Pasquill-Gifford stability classes. The range of σ_z for Cases A and B spans the F-D stability classifications, implying significant effects of RL TKE variations on pollutant mixing within the RL.

5. CONCLUSION

Resimulation of Wangara Day 33 (W33) was performed to address unresolved issues concerning the accuracy with which its daytime and nighttime periods can be modeled using a one-dimensional PBL model. In particular, the degree to which accuracy is lost by use of lower order turbulence closure (LOTC) to simulate daytime W33 was carefully assessed, and nighttime W33 results were analyzed in detail reflective of recent understanding of nocturnal PBL structure. Model improvements incorporated for the study include implementation of updated longwave radiation emissivity functions, an advanced predictive scheme for surface temperature and specific humidity, an improved SBL formulation, and modifications of the Therry and Lacarrère (1983) turbulent length scales for use in nighttime conditions.

Simulation of daytime W33 yielded predictions of daytime mean variables and turbulent fluxes consistent with observations and predictions of higher order turbulence closure (HOTC) models. CBL growth was well-simulated, with values of the ratio of the negative heat flux at the CBL top to the surface heat flux (denoted by r_i) ranging from 12-15% throughout the daytime period. Simulated turbulent kinetic energy (TKE) was, however, in disagreement with mixed layer similarity predictions, with TKE overly concentrated within the lower CBL and erroneous non-zero values of vertically integrated turbulent transport obtained.

Accurate predictions of daytime mean variables and turbulent fluxes result because of large TKE values within the CBL, which enable mean variables to become vertically well-mixed and their turbulent fluxes to be correctly distributed with height regardless of TKE vertical structure. As a result, proper simulation of CBL mean variables only requires proper prediction of surface forcing and of the CBL depth h_i. Prediction of h_i should in theory be adversely affected by limitations of K-based LOTC. However, through proper specification of turbulent length scales (as in the current study) accurate simulation of h_i, and consequently mean variables, can be achieved with LOTC models.

TKE structure within the CBL is more complicated than that for mean variables and turbulent fluxes due to molecular dissipation, which only affects auto-correlated components of turbulent fluctuations. Because dissipation occurs in small eddies, its effects are most dominant near the ground (where eddy size is small), resulting in maximum TKE values located within the CBL, rather than at the surface. K-based LOTC models will not properly locate this maximum due to K-closure on the TKE transport term, which underestimates upward transport due to improper representation of TKE flux as down the local TKE gradient. As a result, TKE is overly concentrated in the lower half of the CBL.

Improper simulation of the vertical structure of TKE within the CBL could have impacts on the prediction of other PBL and mesoscale processes. Improper vertical distribution of TKE would lead to inaccurate vertical variations in horizontal TKE

advection. Also since TKE is overly concentrated in the lower CBL, its amount in the nighttime RL at the evening transition could be underestimated, which may have implications regarding turbulent mixing in this region. A quantitative assessment these potential implications is reserved for future work.

Corrections for the inaccuracy of daytime TKE predictions by K-based LOTC models include employment of a countergradient correction term in the TKE flux formulation (Therry and Lacarrère 1983) and use of arbitrarily defined larger values of K_e to increase upward transport (Sun and Chang 1986; Andrén 1990). The validity of the countergradient correction term in regions outside the middle CBL is, however, questionable due to non-stationarity within these regions, while the use of larger K_e values (although effective in locating maximum TKE in the middle CBL) still describes TKE flux as a down-gradient process. Development of a more theoretically sound means for improving the LOTC description of TKE flux is thus required.

Simulation of the nighttime period captured the main observed qualitative features, with decoupling of the nighttime PBL into a highly thermally stable, surface-based nocturnal boundary layer (NBL) and deep, adiabatic residual layer (RL) aloft. The combined effect of θ_v and V vertical profiles (through Ri) led to decoupling of NBL and RL TKE. Horizontal advection, reflected in the observed nighttime θ_v and q fields, could not be captured using the current one-dimensional model formulation. Inability to account for this advection led to underpredicted values for both nighttime 1.2 meter temperature and specific humidity.

While profiles of mean variables within the NBL were well simulated, overprediction of TKE, as compared to predictions by local similarity relationships, resulted in the upper NBL. This overprediction is believed to result from improper representation of turbulent length scales within the NBL. The stable-condition correction term for these length scales was designed for use within the capping stable layer of the CBL, where TKE has a strong vertical component due to penetration of CBL eddies. These expressions are believed invalid within the NBL, where TKE is primarily *horizontal* due to shear production.

It is hypothesized that use of expressions for turbulent length scales valid within the NBL will produce more realistic TKE values. Recently, Degrazia et al. (1996) proposed length scales based on Taylor diffusion theory, which for stable conditions converge to the local Obukhov length scale with increasing z. It is planned to implement these length scales to test this hypothesis.

RL turbulent structure was found highly sensitive to its rate of stabilization. The transition from thermal instability to stability during the early evening, and corresponding transition from buoyant TKE production to destruction, led to a pronounced decrease in TKE over the period. Stabilization was due to height-decreasing radiative cooling rates within the RL.

A simulation with decreased initial values of specific humidity within the capping stable layer resulted in increased radiative cooling in the upper region of the RL. This led to smaller RL stabilization rates (as cooling was increased aloft within the RL), and to

a persistence of RL TKE throughout the evening. The associated increase in turbulent mixing led to increased wind speed at the RL/elevated stable layer interface, lowering *Ri* at the interface. An increase in the magnitude of pollutant mixing within the RL was also deduced from calculations of σ_z from values of K_m representative of cases with and without decreased specific humidity within the elevated stable layer.

Results from the above simulations suggest the need for model improvements in addition to those already mentioned. Underprediction of SBL TKE during the day necessitates mixed layer scaling of SBL velocity variances. This scaling arises from near-surface convergent velocities that result from circulation of buoyantly driven, semi-organized rising plumes within the CBL. Sykes et al. (1989) and Zilitinkevich (1995) have recently proposed a "minimum u_*" representative of local stresses resulting from these convectively induced horizontal velocities. However, incorporation of mixed layer scaling for SBL velocity variances should also be carried out in combination with parameterization of the semi-organized buoyant motions which give rise to the scaling, best achieved through use of non-local closure models discussed in Section 1. Development of a parameterization for semi-organized CBL motions that links appropriate effects within the SBL and CBL is planned.

Underprediction of CBL virtual potential temperature by the current and previous W33 studies suggests inappropriateness of experimentally determined, single-site surface energy fluxes to force modeled W33 PBL tendencies. Local scale surface heterogeneity, known to have a significant, non-linear effect on grid-area averaged surface fluxes

(Doran et al. 1995; Beljaars and Holtslag 1991), may have been important during W33. This importance is emphasized by the observed nighttime low-level maximum in q, undoubtedly attributed to horizontal advection, possibly locally-driven. Existing parameterizations for the effects of subgrid scale heterogeneity (e.g., Wetzel and Chang 1988; Avissar and Pielke 1989; Beljaars and Holtslag 1991; Uliasz and Pielke 1992; Blyth and Dolman 1995) will guide future development of a scheme to treat these effects.

REFERENCES

Al Nakshabandi, G., and Kohnke, H., 1965: Thermal conductivity and diffusivity of soils as related to moisture tension and other physical properties. *Agric. Meteor.*, **2**, 271-279.

André, J. C., G. De Moor, P. Lacarrère, G. Therry, and R. Du Vachat, 1978: Modeling the 24-hour evolution of the mean and turbulent structures of the planetary boundary layer. *J. Atmos. Sci.*, **35**, 1861-1883.

Andrén, A., 1991: Evaluation of a turbulence closure scheme suitable for air-pollution applications. *J. Appl. Meteor.*, **29**, 224-239.

Arya, S. P. S., and J. C. Wyngaard, 1975: Effect of baroclinity on wind profiles and the geostrophic drag law for the convective boundary layer. *J. Atmos. Sci.*, **32**, 767-778.

Avissar, R., and R. A. Pielke, 1989: A parameterization of heterogeneous land surfaces for atmospheric numerical models and its impact on regional meteorology. *Mon. Wea. Rev.*, **117**, 2113-2136.

Beljaars, A. C. M., and A. A. M. Holtslag, 1991: Flux parameterization over land surfaces for atmospheric models. *J. Appl. Meteor.*, **30**, 327-341.

Blackadar, A. K., 1962: The vertical distribution of wind and turbulent exchange in a neutral atmosphere. *J. Geophys. Res.*, **67**, 3095-3102.

———, 1979: High resolution models of the planetary boundary layer. *Advances in Environmental and Scientific Engineering*, Vol. 1, Gordon and Breach, 276 pp.

Blyth, E. M., and A. J. Dolman, 1995: The roughness length for heat of sparse vegetation. *J. Appl. Meteor.*, **34**, 583-585.

Bornstein, R. D., P. Thunis, P. Grossi, and G. Schayes, 1996: Topographic Vorticity-mode Mesoscale-β (TVM) model: Part II- Evaluation. *J. Appl. Meteor.*, **35**, 1835-1845.

Brutsaert, W. A., 1982: *Evaporation into the Atmosphere*. Reidel, Dordrecht, 299 pp.

Busch, N. E., S. W. Chang, and R. A. Anthes, 1976: A multilevel model of the planetary boundary layer suitable for use with mesoscale dynamical models. *J. Appl. Meteor.*, **15**, 909-919.

Businger, J. A., 1973: A note on free convection. *Bound. Layer Meteor.*, **4**, 323-326.

———, J. C. Wyngaard, Y. Izumi, and E. F. Bradley, 1971: Flux profile relationships in the atmospheric surface layer. *J. Atmos. Sci.*, **28**, 181-189.

Camillo, P. J., R. J. Gurney, and T. J. Schmugge, 1983: A soil and atmospheric boundary layer model for evapotranspiration and soil moisture studies. *Water Resour. Res.*, **19**, 371-380.

Carson, D. J., and P. J. R. Richards, 1978: Modeling surface turbulent fluxes in stable conditions. *Bound. Layer Meteor.*, **14**, 67-81.

Caughey, S. J., and S. G. Palmer, 1979: Some aspects of turbulence structure through the depth of the convective boundary layer. *Quart. J. Roy. Meteor. Soc.*, **105**, 811-827.

Chen, C., and W. R. Cotton, 1983: Numerical experiments with a one-dimensional higher order turbulence model: simulation of the Wangara Day 33 case. *Bound. Layer Meteor.*, **25**, 375-404.

Clapp, R., and G. Hornberger, 1978: Empirical equations for some soil hydraulic properties. *Water. Resour. Res.*, **14**, 601-604.

Clarke, R. H., and G. D. Hess, 1974: Geostrophic departure and the functions A and B of Rossby-number similarity theory. *Bound. Layer Meteor.*, **7**, 267-287.

———, A. J. Dyer, R. R. Brook, D. G. Reid, and A. J. Troup, 1971: *The Wangara Experiment: Boundary Layer Data.* Commonwealth Science and Industrial Research Organisation, 362 pp.

Deardorff, J. W., 1970: Convective velocity and temperature scales for the unstable boundary layer and for Rayleigh convection. *J. Atmos. Sci.*, **27**, 1211-1213.

———, 1974a: Three-Dimensional numerical study of the height and mean structure of a heated planetary boundary layer. *Bound. Layer Meteor.*, **7**, 81-106.

———, 1974b: Three-Dimensional numerical study of turbulence in an entraining mixed layer. *Bound. Layer Meteor.*, **7**, 199-216.

———, 1978: Efficient prediction of ground surface temperature and moisture, with Inclusion of a layer of vegetation. *J. Geophys. Res.*, **83**, 1889-1903.

Degrazia, G. A., O. L. L. Moraes, and A. P. Oliveira, 1996: An analytical method to evaluate mixing length scales for the planetary boundary layer. *J. Appl. Meteor.*, **35**, 974-977.

Detering, H. W., and D. Etling, 1985: Application of the E-ϵ turbulence model to the atmospheric boundary layer. *Bound. Layer Meteor.*, **33**, 113-133.

Doran, J. C., W. J. Shaw, and J. M. Hubbe, 1995: Boundary layer characteristics over areas of inhomogeneous surface fluxes. *J. Appl. Meteor.*, **34**, 559-571.

Estoqué, M. A., 1968: Vertical mixing due to penetrative convection. *J. Atmos. Sci.*, **25**, 561-575.

Garratt, J. R., 1992: *The Atmospheric Boundary Layer*. University Press, Cambridge.

———, and R. A. Brost, 1981: Radiative cooling effects within and above the nocturnal boundary layer. *J. Atmos. Sci.*, **38**, 2730-2744.

———, and R. J. Francey, 1978: Bulk characteristics of heat transfer in the unstable, baroclinic atmospheric boundary layer. *Bound. Layer Meteor.*, **15**, 399-421.

———, B. B. Hicks, and R. A. Valigura, 1993: Comments on "The roughness length for heat and other vegetation parameters for a surface of short grass". *J. Appl. Meteor.*, **32**, 1301-1303.

Gedzelman, S. D., and R. Rilling, 1978: Short-period atmospheric gravity waves: A study of their dynamical and synoptic features. *Mon. Wea. Rev.*, **107**, 667-681.

Grossi, P., 1993: Modili di circolazione a mesoscala: analisi e confronto qualitativo e quantativo con le osservazioni. Tesi di Laurea, Facolta di Fisica, Univ. di Milano.

Guillement, B., H. Isaka, and P. Mascart, 1983: Molecular dissipation of turbulent fluctuations in the convective mixed layer. *Bound. Layer Meteor.*, **27**. 141-162.

Hess, G. D., B. B. Hicks, and T. Yamada, 1981: The impact of the Wangara experiment. *Bound Layer Meteor.*, **20**, 135-174.

Hess, S. L., 1978: *Introduction to Theoretical Meteorology*. Krieger Publishing Company, 362 pp.

Hicks, B. B., 1976: Wind profile relationships from the Wangara experiment. *Quart. J. R. Met. Soc.*, **102**, 535-551.

———, 1981: An analysis of Wangara micrometeorology: Surface stress, sensible heat, evaporation, and dewfall. NOAA Tech. Memo. ERL-104, 36 pp.

Högström, U., 1988: Non-dimensional wind and temperature profiles in the atmospheric surface layer: A re-evaluation. *Bound. Layer Meteor.*, **42**, 55-78.

Holtslag, A. A. M., and H. A. R. De Bruin, 1988: Applied modeling of the nighttime surface energy balance over land. *J. Appl. Meteor.*, **27**, 689-704.

Huang, X., and T. J. Lyons, 1995: The simulation of surface heat fluxes in a land surface-atmosphere model. *J. Appl. Meteor.*, **34**, 1099-1111.

Kader, B. A., and A. M. Yaglom, 1990: Mean fields and fluctuation moments in unstably stratified turbulent boundary layers. *J. Fluid Mech.*, **212**, 637-662.

Kaimal, J. C., J. C. Wyngaard, D. A. Haugen, O. R. Coté, Y. Izumi, S. J. Caughey, and C. J. Readings, 1976: Turbulence structure in the convective boundary layer. *J. Atmos. Sci.*, **33**, 2152-2169.

Kitchen, M., J. R. Leighton, and S. J. Caughey, 1983: Three case studies of shallow convection using a tethered balloon. *Bound. Layer Meteor.*, **27**, 281-308.

Kondo, J., O. Kanechika, and N. Yasuda, 1978: Heat and momentum transfer under strong stability in the atmospheric surface layer. *J. Atmos. Sci.*, **35**, 1012-1021.

———, N. Saigusa, and T. Sato, 1990: A parameterization of evaporation from a bare soil surface. *J. Appl. Meteor.*, **29**, 385-389.

Kondratyev, K. Y., 1969: *Radiation in the Atmosphere*. Academic Press, 912 pp.

Lee, T. J., and R. A. Pielke, 1992: Estimating the soil surface specific humidity. *J. Appl. Meteor.*, **31**, 480-484.

Lenschow, D. W., 1974: Model of the height variation of the turbulent kinetic energy budget in the unstable planetary boundary layer. *J. Atmos. Sci.*, **31**, 465-474.

———, J. C. Wyngaard, and W. T. Pennell, 1980: Mean-field and second-moment budgets in a baroclinic, convective boundary layer. *J. Atmos. Sci.*, **37**, 1313-1326.

———, X. S. Li, C. J. Zhu, and B. Boba Stankov, 1988: The stably stratified boundary layer over the Great Plains. *Bound. Layer Meteor.*, **42**, 95-121.

Mahouf, J. F., and J. Noilhan, 1991: Comparitive study of various formulations of evaporation from bare soil using in situ data. *J. Appl. Meteor.*, **30**, 1354-1365.

Mahrt, L., R. C. Heald, D. H. Lenschow, B. B. Stankov, and I. Troen, 1979: An observational study of the structure of the nocturnal boundary layer. *Bound. Layer Meteor.*, **17**, 247-264.

Mailhot, J., and R. Benoit, 1982: A finite-element model of the atmospheric boundary layer suitable for use with numerical weather prediction models. *J. Atmos. Sci.*, **39**, 2249-2266.

Malcher, J., and H. Kraus, 1983: Low-level jet phenomena described by an integrated dynamical PBL model. *Bound. Layer Meteor.*, **27**, 327-343.

McCumber, M. C., and R. A. Pielke, 1981: Simulation of the effects of surface fluxes of heat and moisture in a mesoscale numerical model, 1. Soil layer. *J. Geophys. Res.*, **86**, 9929-9938.

McNider, R. T., and R. A. Pielke, 1981: Diurnal boundary-layer development over sloping terrain. *J. Atmos. Sci.*, **38**, 2198-2212.

McPherson, R. P., 1970: A numerical study of the effect of a coastal irregularity on a sea breeze. *J. Appl. Meteor.*, **9**, 767-777.

Mellor, G. L., and T. Yamada, 1974: A hierarchy of turbulence closure models for planetary boundary layers. *J. Atmos. Sci*, **31**, 1791-1806.

———, and ——— 1982: Development of a turbulence closure model for geophysical fluid problems. *Rev. Geophys. Space Phys.*, **20**, 851-875.

Mihailović, D. T., B. Rajković, B. Lalić, and L. Dekić, 1995: Schemes for parameterizing evaporation from a non-plant covered surface and their impact on partitioning the surface energy in land-air exchange parameterization. *J. Appl. Meteor.*, **34**, 2462-2475.

Miles, J. W., 1961: On the stability of heterogeneous shear flows. *J. Fluid Mech.*, **10**, 496-508.

Monteith, J. L. , 1981: Evaporation and surface temperature. *Quart. J. R. Met. Soc.*, **107**, 1-27.

Nieuwstadt, F. T. M., 1984: The turbulent structure of the stable, nocturnal boundary layer. *J. Atmos. Sci.*, **41**, 2202-2216.

O'Brien, J. J., 1970: A note on the vertical structure of the eddy exchange coefficient in the planetary boundary layer. *J. Atmos. Sci.*, **27**, 1213-1215.

Panayiotou, C., 1995: Application of the prognostic URBMET/TVM meso-β meteorological model to Phoenix, Az. M.S. thesis, San Jose State University.

Pandolfo, J., and M. A. Atwater, 1965: The development of a numerical prediction model for the planetary boundary layer. Final Rept. 7465-174, Contract Cwb-10960, The Travelers Research Center, Inc.

Panofsky, H. A., H. Tennekes, D. H. Lenschow, and J. C. Wyngaard, 1977: The characteristics of turbulent velocity components in the surface layer under convective conditions. *Bound. Layer Meteor.*, **11**, 355-361.

Passerat de Silans, A., L. Bruckler, J. L. Thony, and M. Vauchlin, 1989: Numerical modeling of coupled heat and water flows during drying in a stratified bare soil-comparison with field observations. *J. Hydro.*, **105**, 109-138.

Philip, J. R., 1957: Evaporation, and moisture and heat fields in the soil. *J. Meteor.*, **14**, 354-366.

Pielke, R. A., 1984: *Mesoscale Meteorological Modeling.* Academic Press, 612 pp.

———, and Y. Mahrer, 1975: Representation of the heated planetary boundary layer in mesoscale models with coarse vertical resolution. *J. Atmos. Sci.*, **32**, 2288-2308.

Pleim, J. E., and A. Xiu, 1995: Development and testing of a surface flux and planetary boundary layer model for application in mesoscale models. *J. Appl. Meteor.*, **34**, 16-32.

Ramanathan, N., K. Srinivasan, and B. V. Seshasayee, 1995: Numerical simulation of boundary layer variables using e-ϵ closure scheme. *J. Appl. Meteor.*, **34**, 542-548.

Sasamori, T., 1968: The radiative cooling calculation for application to general circulation experiments. *J. Appl. Meteor.*, **7**, 721-729.

———, 1970: A numerical study of atmospheric and soil boundary layers. *J. Atmos. Sci.*, **27**, 1122-1137.

Schayes, G., P. Thunis, and R. Bornstein, 1996: Topographic Vorticity-mode Mesoscale-β (TVM) model: Part I- Formulation. *J. Appl. Meteor.*, **35**, 1815-1823.

Shir, C. C., and R. D. Bornstein, 1977: Eddy exchange coefficients in numerical models of the planetary boundary layer. *Bound. Layer Meteor.*, **11**, 171-185.

Slade, D. H., 1968: *Meteorology and Atomic Energy*. United States Atomic Energy Commission, 445 pp.

Sorbjan, Z., 1986: An examination of local similarity theory in the stably stratified boundary layer. *Bound. Layer Meteor.*, **38**, 63-71.

Stull, R. B., 1984: Transilient turbulence theory. Part I: The concept of eddy mixing across finite distances. *J. Atmos. Sci.*, **41**, 3351-3367.

———, R. B., 1988: *An Introduction to Boundary Layer Meteorology*. Kluwer Academic, 666 pp.

Sun, W., and Y. Ogura, 1980: Modeling the evolution of the convective planetary boundary layer. *J. Atmos. Sci.*, **37**, 1558-1572.

———, and C. Z. Chang, 1986: Diffusion model for a convective layer. Part I: Numerical simulation of convective boundary layer. *J. Climate Appl. Meteor.*, **25**, 1445-1453.

Sykes, R. I., D. S. Henn, and W. S. Lewellen, 1993: Surface-layer description under free- convection conditions. *Quart. J. R. Met. Soc.*, **119**, 409-421.

Taylor, P. A., and Y. Delage, 1971: A note on finite-difference schemes in the surface and planetary boundary layer. *Bound. Layer Meteor.*, **2**, 108-121.

Therry, G., and P. Lacarrère, 1983: Improving the eddy kinetic energy model for planetary boundary layer description. *Bound. Layer Meteor.*, **25**, 63-88.

Thunis, P., 1995: Formulation and Evaluation of a Nonhydrostatic Vorticity-mode Mesoscale Model, Rept. EUR-16141-EN, European Community Joint Research Center, Ispra, IT., 151 pp.

Trembeck, C. J., and R. Kessler, 1985: A surface temperature and moisture parameterization for use in mesoscale numerical models.

Uliasz, M., 1994: Subgrid-scale parameterization. *Mesoscale Modeling of the Atmosphere*, R. A. Pielke and R. P. Pearce, Eds., Amer. Meteor. Soc., 13-19.

———, and R. A. Pielke, 1992: Effect of land surface representation on simulated mesoscale pollution dispersion. *Air Pollution Modelling and its Application IX*, H. Van Dop and G. Kallos, Eds., Plenum Press, 163-170.

Webb, E. K., 1970: Profile relationships: the log-linear range and extension to strong stability. *Quart. J. Roy. Meteor. Soc.*, **96**, 67-90.

Welch, R., and W. Zdunkowski, 1976: A radiation model of the polluted atmospheric boundary layer. *J. Atmos. Sci.*, **33**, 2170-2184.

Wetzel, P. J., and J. Chang, 1987: Evaporation and moisture and heat fields in the soil. *J. Climate Appl. Meteor.*, **26**, 18-27.

———, and ——— 1988: Evapotranspiration from nonuniform surfaces: A first approach for short-term numerical weather prediction. *Mon. Wea. Rev.*, **116**, 600-621.

Willis, G. E., and J. W. Deardorff, 1974: A laboratory model of the unstable planetary boundary layer. *J. Atmos. Sci.*, **31**, 1297-1307.

Wyngaard, J. C., and O. R. Coté, 1974: The evolution of a convective planetary boundary layer - a higher-order-closure model study. *Bound. Layer Meteor.*, 7, 289-308.

———, and R. A. Brost, 1984: Top-down and bottom-up diffusion of a scalar in the convective boundary layer. *J. Atmos. Sci.*, **41**, 102-112.

Yamada, T. ,1977: A numerical experiment on pollutant dispersion in a horizontally-homogeneous atmospheric boundary layer. *Atmos. Environ.*, **11**, 1015-1024.

———, 1979: Prediction of the nocturnal surface inversion height. *J. Appl. Meteor.*, **18**, 526-531.

———, and G. Mellor, 1975: A simulation of the Wangara atmospheric boundary layer data. *J. Atmos. Sci.*, **32**, 2309-2329.

Yu, T. W., 1977: A comparitive study on parameterization of vertical turbulent exchange. *Mon. Wea. Rev.*, **105**, 55-66.

Zeman, O., 1975: The dynamics of entrainment in the planetary boundary layer: a study in turbulence modeling and parameterization. Ph.D. thesis, The Pennsylvania State University, 216 pp.

———, and J. Lumley, 1976: Modeling the buoyancy driven mixed layer. *J. Atmos. Sci.*, **33**, 1974-1988.

Zhang, D., and R. A. Anthes, 1982: A high-resolution model of the planetary boundary layer- Sensitivity tests and comparisons with SESAME-79 data. *J. Appl. Meteor.*, **21**, 1594-1609.

Zilitinkevich, S., 1970: *Dynamics of the Atmospheric Boundary Layer*. Hydrometeorol, Leningrad.

———, 1994: A generalized scaling for convective shear flows. *Bound Layer Meteor.*, **70**, 51-78.

———, 1995: Non-local turbulent transport: pollution dispersion aspects of coherent structure of convective flows. *Air Pollution III, Vol 1: Air Pollution Theory and Simulation*, H. Power, N. Moussiopoulos, C. A. Brebbia, Eds., Computational Mechanics Publications, 53-60.

APPENDIX: LIST OF SYMBOLS

a_i	constants for computation of ϵ_{vD} (= 0.6554, 0.1213, 1.552×10^{-2}, 1.856×10^{-3}, 9.430×10^{-5}, for i = 0 to 4, respectively)
A	arbitrary conserved mean variable
A'	turbulent component of arbitrary variable
A_1, A_2, A_3	constants for computation of SBL e (= 2.3, 1.7, 1.3, respectively)
b	exponent for analytic soil parameter equations
b_i	constants for computation of ϵ_{vU} (= 0.6039, 0.1513, 2.8234×10^{-2}, 4.1063×10^{-3}, 2.3803×10^{-5}, for i = 0 to 4, respectively)
B	Stefan-boltzmann function ($= \sigma T^4$)
c_p	specific heat of dry air at constant pressure (= 1004.7 J kg^{-1} K^{-1})
C, C'	functions for η_0 calculation
C_A	constant for K_A computation
C_d, C_s, C_w	dry soil, total soil, and liquid water (= 4186 J kg^{-1}) heat capacities, respectively
C_{ik}	constants for l_k and l_h computation (= 15, 11, 2.5×10^{-3}, 1, 3 for i = 1 to 5, respectively)
$C_{i\epsilon}$	constants for l_ϵ computation (= 15, 5, 5×10^{-3}, 1, 1.5 for i = 1 to 5, respectively)
C_ϵ	constant for ϵ computation (= 0.125)
d	downwind distance of plume travel
D_η	soil moisture diffusivity

e	turbulent kinetic energy
E_0	surface evaporation rate
f	coriolis parameter (for 34.5°S, = -8.26×10^{-5} s^{-1})
F_D, F_U	downward and upward longwave radiative flux, respectively
g	gravitational acceleration (= 9.81 m s^{-2})
H_G, H_L, H_S	surface soil, latent, and sensible heat fluxes, respectively
h	height of bottom-most atmospheric grid layer
h_g	one-half the depth of top-most soil grid layer
h_i	CBL height
h_s	NBL height
h_t	turbulent NBL height
k	von karman constant (= 0.40)
K	eddy diffusivity
K_A	eddy diffusivity appropriate for A
K_m, K_h, K_q, K_e	eddy diffusivities for momentum, heat, humidity, and turbulent kinetic energy, respectively
K_η	soil hydraulic conductivity
$K_{\eta s}$	saturation soil hydraulic conductivity
l, l_k	turbulent length scale
l_m, l_h, l_ϵ	turbulent length scales for momentum, heat, and molecular dissipation, respectively

l_s	length scale used to correct for locally stable conditions
l_{sbl}	SBL turbulent length scale
l_{sbl}^m, l_{sbl}^h	SBL turbulent length scales for momentum and heat, respectively
l_∞	free atmospheric length scale
L	Monin-Obukhov length
L_E	latent heat of evaporation (= 2.5×10^6 J kg^{-1})
m_{ik}, $m_{i\epsilon}$	factors for l_k and l_ϵ computation, respectively (i = 1,2)
m_{1m}, m_{1h}	factors analogous to m_{1k} for l_m and l_h computation, respectively
M_0	surface momentum flux
p	atmospheric pressure
p_0	reference surface pressure (= 1000 mb)
P	surface precipitation rate
q	atmospheric specific humidity
q_s	saturation specific humidity
q_0	surface specific humidity
$q_{1.2}$	1.2 meter specific humidity
$q_\star$	SBL specific humidity scale
Q_s	soil heat flux
r_i	ratio of negative heat flux at h_i to H_s
R_D, R_U	downward and upward surface longwave radiative flux, respectively

R_S	shortwave surface radiative flux
Ri	gradient Richardson number
Ri_c	critical gradient Richardson number
t	elapsed time of simulation
T	atmospheric temperature
T_s	soil temperature
T_0	surface temperature
$T_{1.2}$	1.2 meter temperature
u, v	zonal and meridional velocity components, respectively
u_g, v_g	zonal and meridional geostrophic velocity components, respectively
$u_\star$	Monin-Obukhov velocity scale
V	horizontal wind speed
V_g	geostrophic wind velocity
V_{16}	16 m horizontal wind speed
w_s	imposed large-scale subsidence velocity
w'	turbulent component of vertical velocity
$w_\star$	free convective velocity scale
W_0	surface soil moisture flux
W_s	soil moisture flux
y	northward coordinate

z	atmospheric vertical coordinate
z_R	top of extended model for computation of F_D
z_s	soil vertical coordinate
z_T	top of model
z_0, z_θ, z_q	aerodynamic (momentum), thermal, and humidity roughness lengths, respectively
z'	dummy variable of integration
$\tilde{z}$	height scale for χ computation

Greek

α	surface wetness function
β_i	Monin-Obukhov constants for stable conditions (= 1, 0.667, 5, 0.35 for i = 1 to 4, respectively)
γ_m, γ_h	Monin-Obukhov constants (unstable conditions) for momentum and heat, respectively (= 19.3, 11.6, respectively)
Δ	layer difference operator
ϵ_0	surface longwave emissivity
ϵ_D, ϵ_U	Total downward and upward longwave atmospheric emissivities, respectively
ϵ_{cD}, ϵ_{cU}	Downward and upward longwave emissivities, respectively, for carbon dioxide
ϵ_{vD}, ϵ_{vU}	Downward and upward longwave emissivities, respectively, for water vapor
ζ	Monin-Obukhov stability parameter (= z/L)

η	volumetric soil moisture content
η_0	surface volumetric soil moisture content
η_{fc}	volumetric soil moisture content at field capacity
η_s	saturation volumetric soil moisture content
θ	potential temperature
θ_a	domain averaged potential temperature
θ_v	virtual potential temperature
$\theta_\star$	Monin-Obukhov potential temperature scale
λ	soil thermal conductivity
ρ	atmospheric density
ρ_0	reference surface atmospheric density (= 1.23 kg m^{-3})
ρ_c	mass concentration of carbon dioxide (= 350 ppm)
ρ_w	density of liquid water (= 1000 kg m^{-3})
σ	Stefan-boltzmann constant (= 5.67×10^{-8} W m^{-2} K^{-4})
σ_u, σ_v, σ_w	horizontal and vertical components of momentum variance
σ_z	vertical diffusion coefficient
ϕ_m, ϕ_h, ϕ_q	Monin-Obukhov non-dimensional momentum, heat, and humidity gradients, respectively
χ	scaling factor in length scale formulation
ψ	soil matrix potential
ψ_s	saturation soil matrix potential

ω_{cD}, ω_{cU}	Downward and upward optical path lengths, respectively, for carbon dioxide
ω_{vD}, ω_{vU}	Downward and upward optical path lengths, respectively, for water vapor

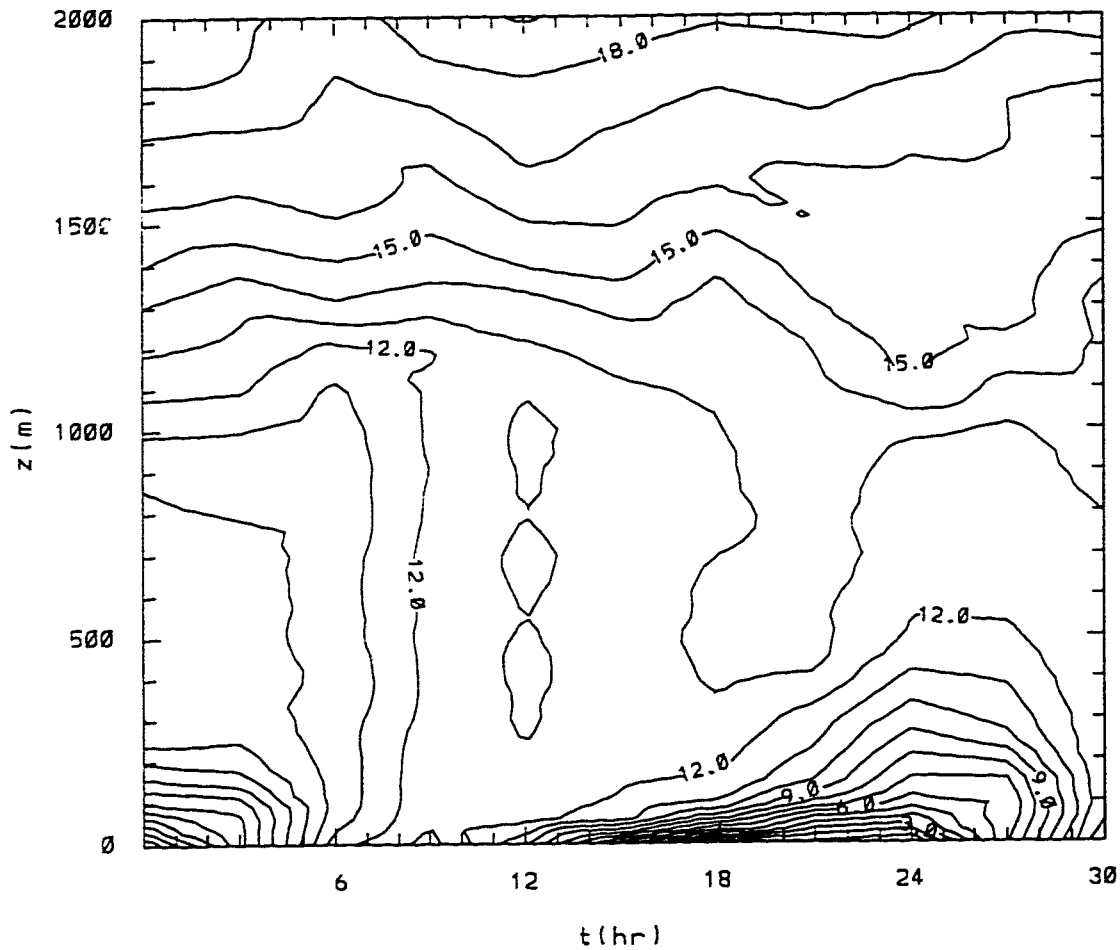
2000
1500
1000
500
0
z(m)
18.0
15.0
15.0
15.0
12.0
12.0
12.0
12.0
9.0
6.0
3.0
0.0
6
12
18
24
30
t(hr)

Fig. 1

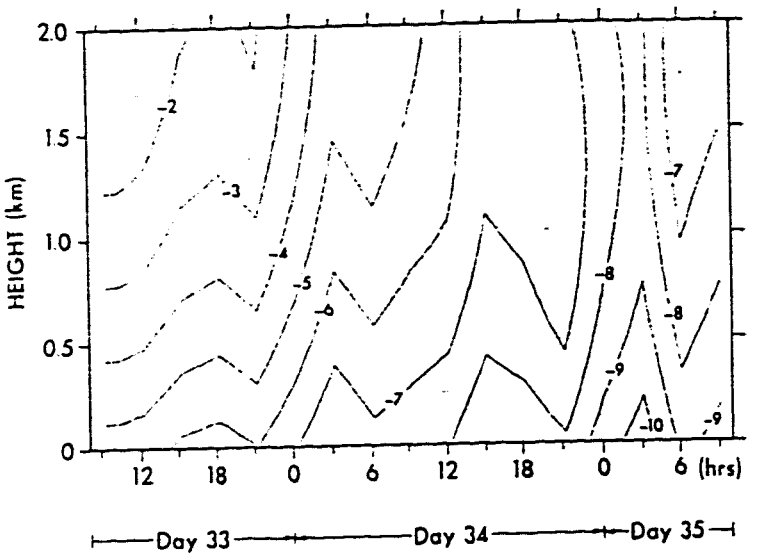
HEIGHT (km)
2.0
1.5
1.0
0.5
0
12
18
0
6
12
18
0
6 (hrs)
Day 33
Day 34
Day 35

(a)

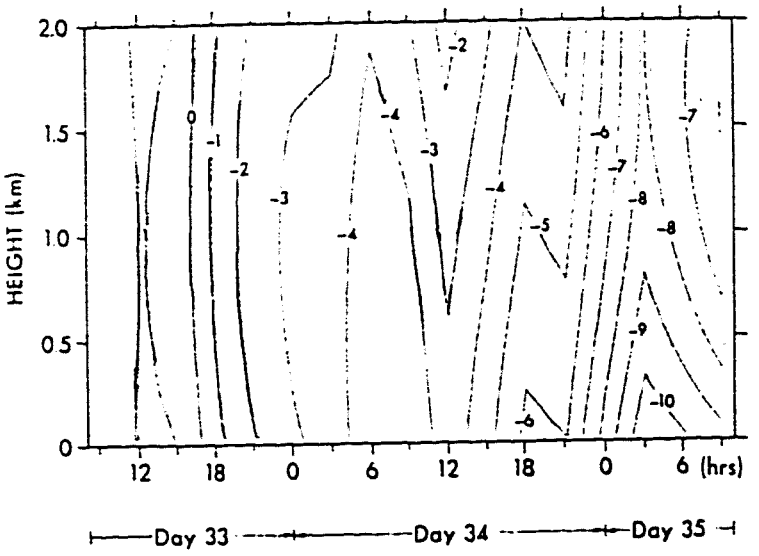
HEIGHT (km)
2.0
1.5
1.0
0.5
0
12
18
0
6
12
18
0
6 (hrs)
Day 33
Day 34
Day 35

(b)

Fig. 2

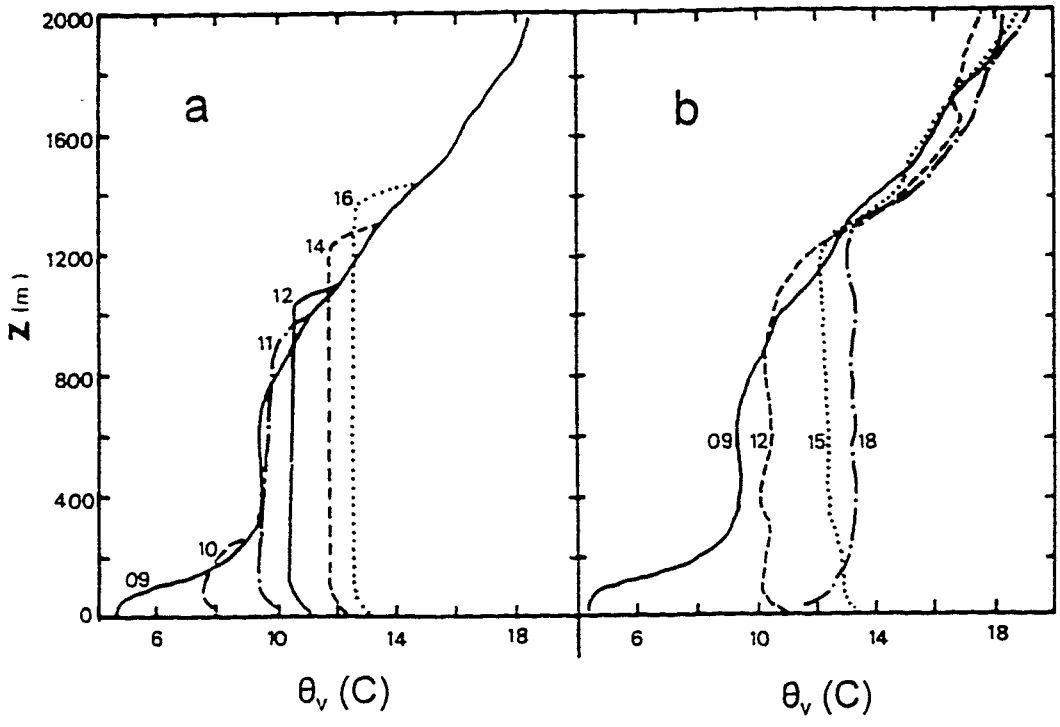

Fig. 3

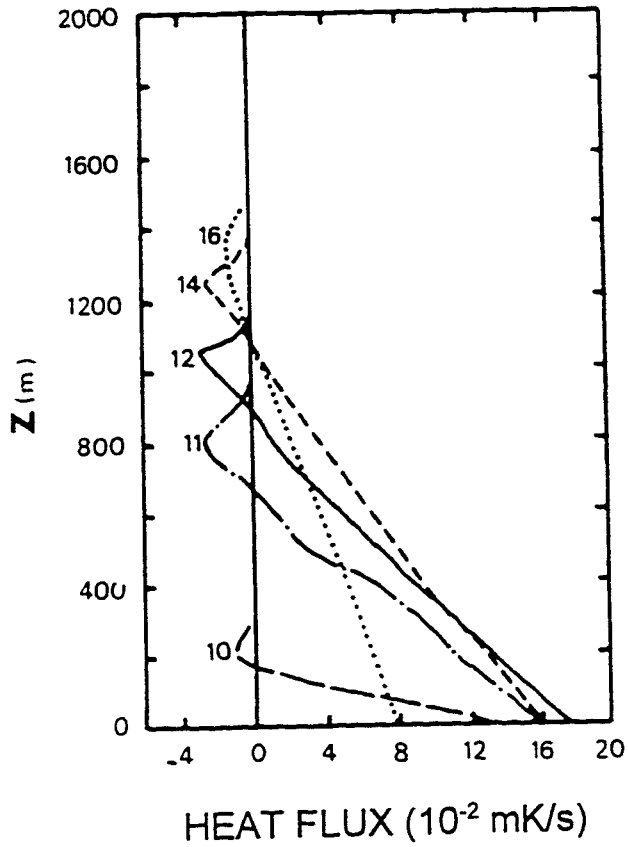
2000
1600
1200
800
400
0
Z (m)
16
14
12
11
10
-4
0
4
8
12
16
20
HEAT FLUX (10-2 mK/s)

Fig. 4

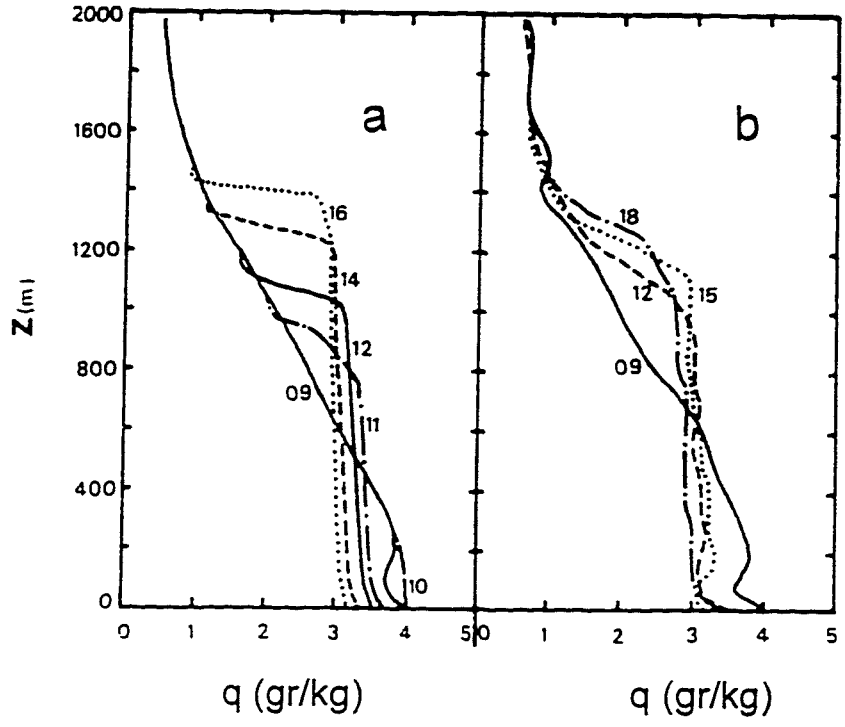
2000
1600
1200
800
400
0
z (m)
a
b
16
14
12
09
11
10
18
12
15
09
0
1
2
3
4
5
q (gr/kg)
q (gr/kg)

Fig. 5

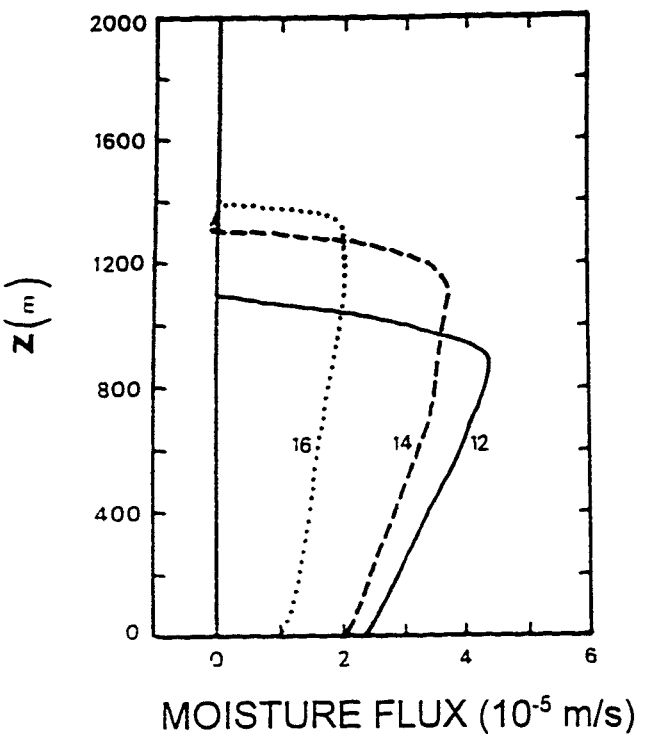

Fig. 6

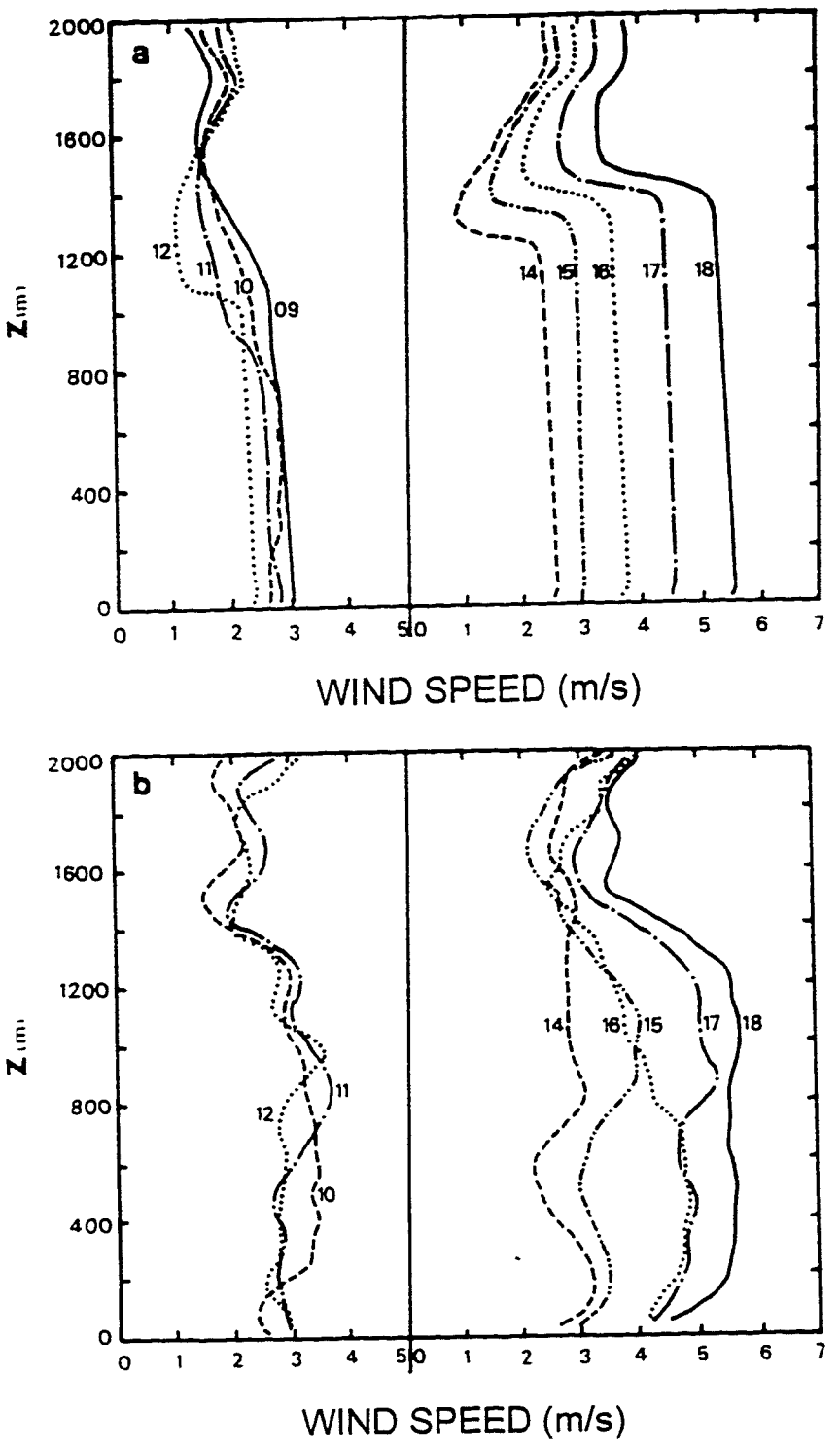
a
2000
1600
1200
800
400
0
Z (m)
12
11
10
09
14
15
16
17
18
0 1 2 3 4 5
0 1 2 3 4 5 6 7
WIND SPEED (m/s)
b
2000
1600
1200
800
400
0
Z (m)
11
12
10
14
16
15
17
18
0 1 2 3 4 5
0 1 2 3 4 5 6 7
WIND SPEED (m/s)

Fig. 7

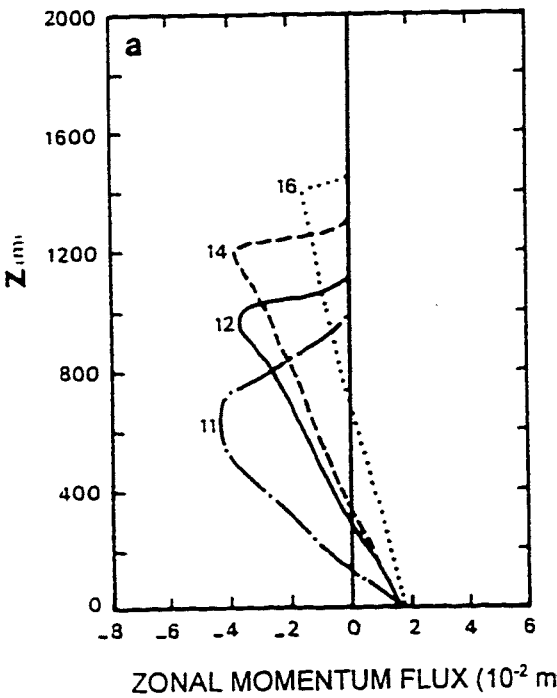
a
2000
1600
1200
800
400
0
z (m)
16
14
12
11
-8
-6
-4
-2
0
2
4
6
ZONAL MOMENTUM FLUX (10-2 m2/s2)

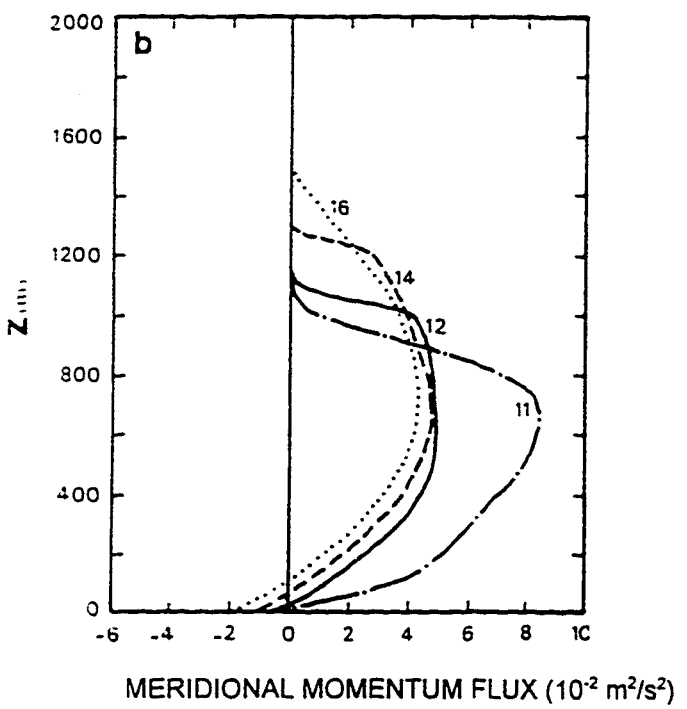
b
2000
1600
1200
800
400
0
z (m)
16
14
12
11
-6
-4
-2
0
2
4
6
8
10
MERIDIONAL MOMENTUM FLUX (10-2 m2/s2)

Fig. 8

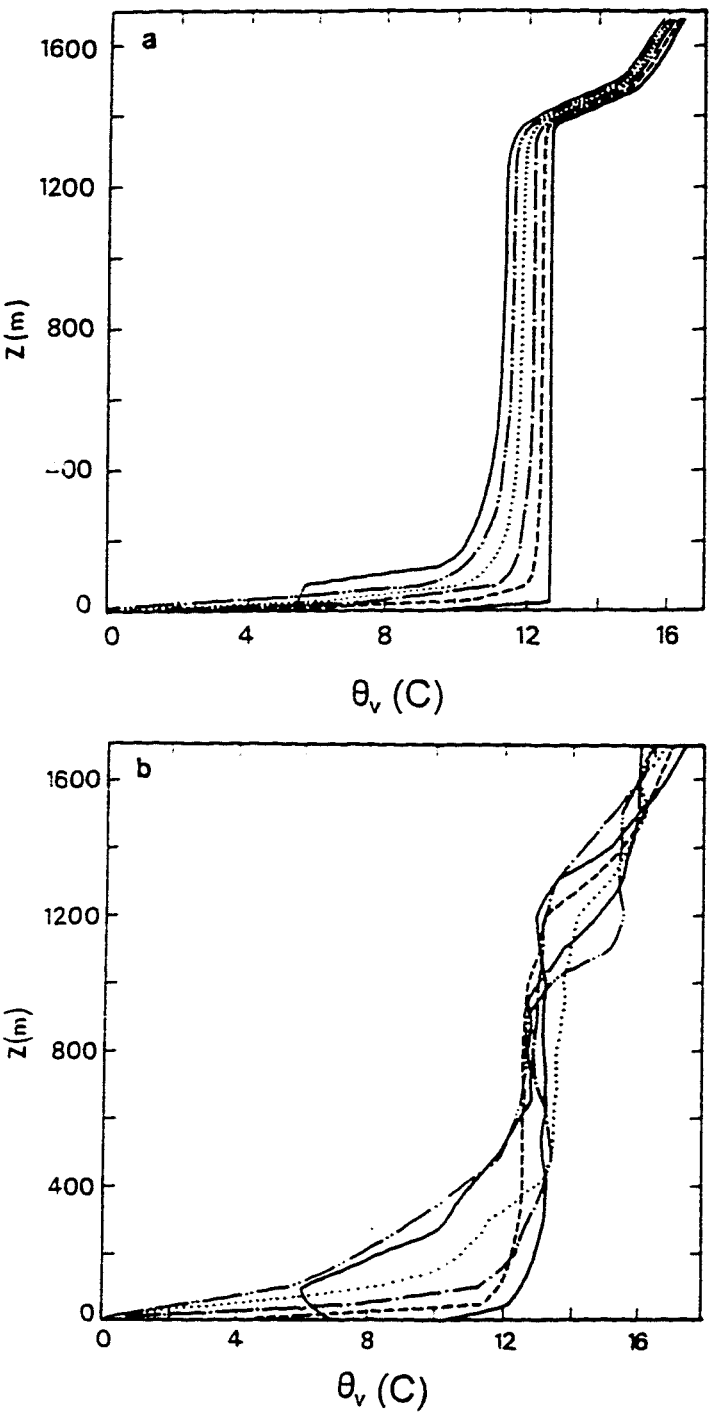
a
1600
1200
800
400
0
Z(m)
0
4
8
12
16
θv (C)
b
1600
1200
800
400
0
Z(m)
0
4
8
12
16
θv (C)

Fig. 9

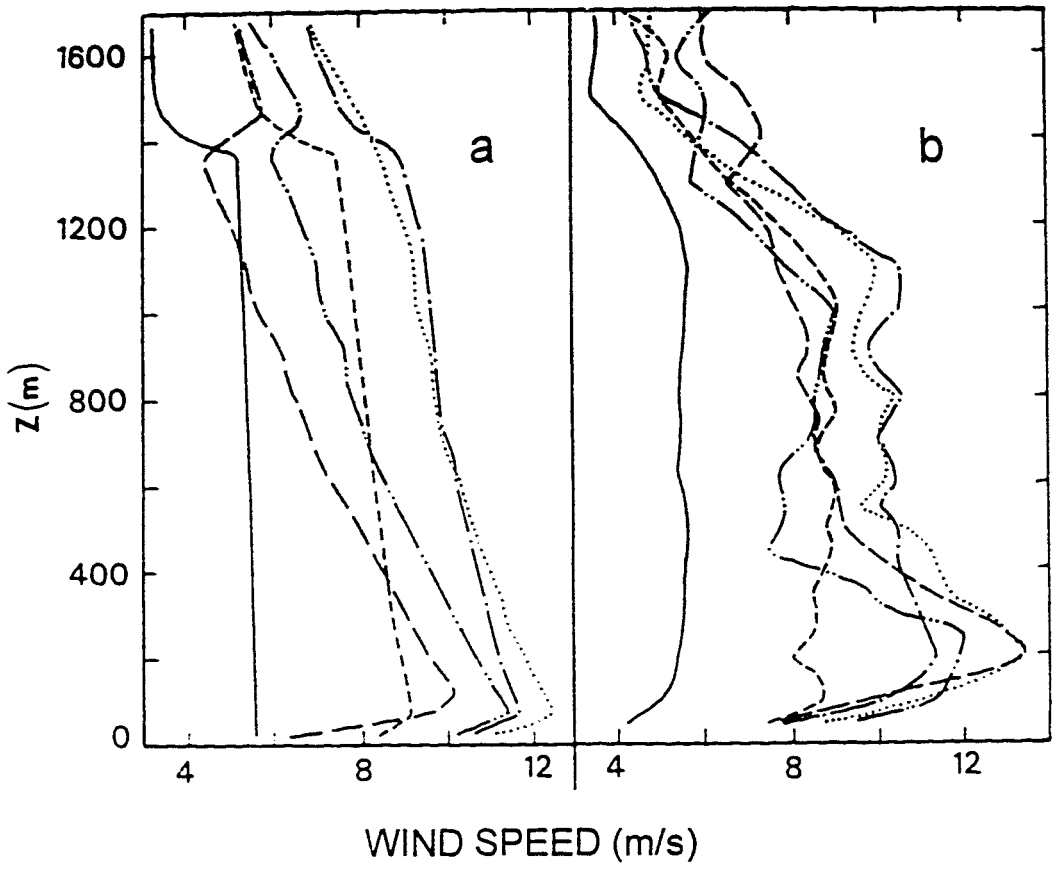

Fig. 10

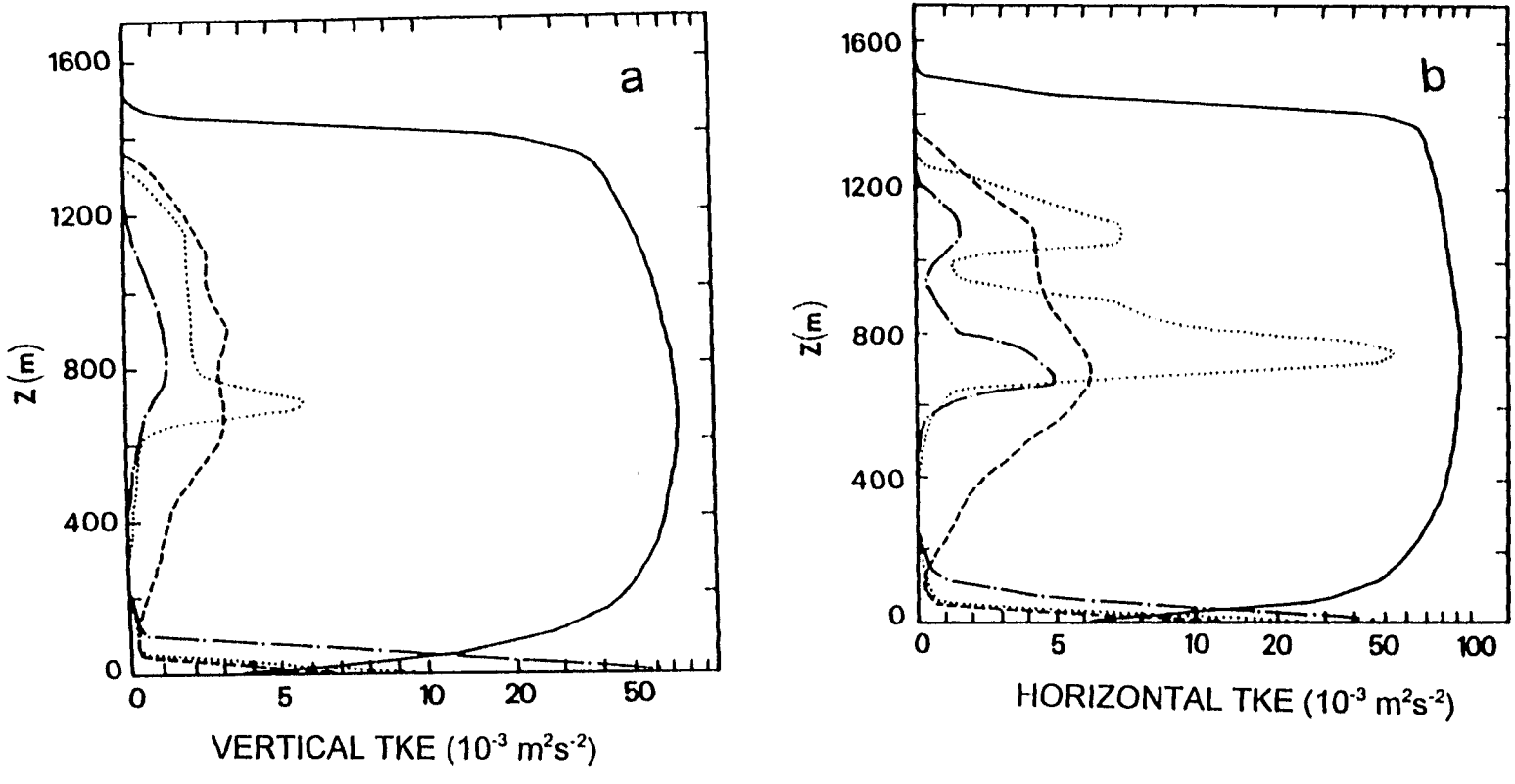
a
b
1600
1200
800
400
0
Z(m)
0
5
10
20
50
100
VERTICAL TKE (10^{-3} m^2s^{-2})
HORIZONTAL TKE (10^{-3} m^2s^{-2})

Fig. 11

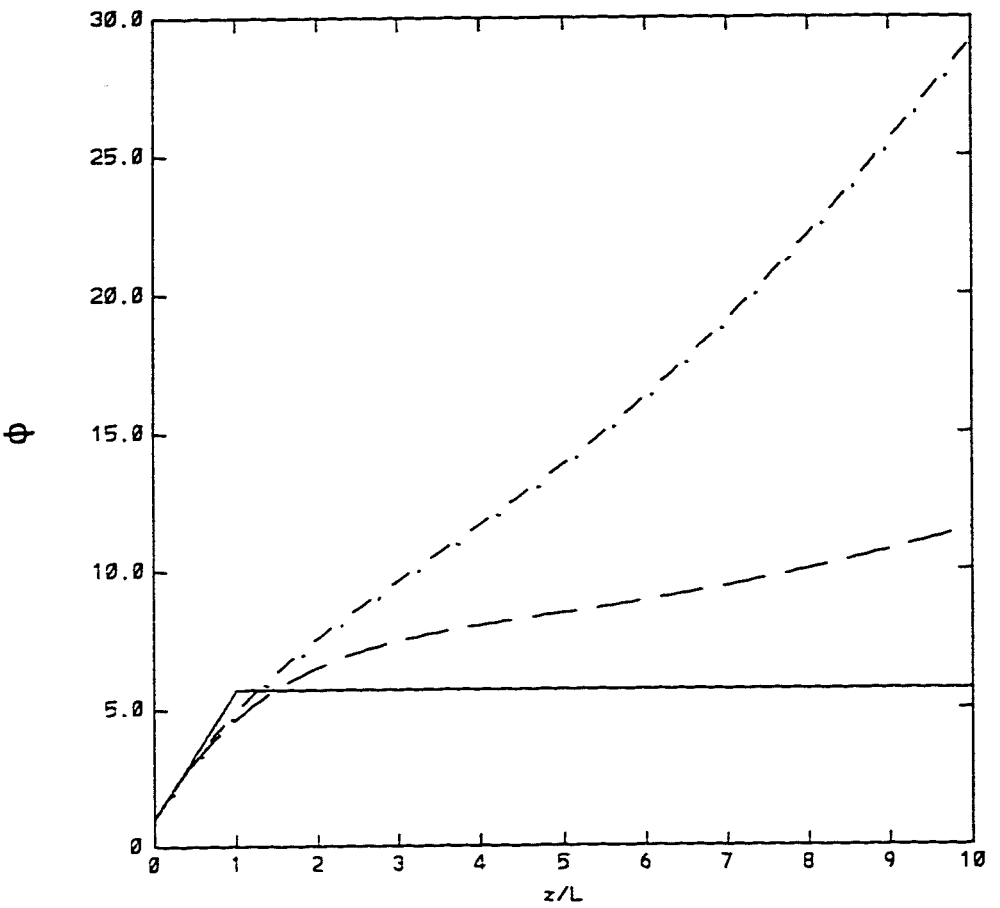

Fig. 12

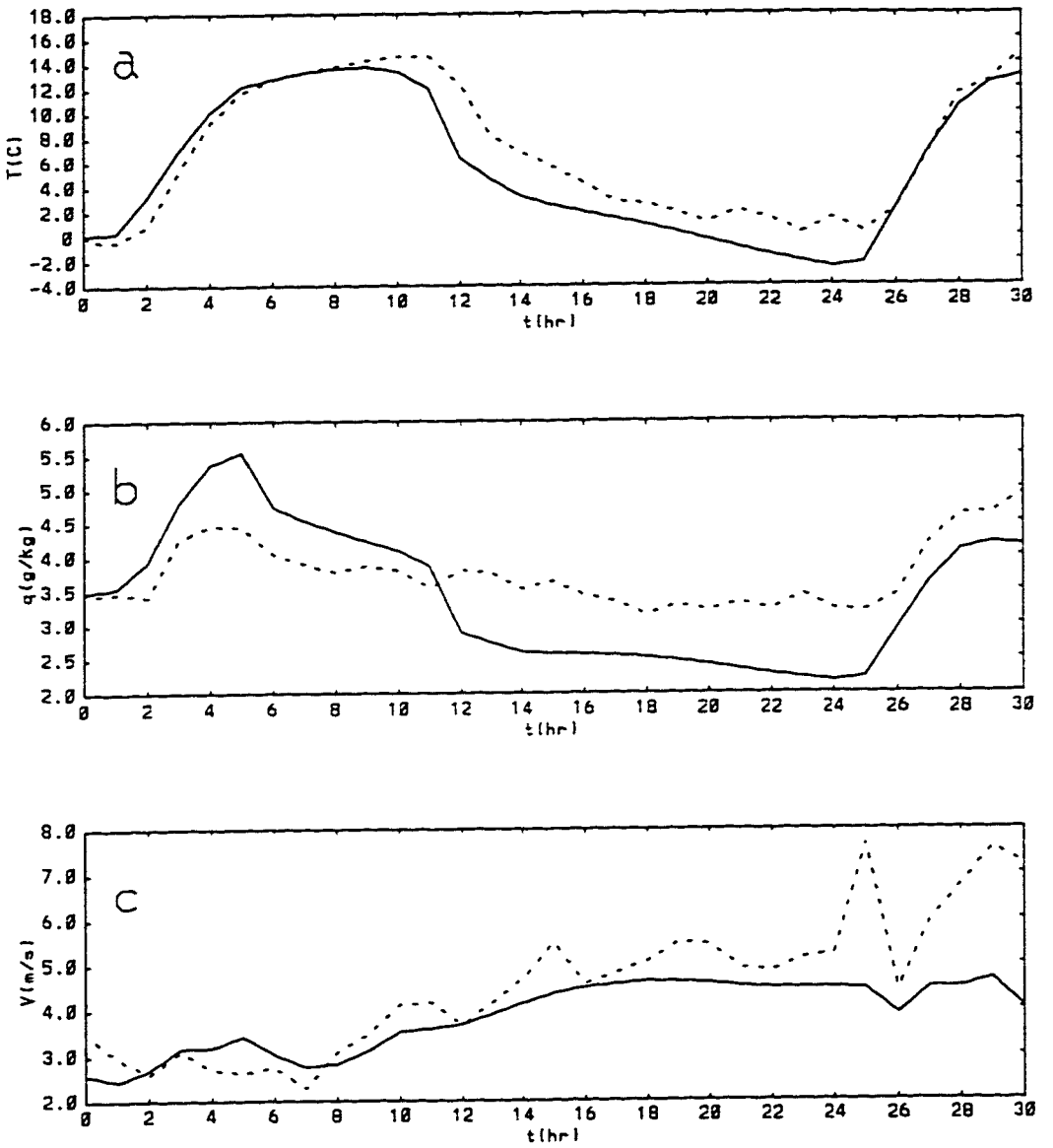
a
T(C)
18.0
16.0
14.0
12.0
10.0
8.0
6.0
4.0
2.0
0
-2.0
-4.0
0 2 4 6 8 10 12 14 16 18 20 22 24 26 28 30
t(hr)
b
q(g/kg)
6.0
5.5
5.0
4.5
4.0
3.5
3.0
2.5
2.0
0 2 4 6 8 10 12 14 16 18 20 22 24 26 28 30
t(hr)
c
V(m/s)
8.0
7.0
6.0
5.0
4.0
3.0
2.0
0 2 4 6 8 10 12 14 16 18 20 22 24 26 28 30
t(hr)

Fig. 13

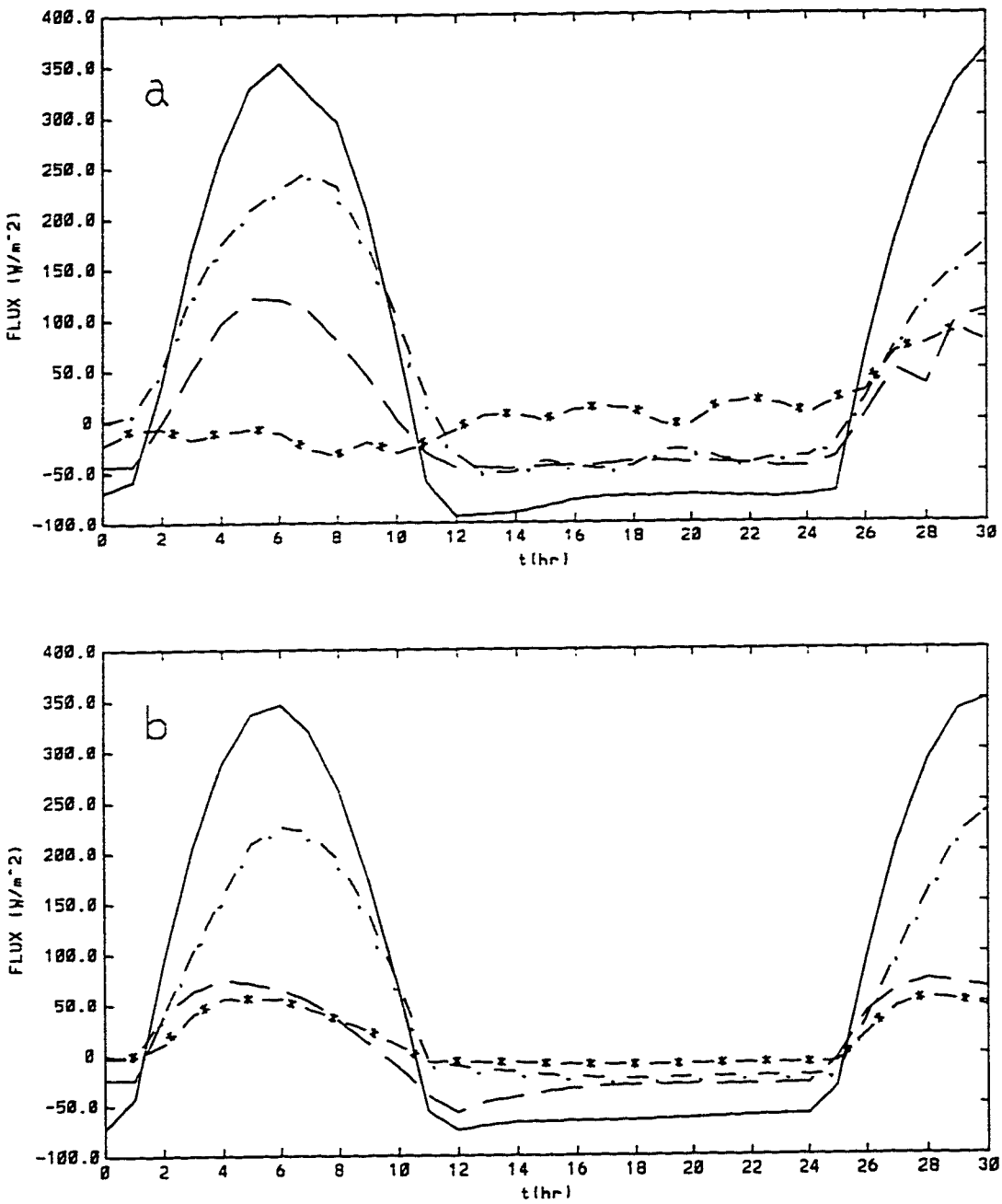
a
b
FLUX (W/m^2)
t(hr)
400.0
350.0
300.0
250.0
200.0
150.0
100.0
50.0
0
-50.0
-100.0
0
2
4
6
8
10
12
14
16
18
20
22
24
26
28
30

Fig. 14

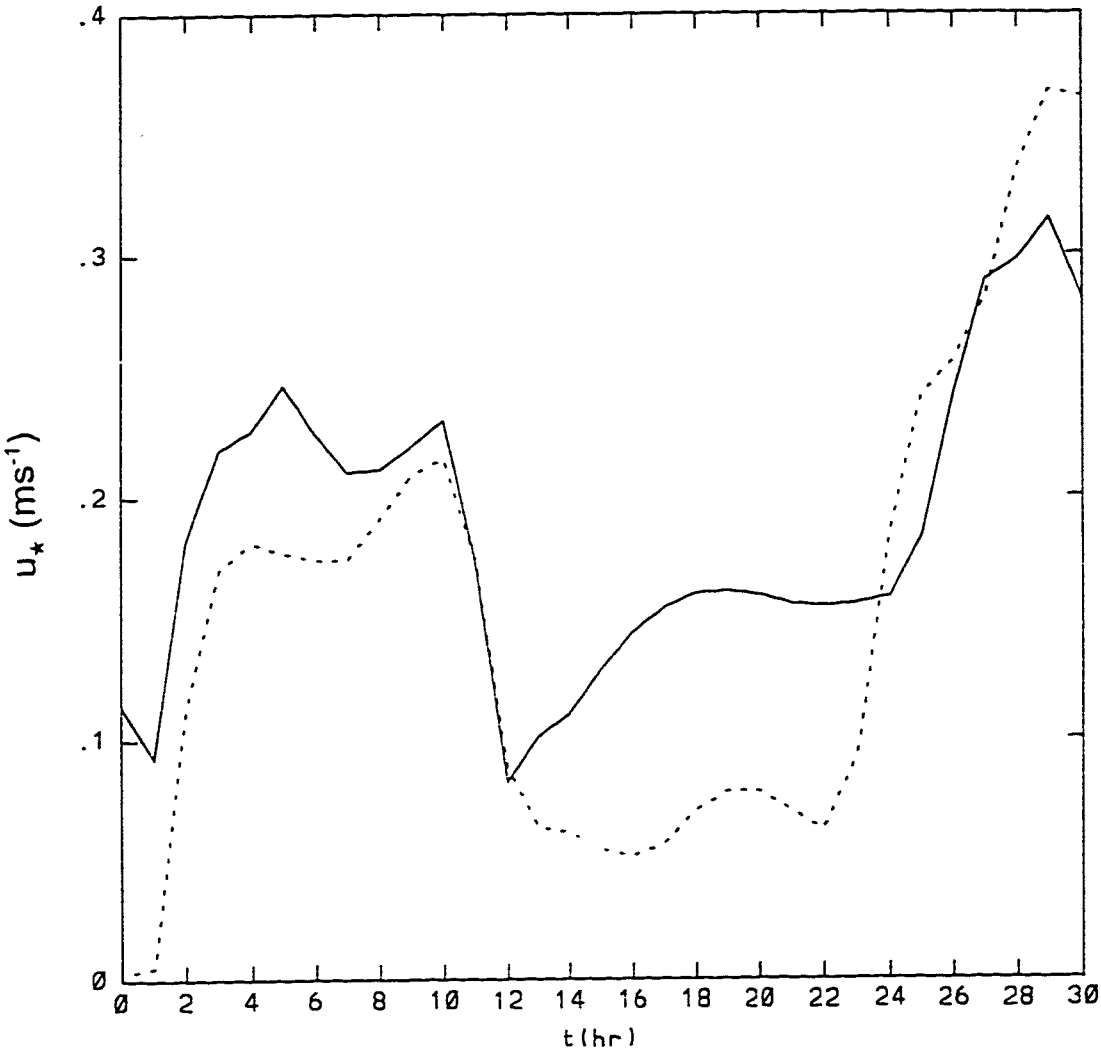

Fig. 15

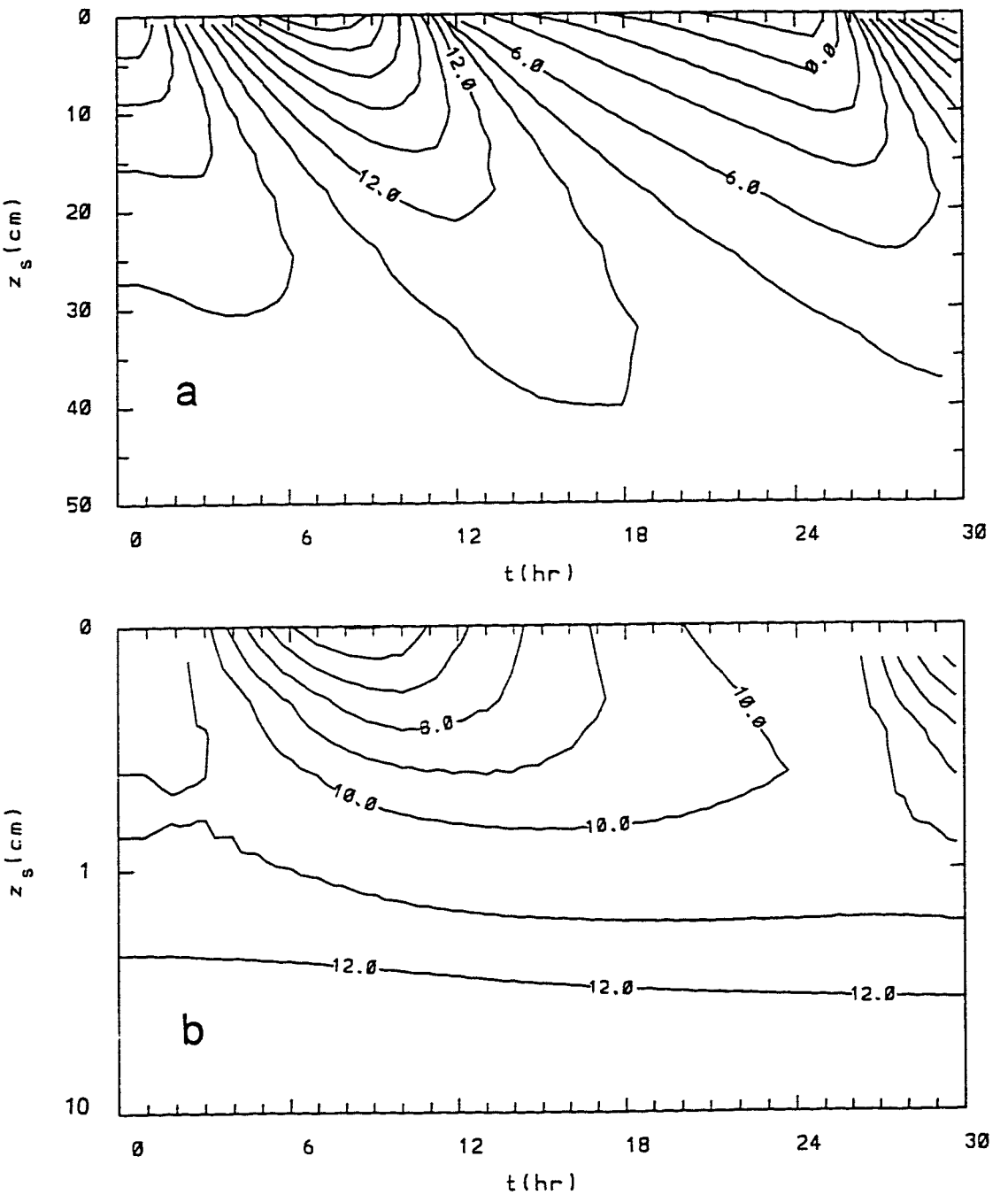
0
10
20
30
40
50
z s (cm)
12.0
6.0
0.0
6.0
12.0
a
0
6
12
18
24
30
t(hr)
0
1
10
z s (cm)
8.0
10.0
10.0
10.0
12.0
12.0
12.0
b
0
6
12
18
24
30
t(hr)

Fig. 16

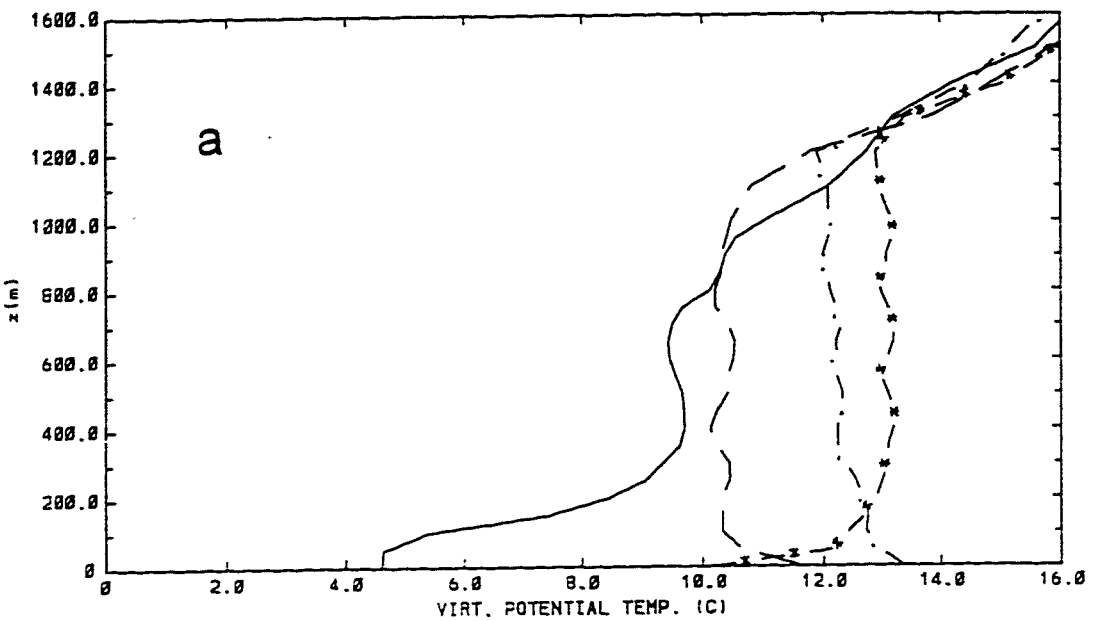
a
1600.0
1400.0
1200.0
1000.0
800.0
600.0
400.0
200.0
0
z(m)
0
2.0
4.0
6.0
8.0
10.0
12.0
14.0
16.0
VIRT. POTENTIAL TEMP. (C)

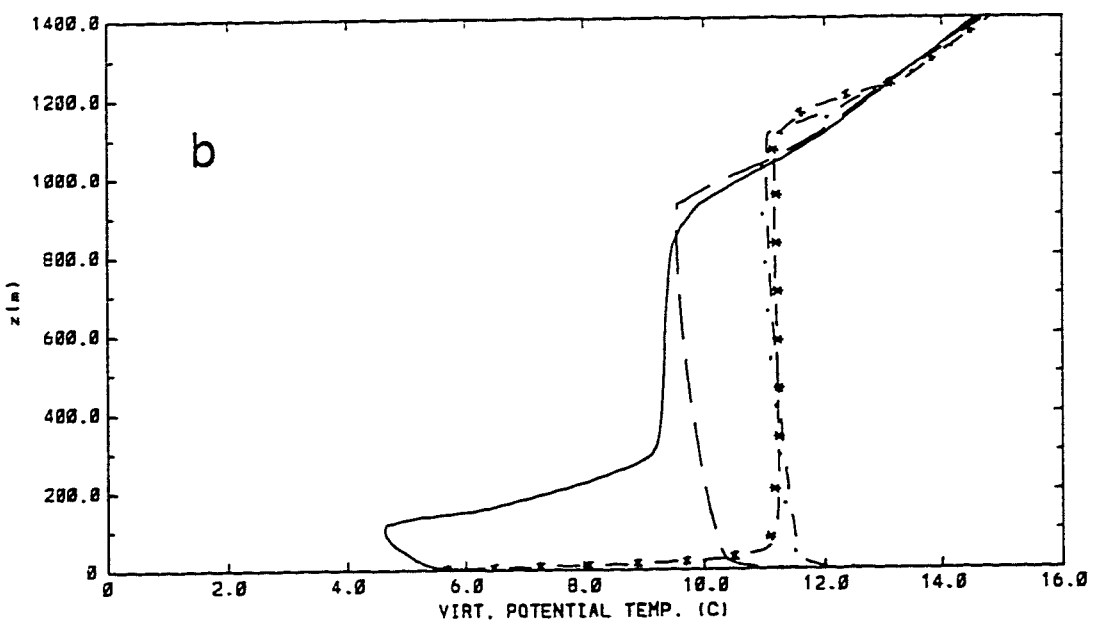
b
1400.0
1200.0
1000.0
800.0
600.0
400.0
200.0
0
z(m)
0
2.0
4.0
6.0
8.0
10.0
12.0
14.0
16.0
VIRT. POTENTIAL TEMP. (C)

Fig. 17

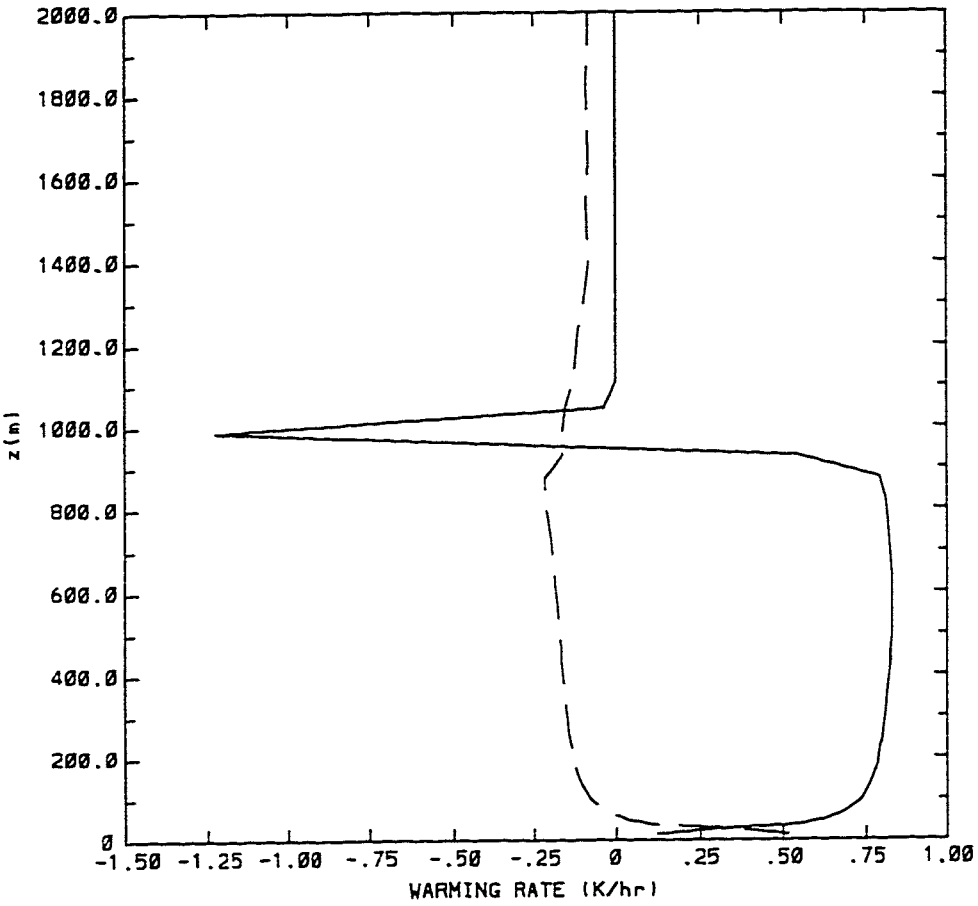
2000.0
1800.0
1600.0
1400.0
1200.0
1000.0
800.0
600.0
400.0
200.0
0
z(m)
-1.50 -1.25 -1.00 -.75 -.50 -.25 0 .25 .50 .75 1.00
WARMING RATE (K/hr)

Fig. 18

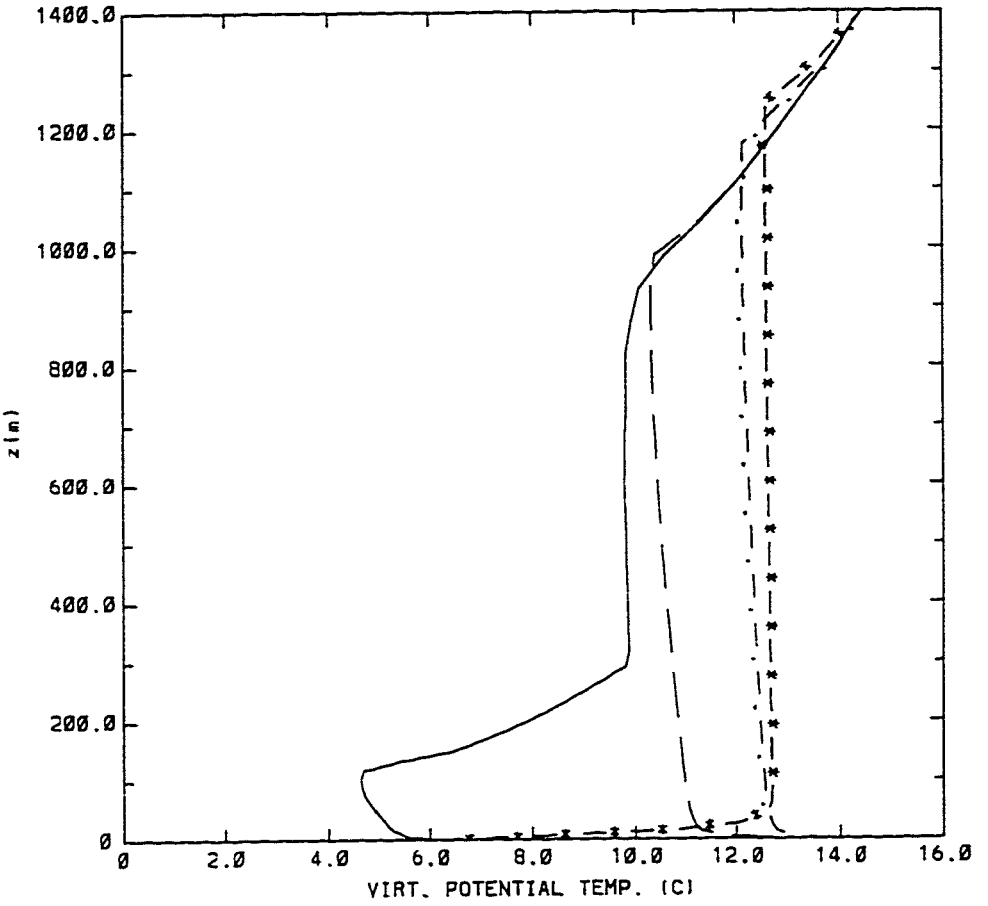
1400.0
1200.0
1000.0
800.0
600.0
400.0
200.0
0
z(m)
0
2.0
4.0
6.0
8.0
10.0
12.0
14.0
16.0
VIRT. POTENTIAL TEMP. (C)

Fig. 19

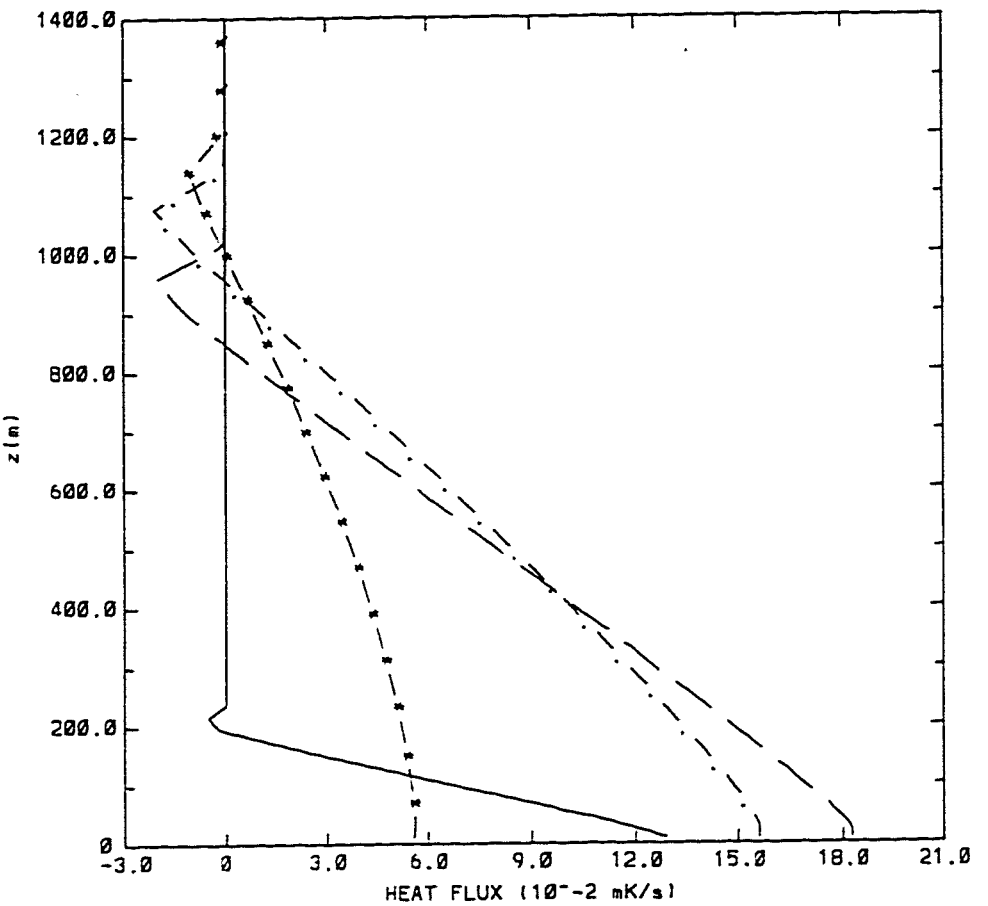
1400.0
1200.0
1000.0
800.0
600.0
400.0
200.0
0
z(m)
-3.0
0
3.0
6.0
9.0
12.0
15.0
18.0
21.0
HEAT FLUX (10^-2 mK/s)

Fig. 20

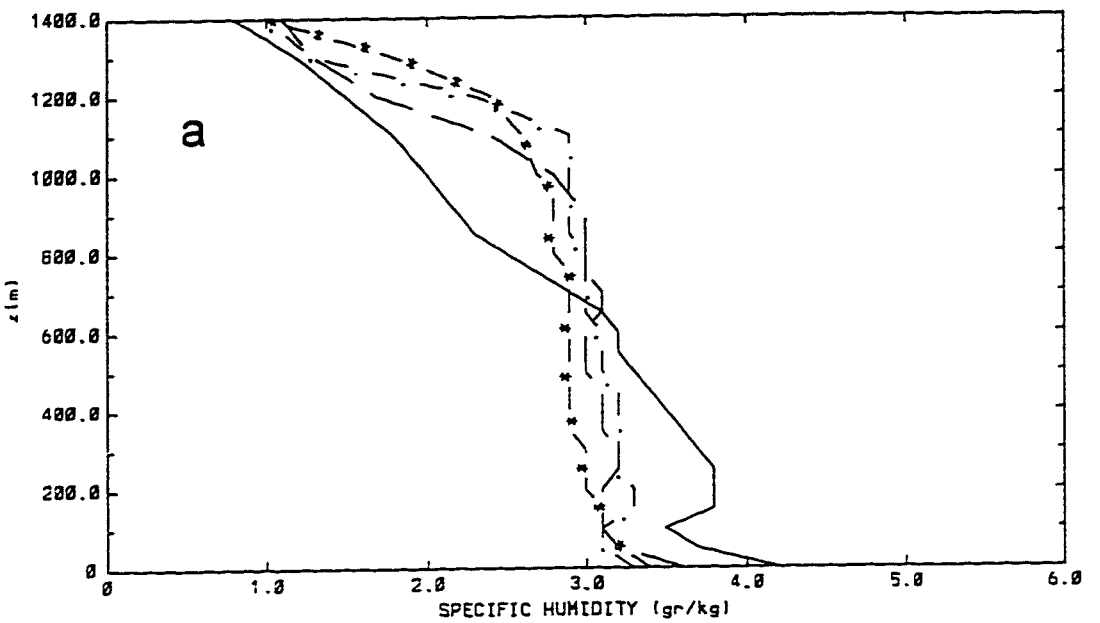
a
1400.0
1200.0
1000.0
800.0
600.0
400.0
200.0
0
z(m)
0
1.0
2.0
3.0
4.0
5.0
6.0
SPECIFIC HUMIDITY (gr/kg)

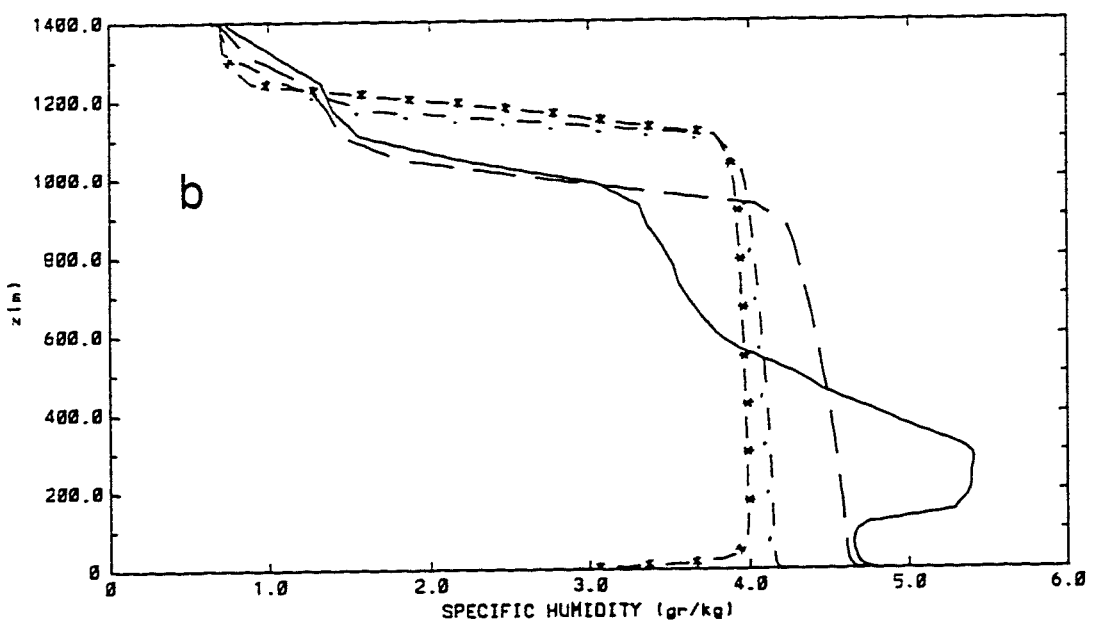
b
1400.0
1200.0
1000.0
800.0
600.0
400.0
200.0
0
z(m)
0
1.0
2.0
3.0
4.0
5.0
6.0
SPECIFIC HUMIDITY (gr/kg)

Fig. 21

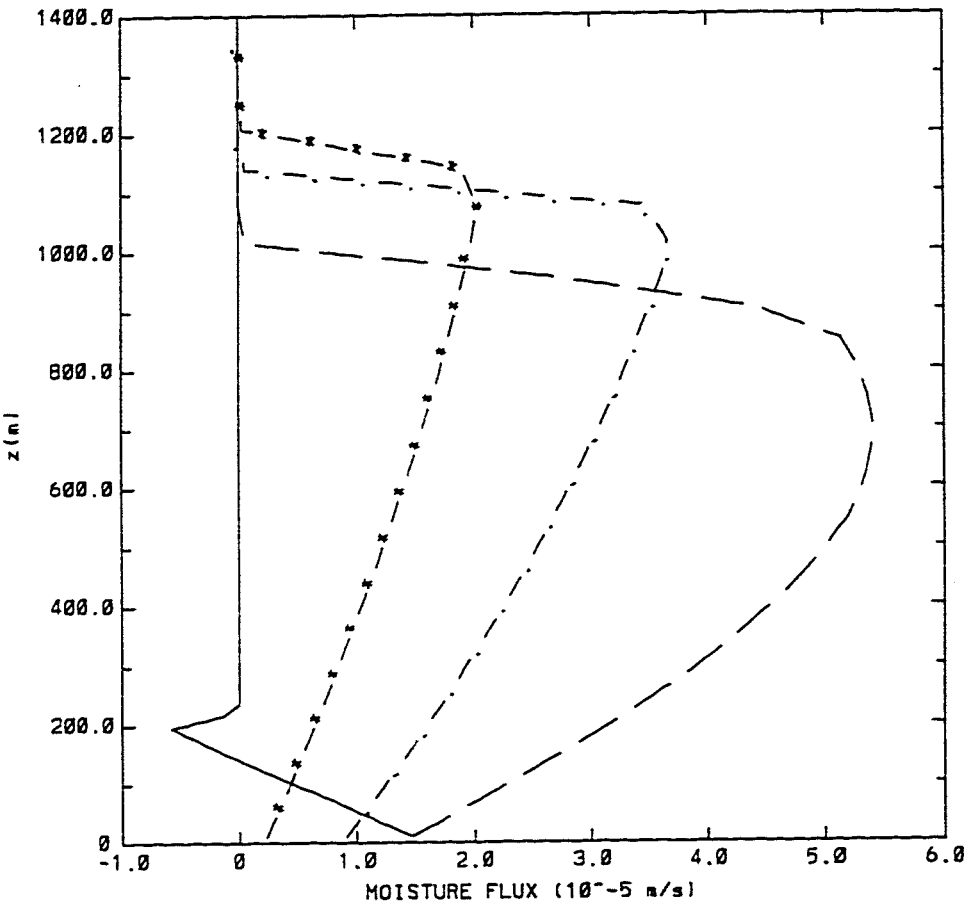
1400.0
1200.0
1000.0
800.0
600.0
400.0
200.0
0
z(m)
-1.0
0
1.0
2.0
3.0
4.0
5.0
6.0
MOISTURE FLUX (10^-5 m/s)

Fig. 22

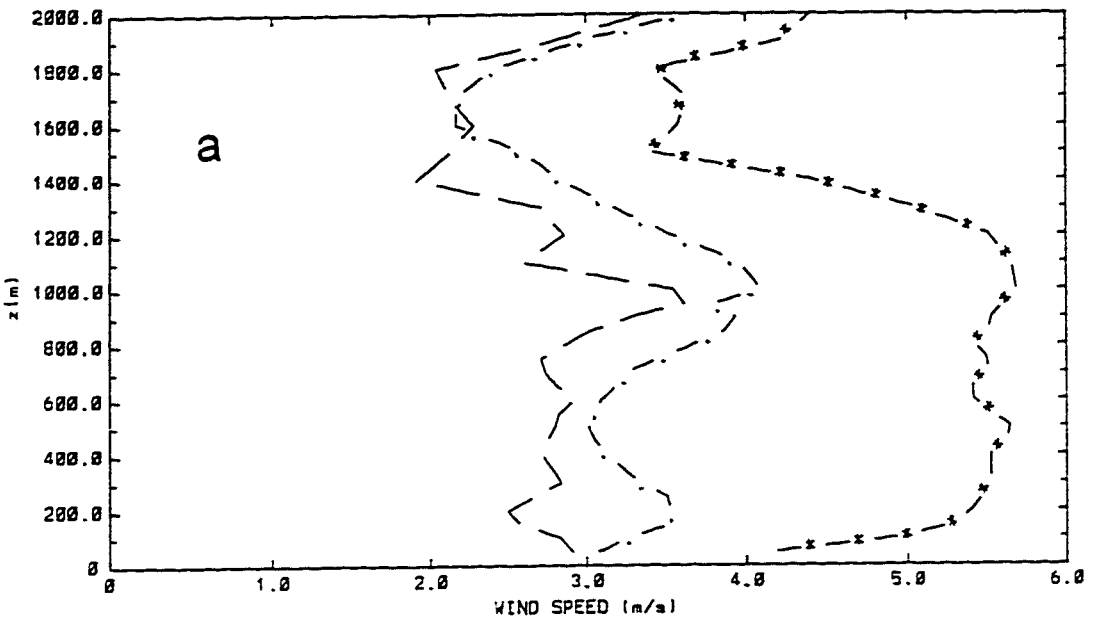
a
2000.0
1800.0
1600.0
1400.0
1200.0
1000.0
800.0
600.0
400.0
200.0
0
z(m)
0
1.0
2.0
3.0
4.0
5.0
6.0
WIND SPEED (m/s)

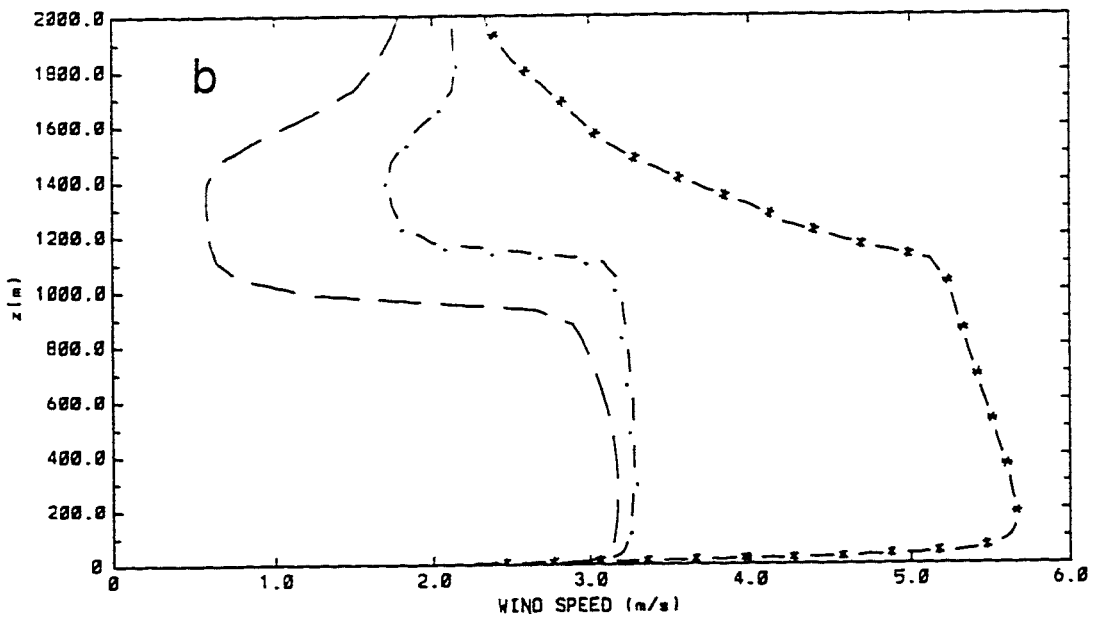
b
2000.0
1800.0
1600.0
1400.0
1200.0
1000.0
800.0
600.0
400.0
200.0
0
z(m)
0
1.0
2.0
3.0
4.0
5.0
6.0
WIND SPEED (m/s)

Fig. 23

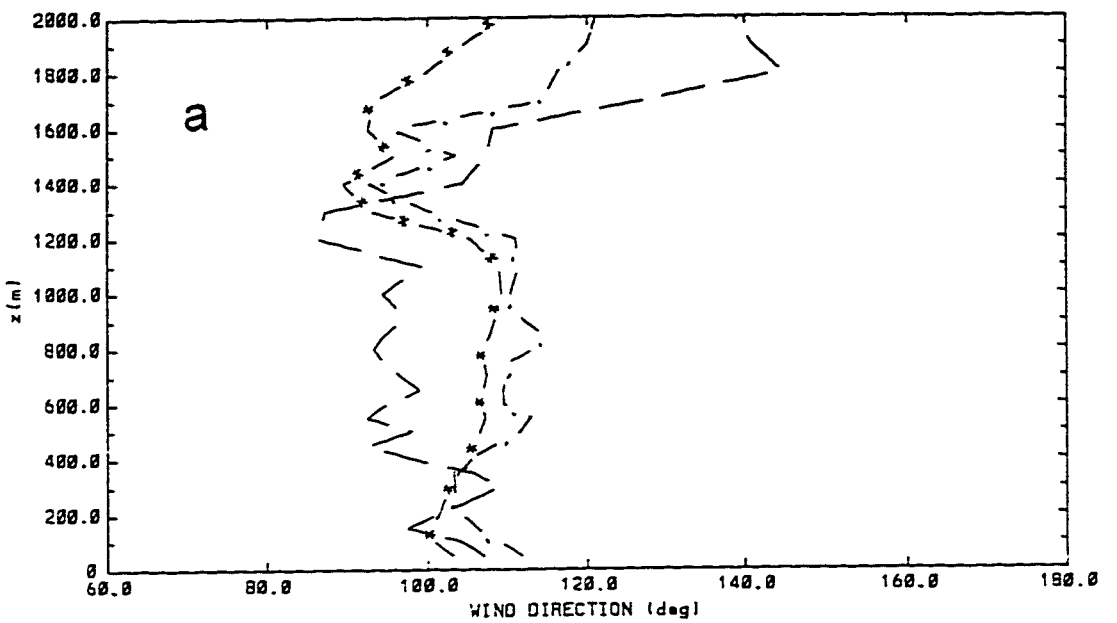
a
2000.0
1800.0
1600.0
1400.0
1200.0
1000.0
800.0
600.0
400.0
200.0
0
z (m)
60.0
80.0
100.0
120.0
140.0
160.0
180.0
WIND DIRECTION (deg)

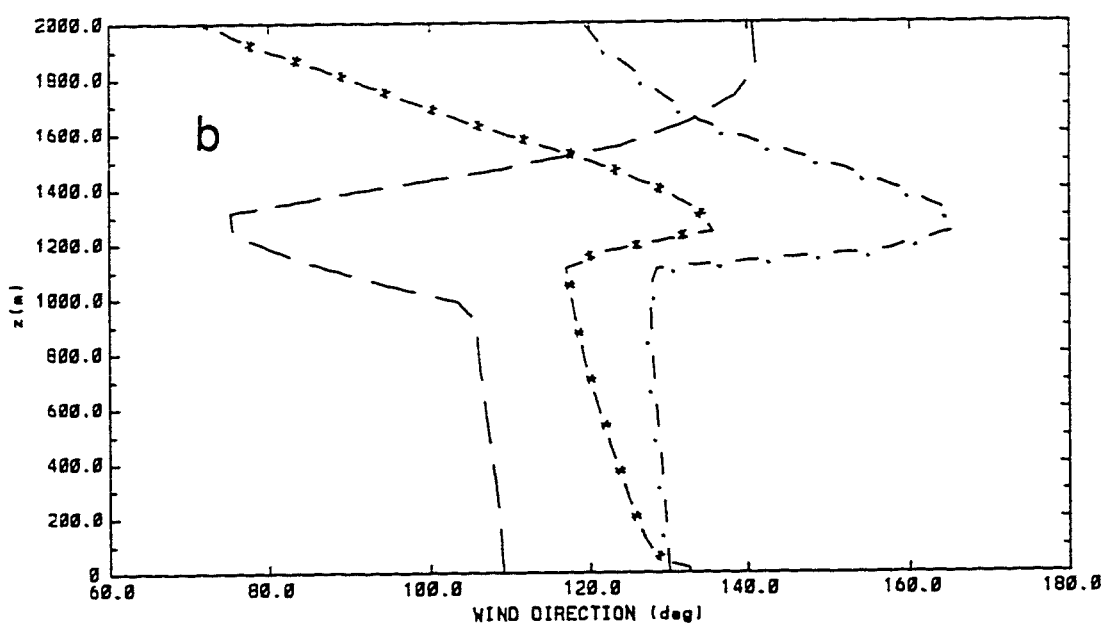
b
2000.0
1800.0
1600.0
1400.0
1200.0
1000.0
800.0
600.0
400.0
200.0
0
z (m)
60.0
80.0
100.0
120.0
140.0
160.0
180.0
WIND DIRECTION (deg)

Fig. 24

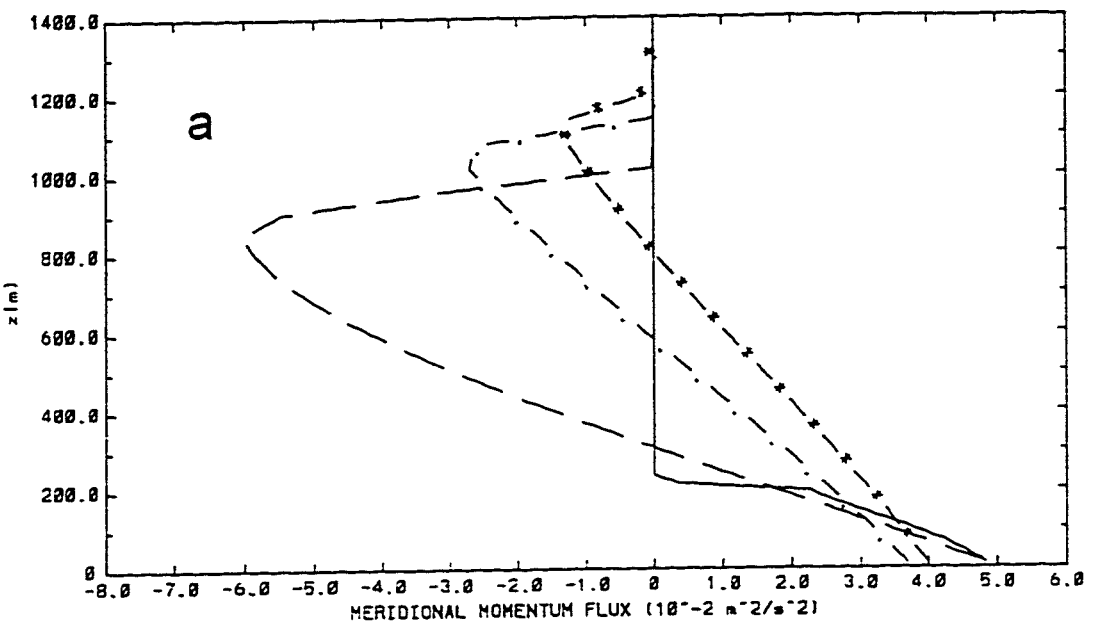
a
1400.0
1200.0
1000.0
800.0
600.0
400.0
200.0
0
z(m)
-8.0 -7.0 -6.0 -5.0 -4.0 -3.0 -2.0 -1.0 0 1.0 2.0 3.0 4.0 5.0 6.0
MERIDIONAL MOMENTUM FLUX (10^-2 m^2/s^2)

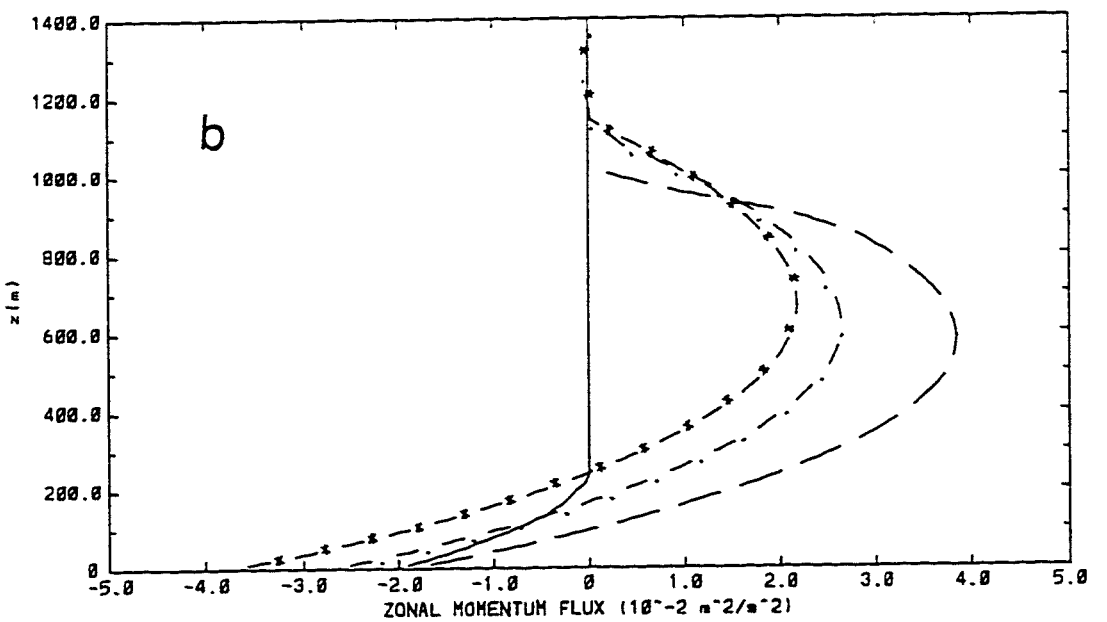
b
1400.0
1200.0
1000.0
800.0
600.0
400.0
200.0
0
z(m)
-5.0 -4.0 -3.0 -2.0 -1.0 0 1.0 2.0 3.0 4.0 5.0
ZONAL MOMENTUM FLUX (10^-2 m^2/s^2)

Fig. 25

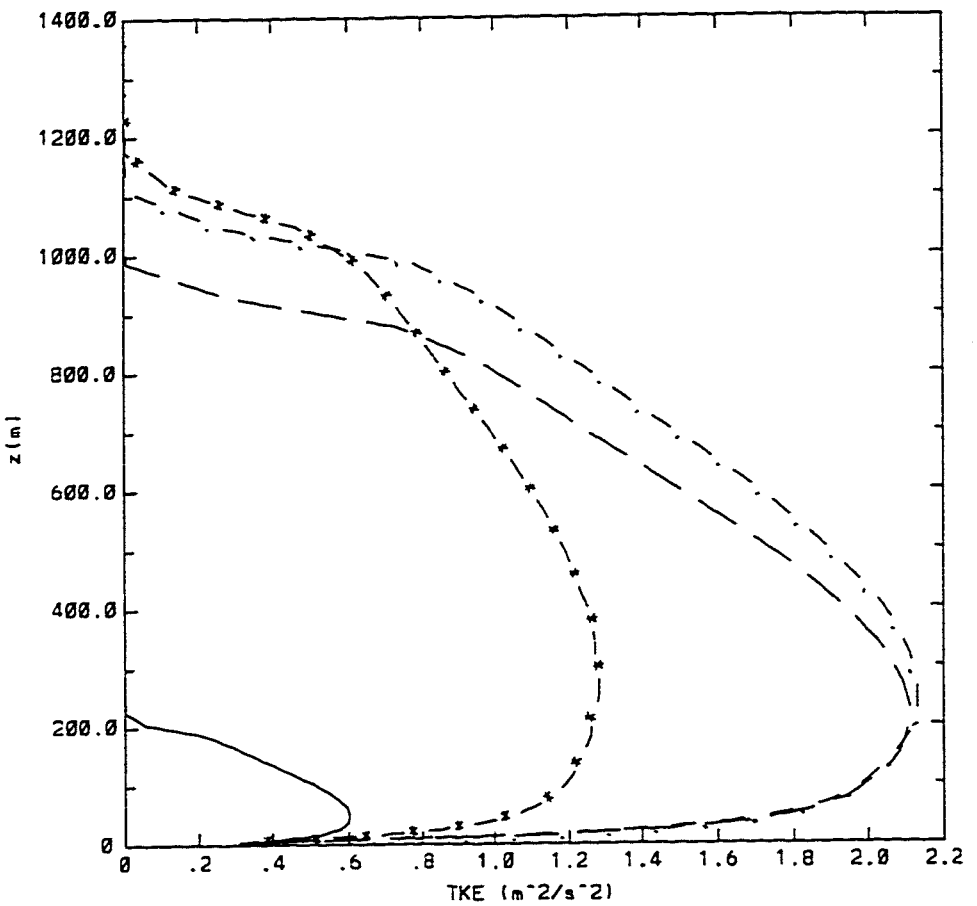
1400.0
1200.0
1000.0
800.0
600.0
400.0
200.0
0
z(m)
0
.2
.4
.6
.8
1.0
1.2
1.4
1.6
1.8
2.0
2.2
TKE (m^2/s^2)

Fig. 26

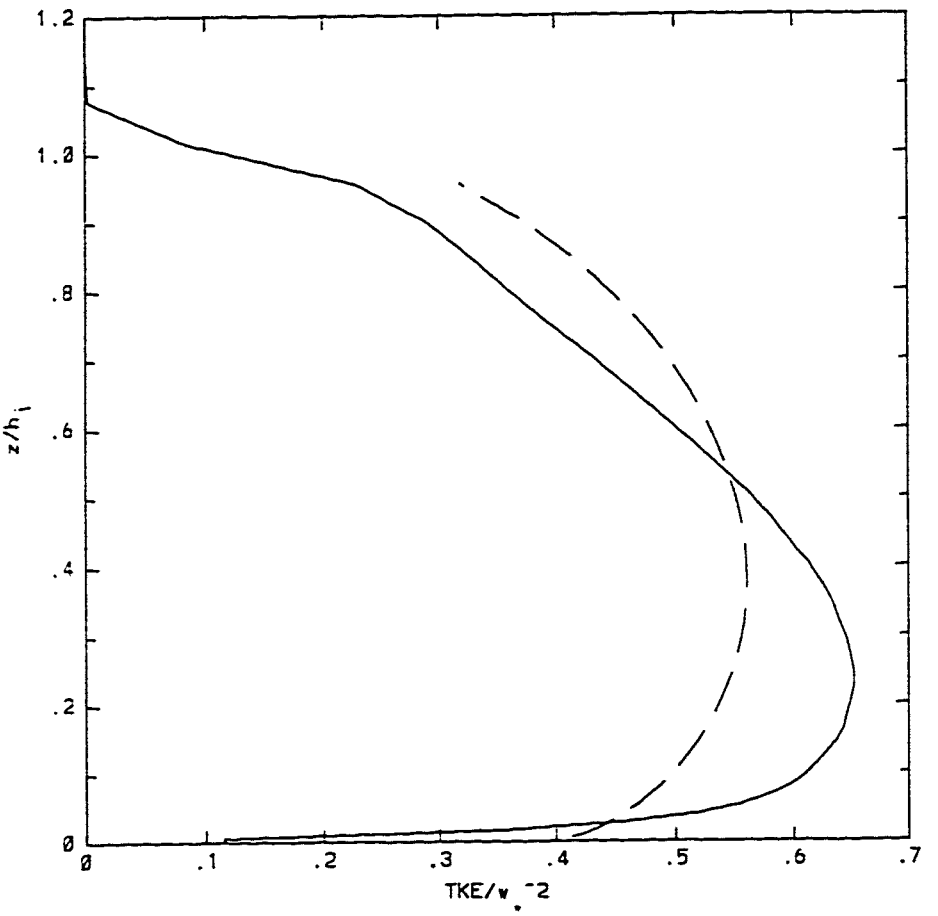

Fig. 27

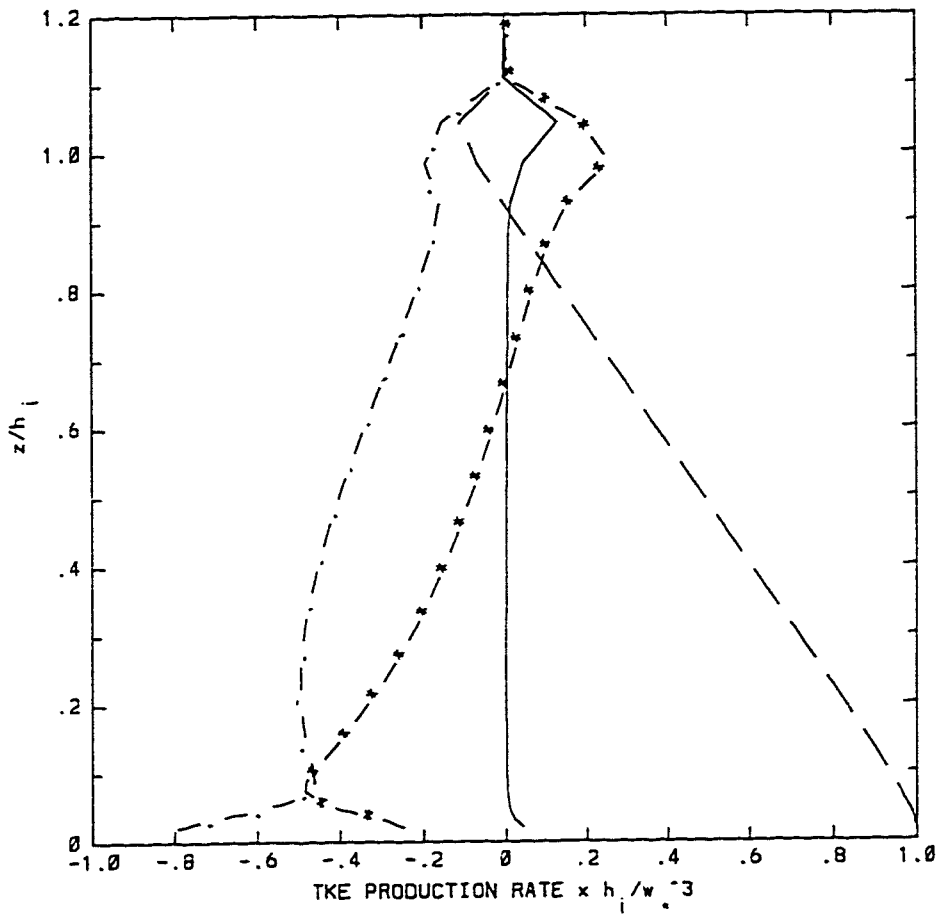

Fig. 28

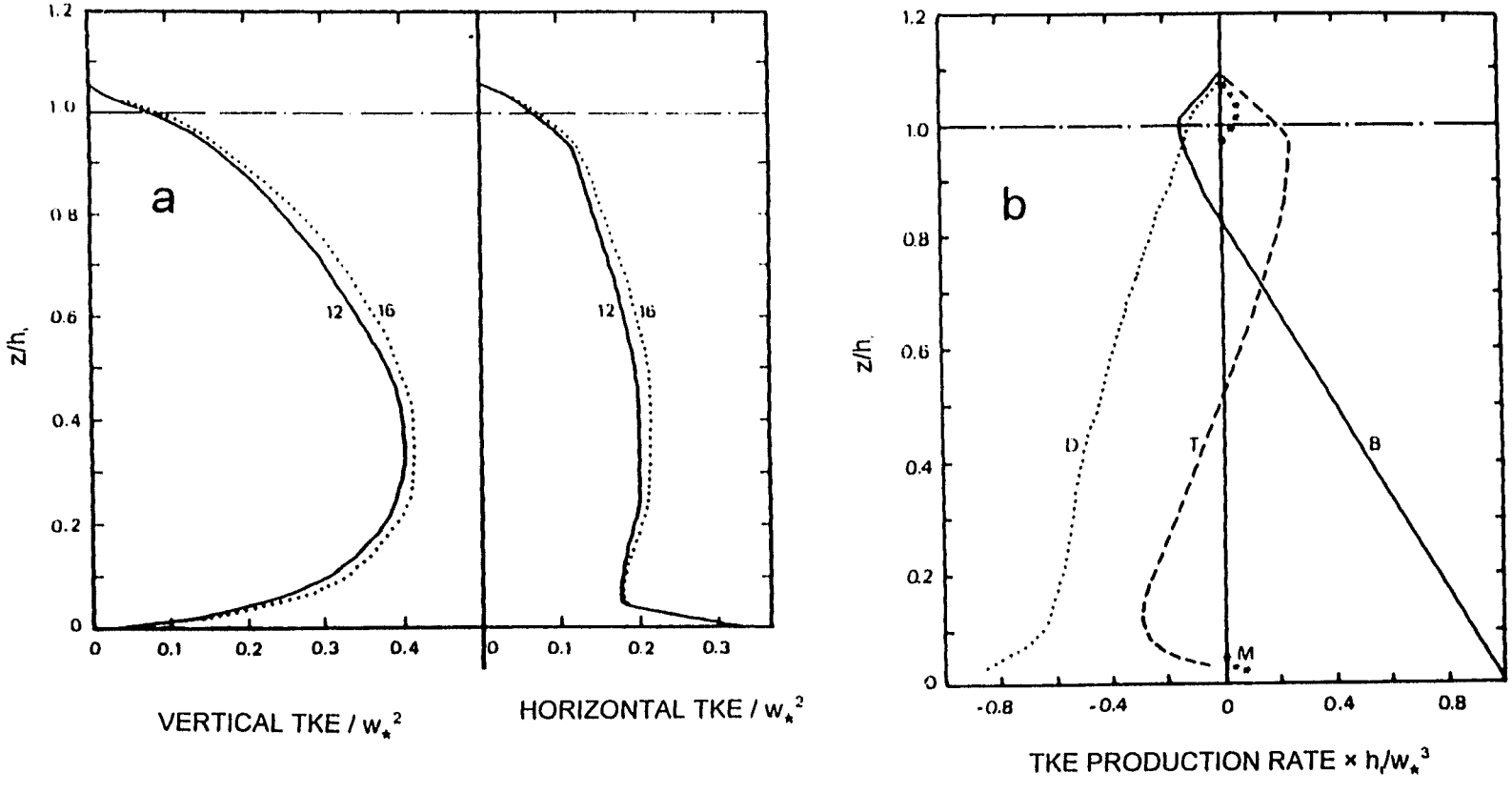
a
b
z/h
1.2
1.0
0.8
0.6
0.4
0.2
0
12
16
0.1
0.2
0.3
VERTICAL TKE / w*²
HORIZONTAL TKE / w*²
D
T
B
M
-0.8
-0.4
0.4
0.8
TKE PRODUCTION RATE × h/w*³

Fig. 29

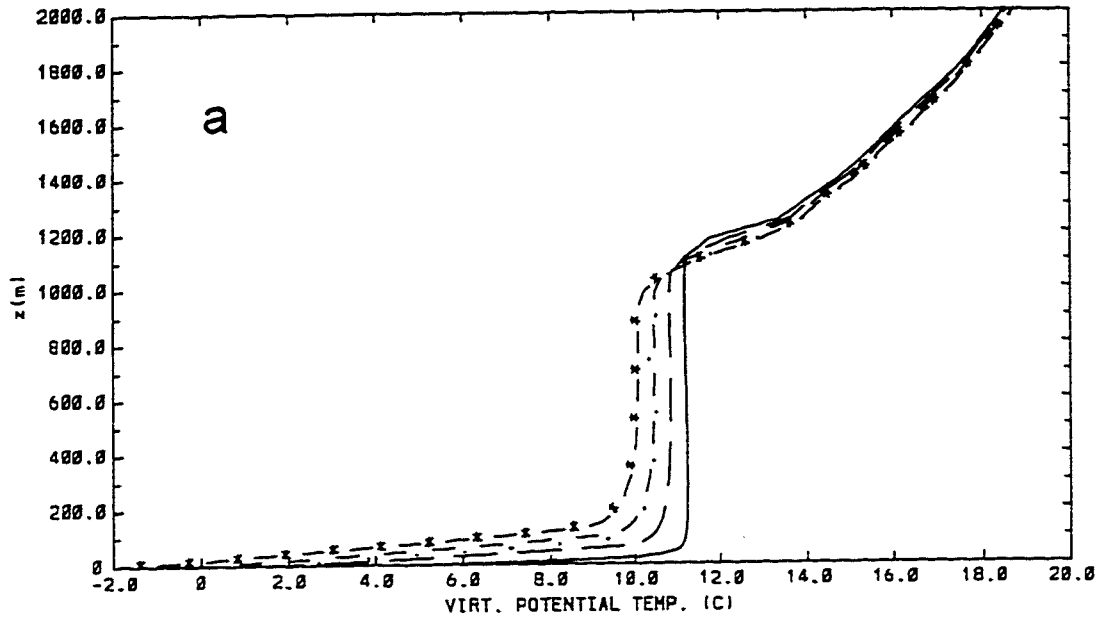
a
2000.0
1800.0
1600.0
1400.0
1200.0
1000.0
800.0
600.0
400.0
200.0
0
z(m)
-2.0
0
2.0
4.0
6.0
8.0
10.0
12.0
14.0
16.0
18.0
20.0
VIRT. POTENTIAL TEMP. (C)

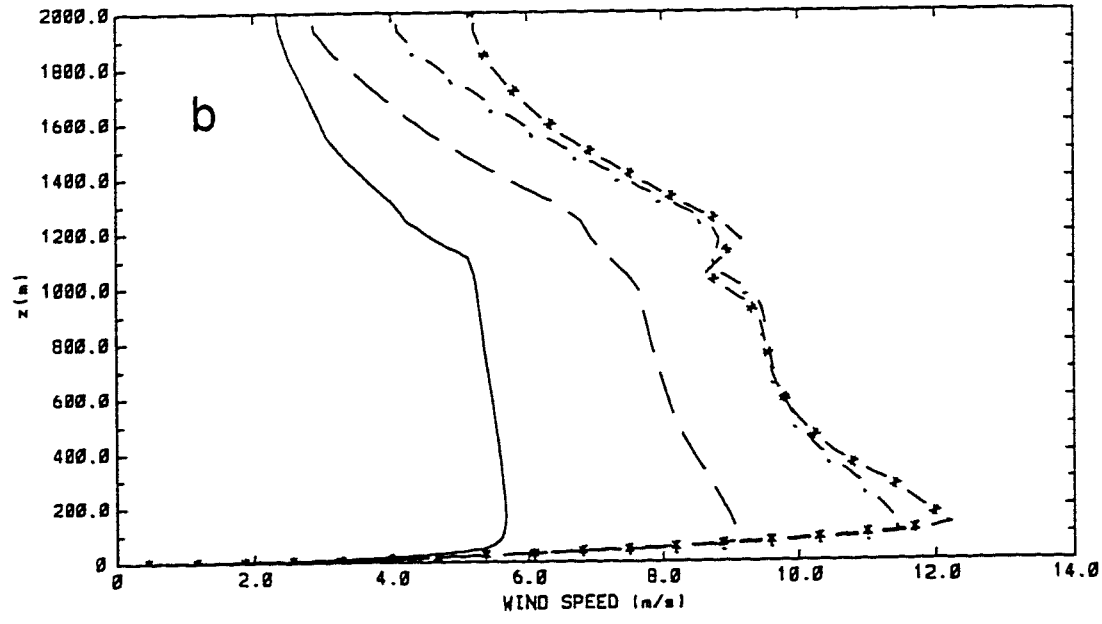
b
2000.0
1800.0
1600.0
1400.0
1200.0
1000.0
800.0
600.0
400.0
200.0
0
z(m)
0
2.0
4.0
6.0
8.0
10.0
12.0
14.0
WIND SPEED (m/s)

Fig. 30

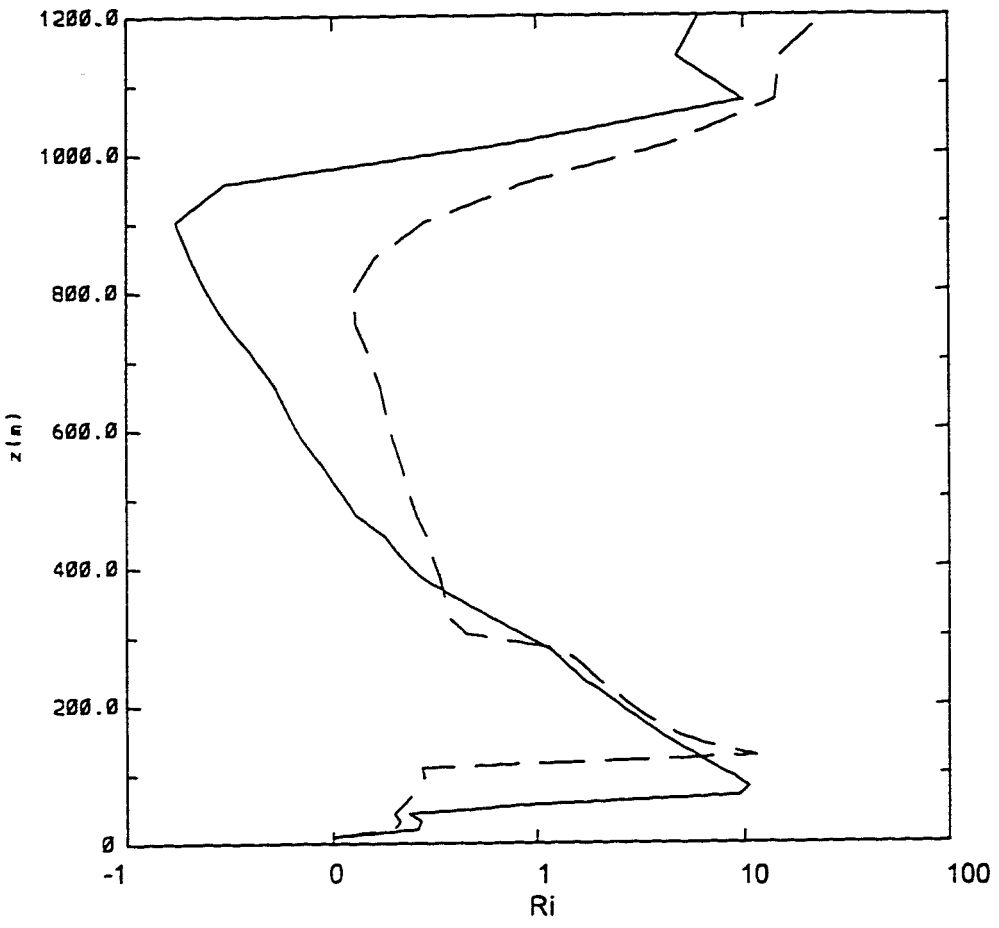

Fig. 31

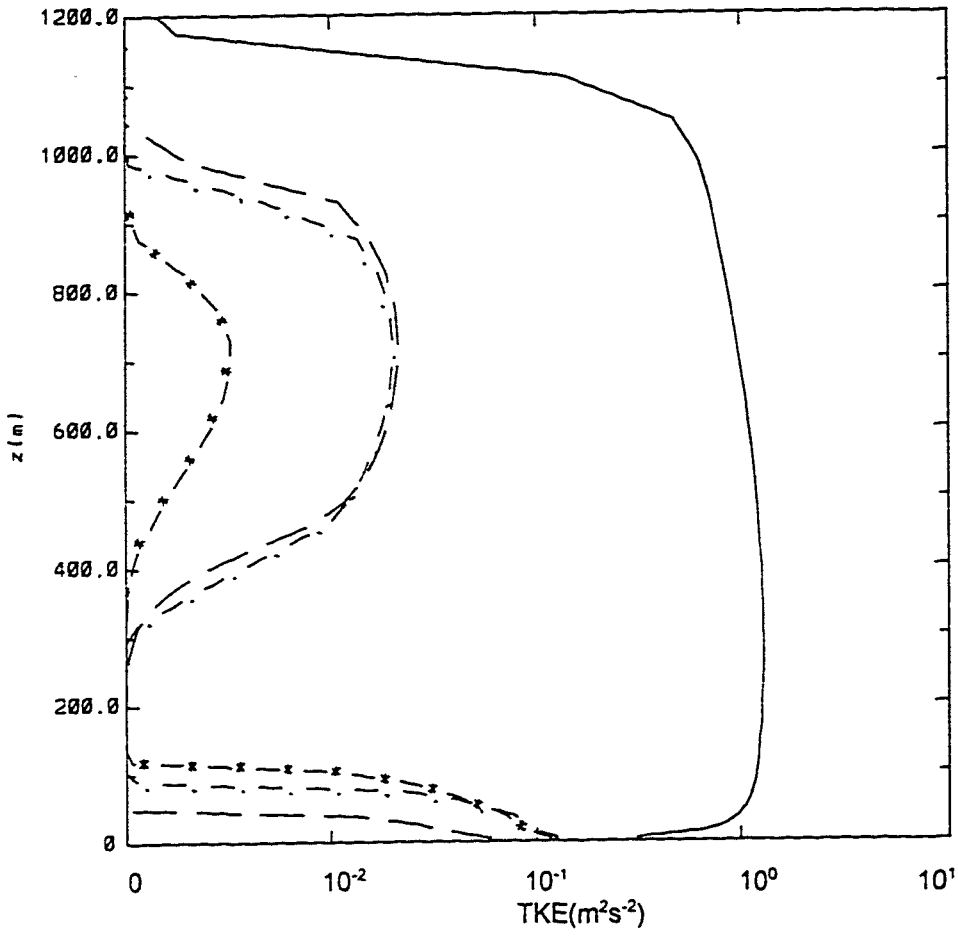

Fig. 32

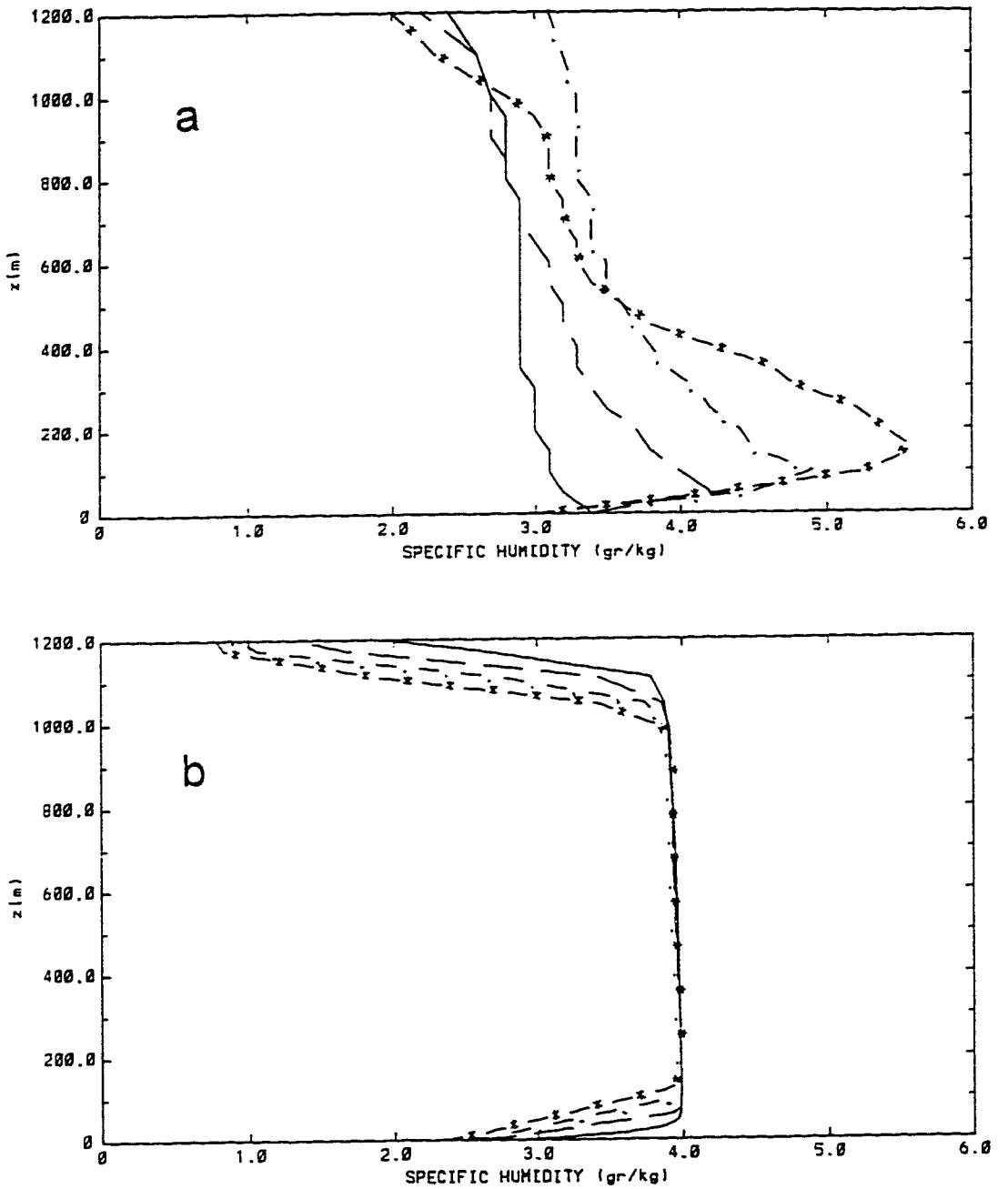
a
b
1200.0
1000.0
800.0
600.0
400.0
200.0
0
z(m)
0
1.0
2.0
3.0
4.0
5.0
6.0
SPECIFIC HUMIDITY (gr/kg)

Fig. 33

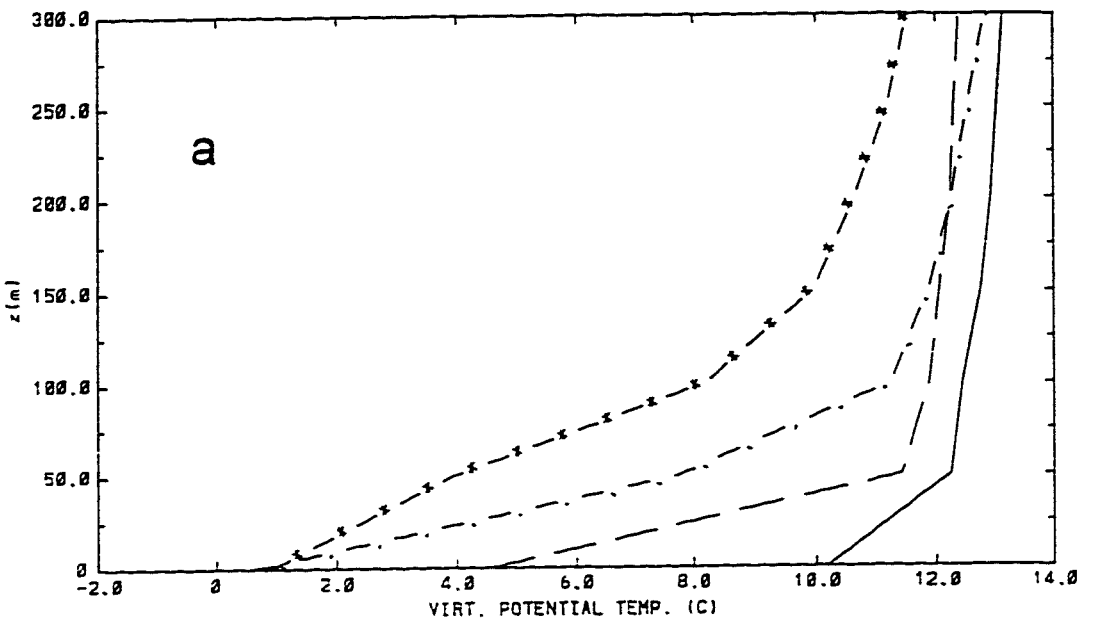
a
300.0
250.0
200.0
150.0
100.0
50.0
0
z(m)
-2.0
0
2.0
4.0
6.0
8.0
10.0
12.0
14.0
VIRT. POTENTIAL TEMP. (C)

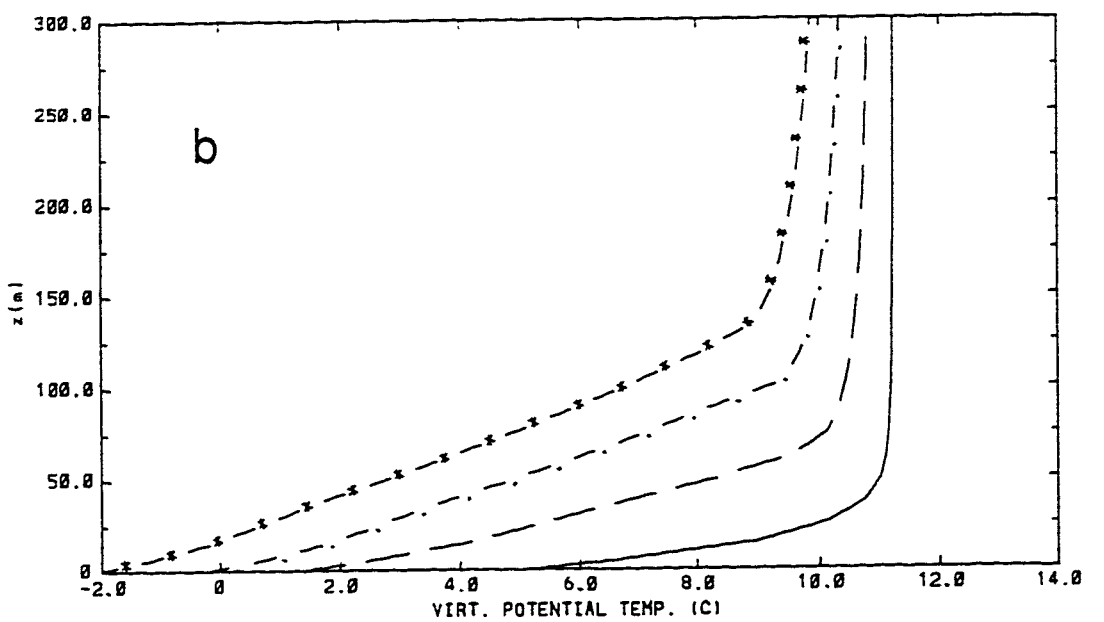
b
300.0
250.0
200.0
150.0
100.0
50.0
0
z(m)
-2.0
0
2.0
4.0
6.0
8.0
10.0
12.0
14.0
VIRT. POTENTIAL TEMP. (C)

Fig. 34

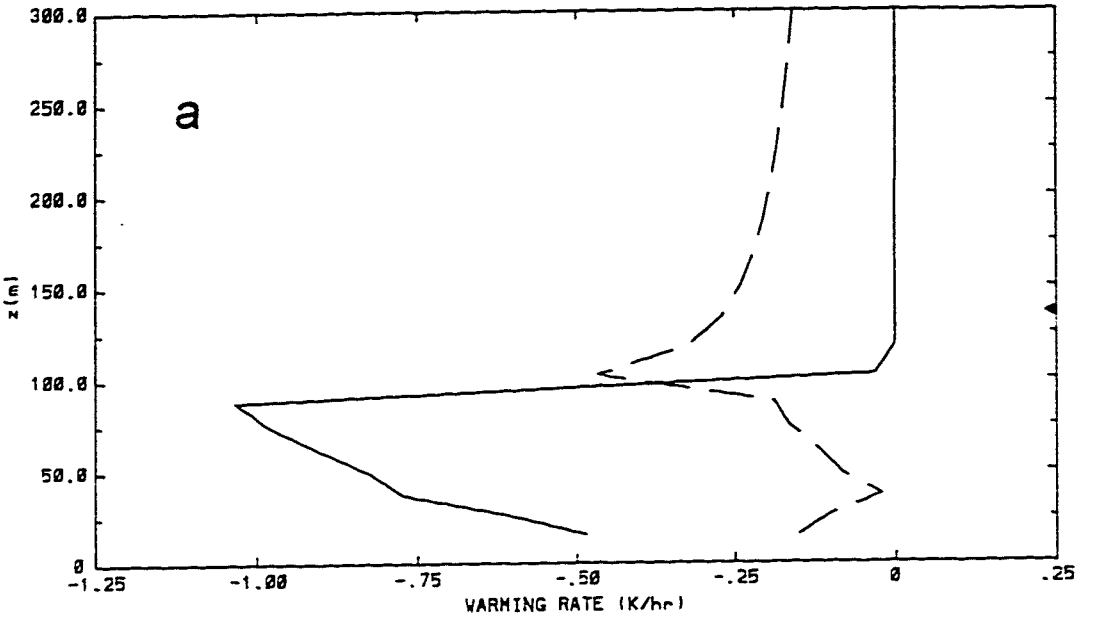
a
300.0
250.0
200.0
150.0
100.0
50.0
0
z(m)
-1.25
-1.00
-.75
-.50
-.25
0
.25
WARMING RATE (K/hr)

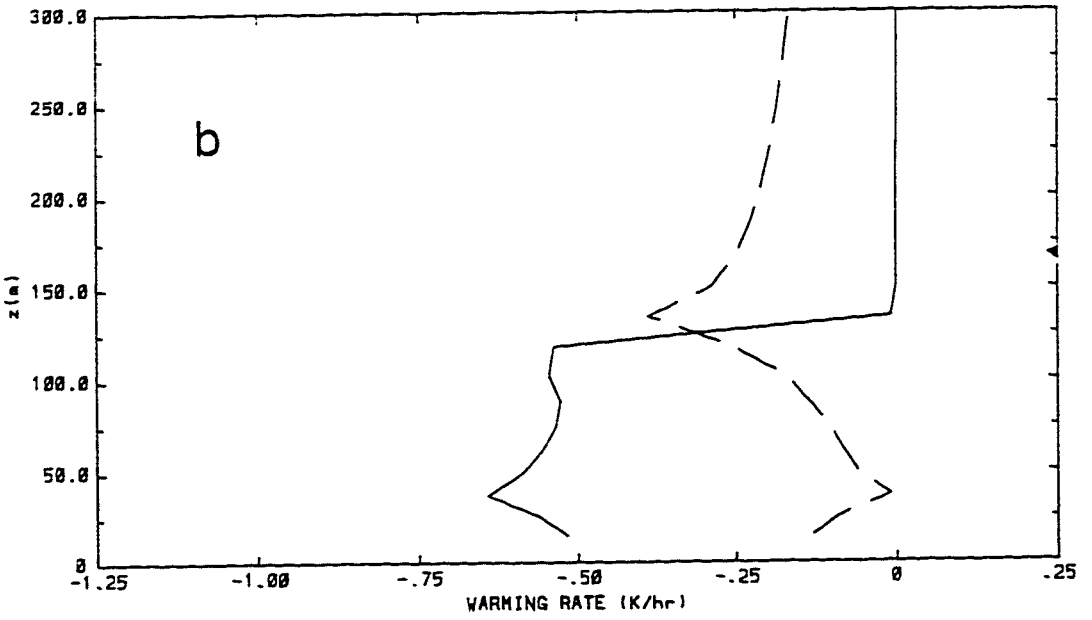
b
300.0
250.0
200.0
150.0
100.0
50.0
0
z(m)
-1.25
-1.00
-.75
-.50
-.25
0
.25
WARMING RATE (K/hr)

Fig. 35

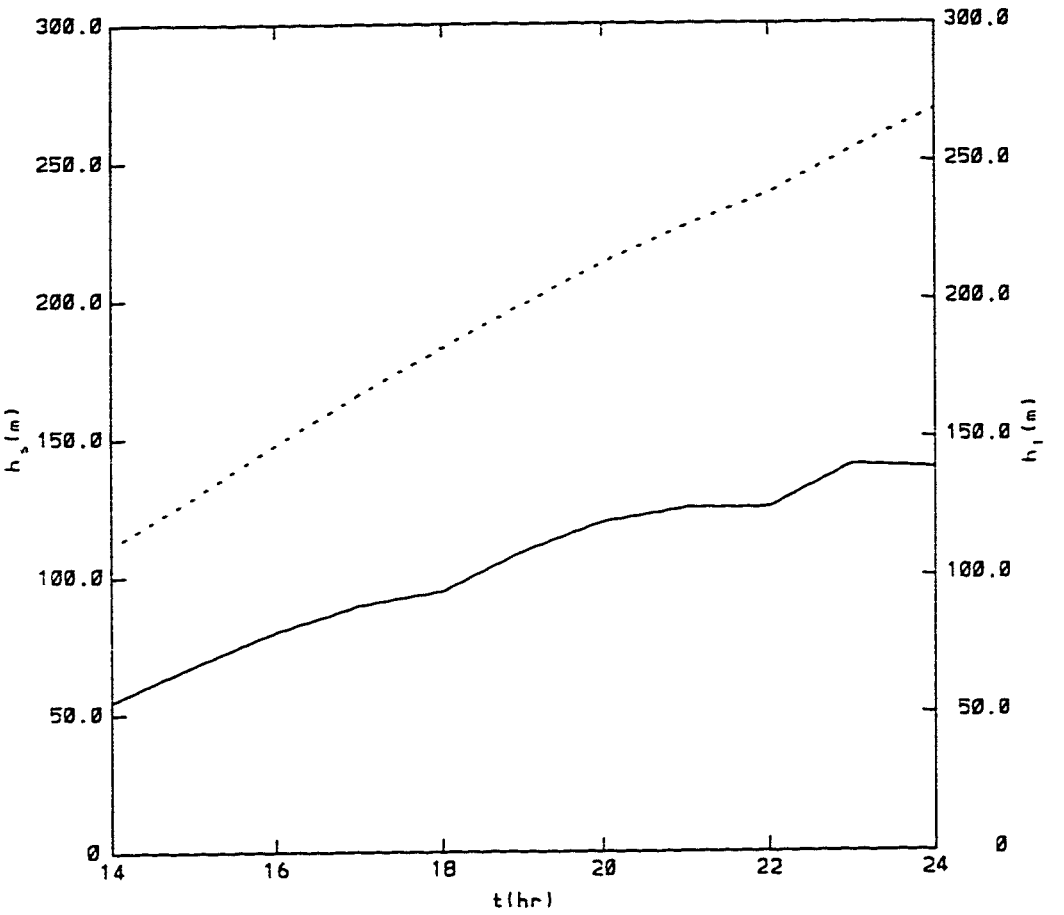

Fig. 36

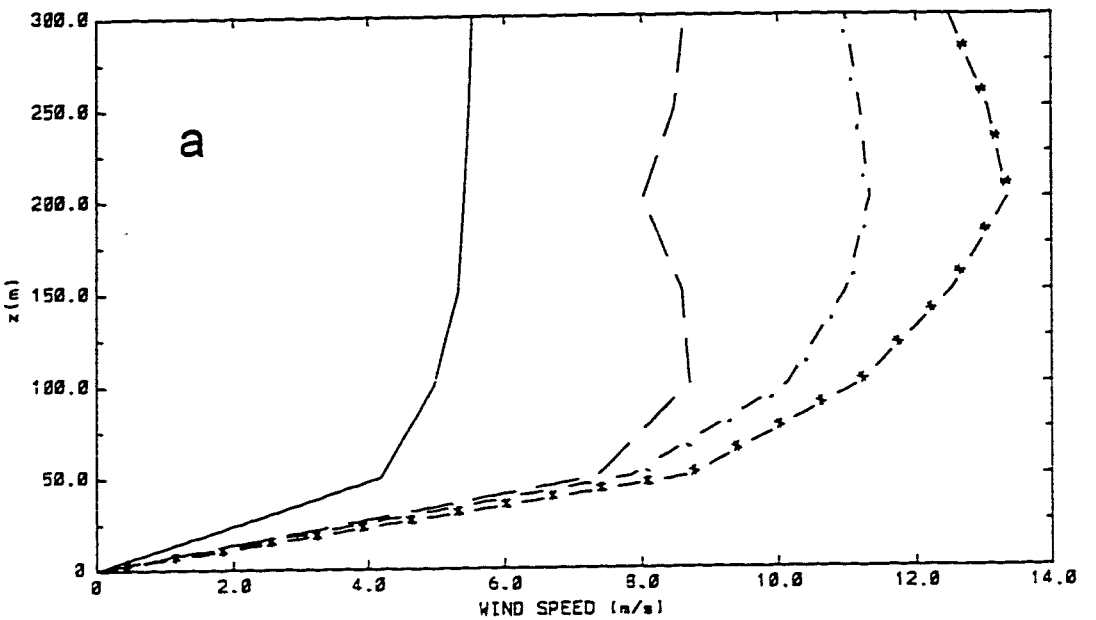
a
300.0
250.0
200.0
150.0
100.0
50.0
0
z(m)
0
2.0
4.0
6.0
8.0
10.0
12.0
14.0
WIND SPEED (m/s)

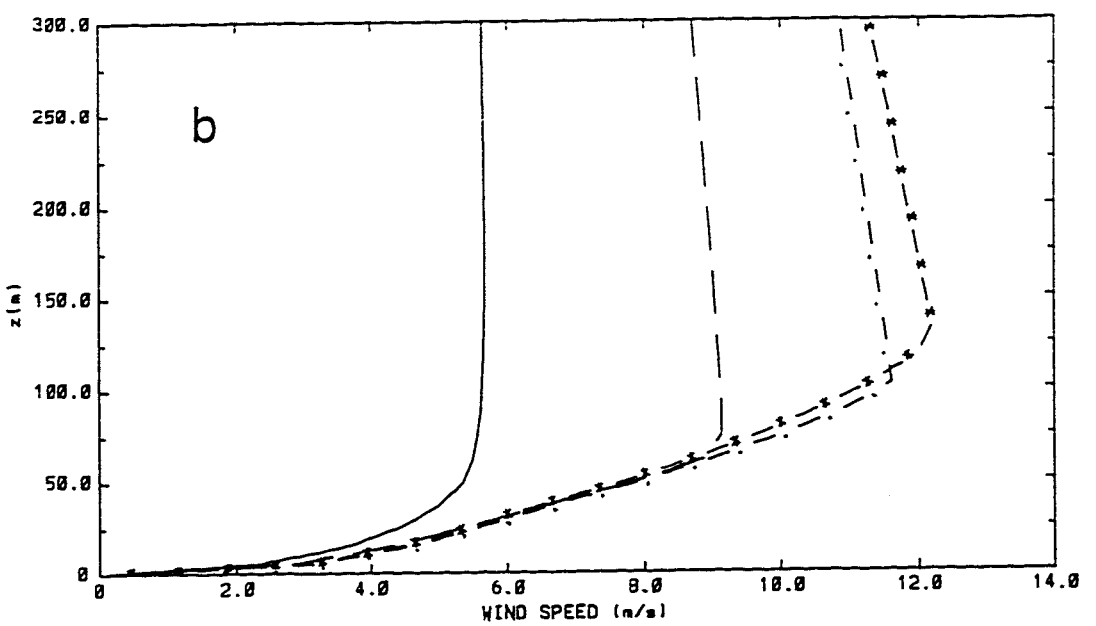
b
300.0
250.0
200.0
150.0
100.0
50.0
0
z(m)
0
2.0
4.0
6.0
8.0
10.0
12.0
14.0
WIND SPEED (m/s)

Fig. 37

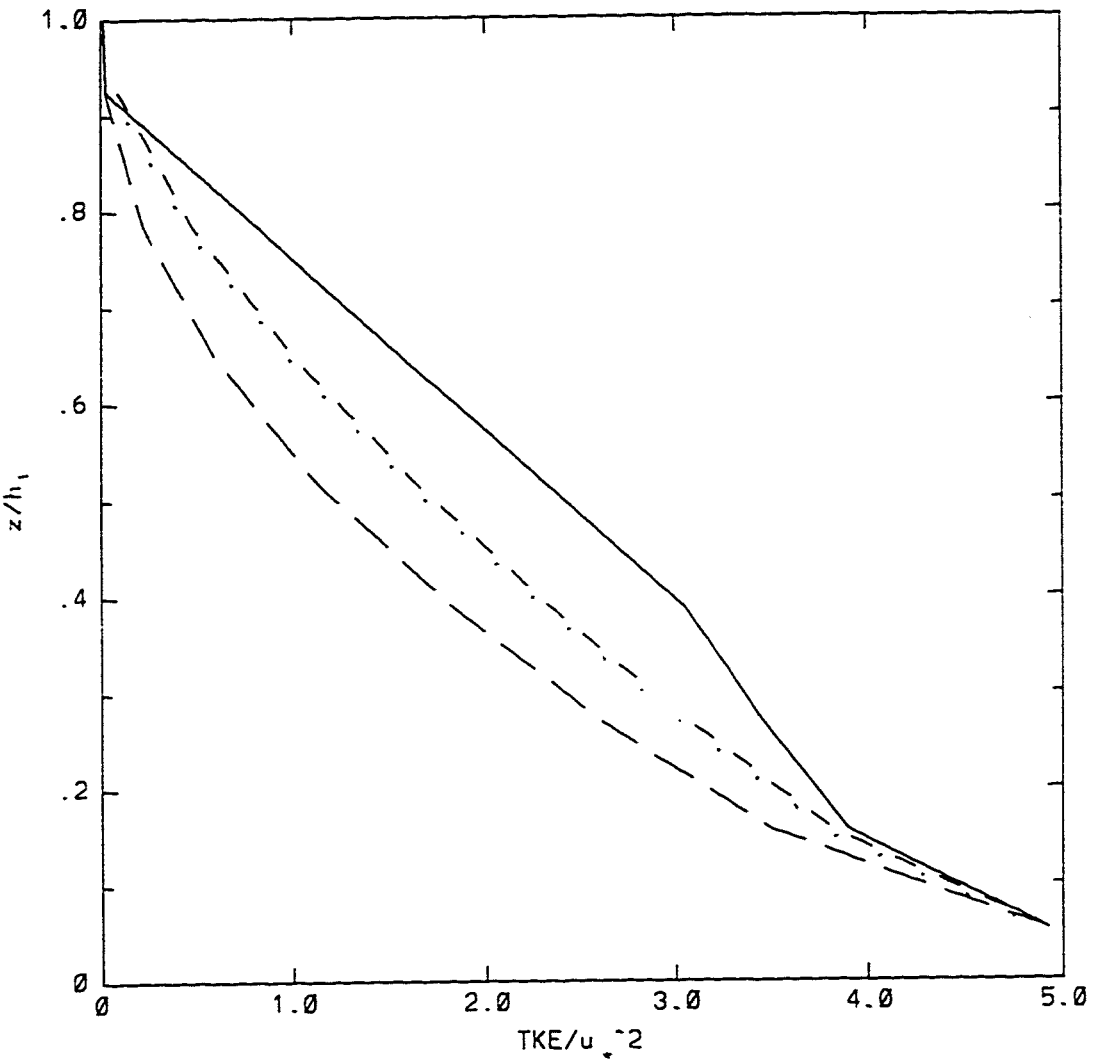

Fig. 38

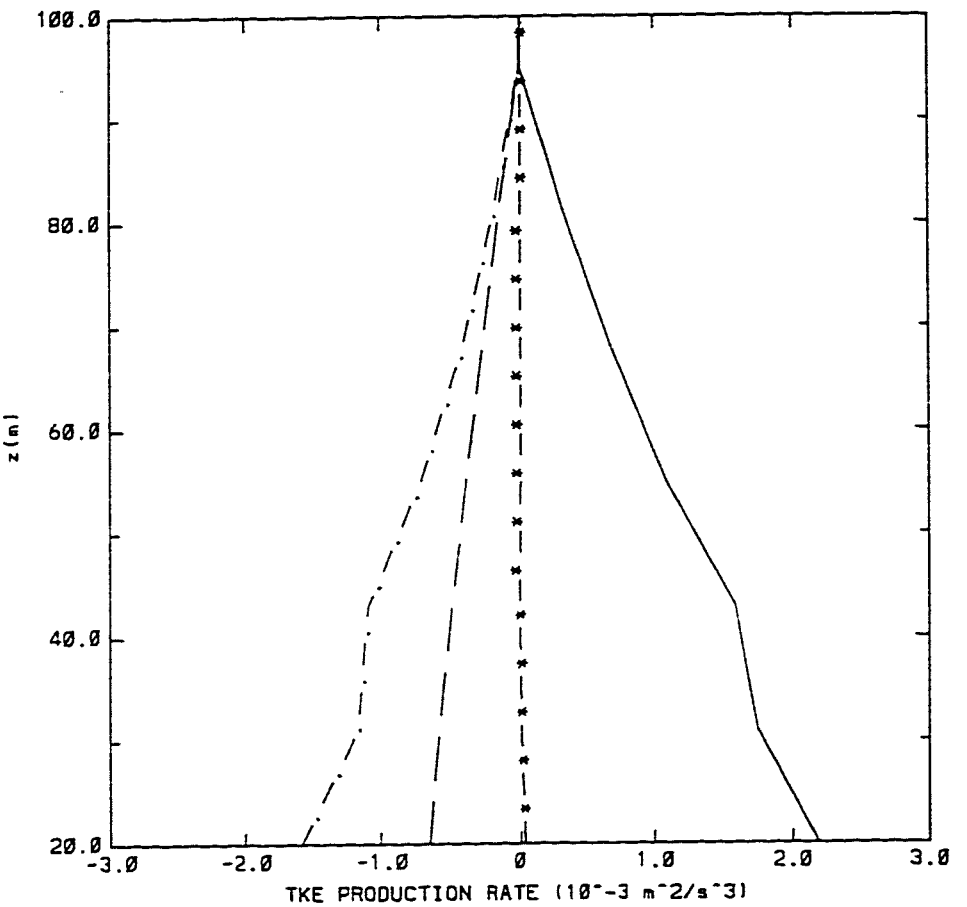
100.0
80.0
60.0
40.0
20.0
z(m)
-3.0
-2.0
-1.0
0
1.0
2.0
3.0
TKE PRODUCTION RATE (10^-3 m^2/s^3)

Fig. 39

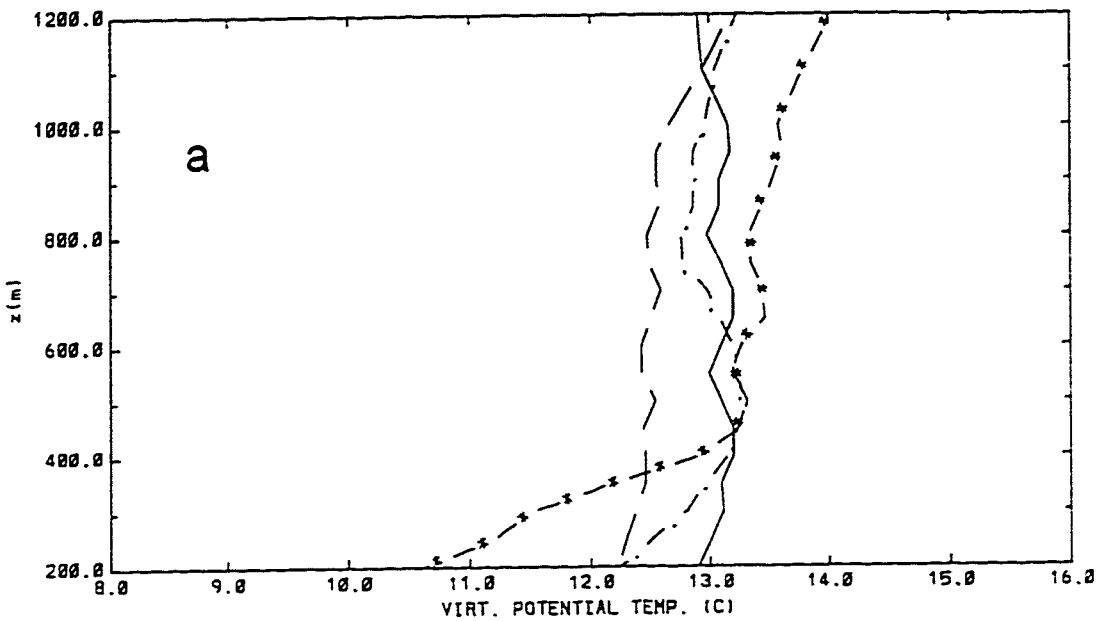
a
1200.0
1000.0
800.0
600.0
400.0
200.0
z(m)
8.0
9.0
10.0
11.0
12.0
13.0
14.0
15.0
16.0
VIRT. POTENTIAL TEMP. (C)

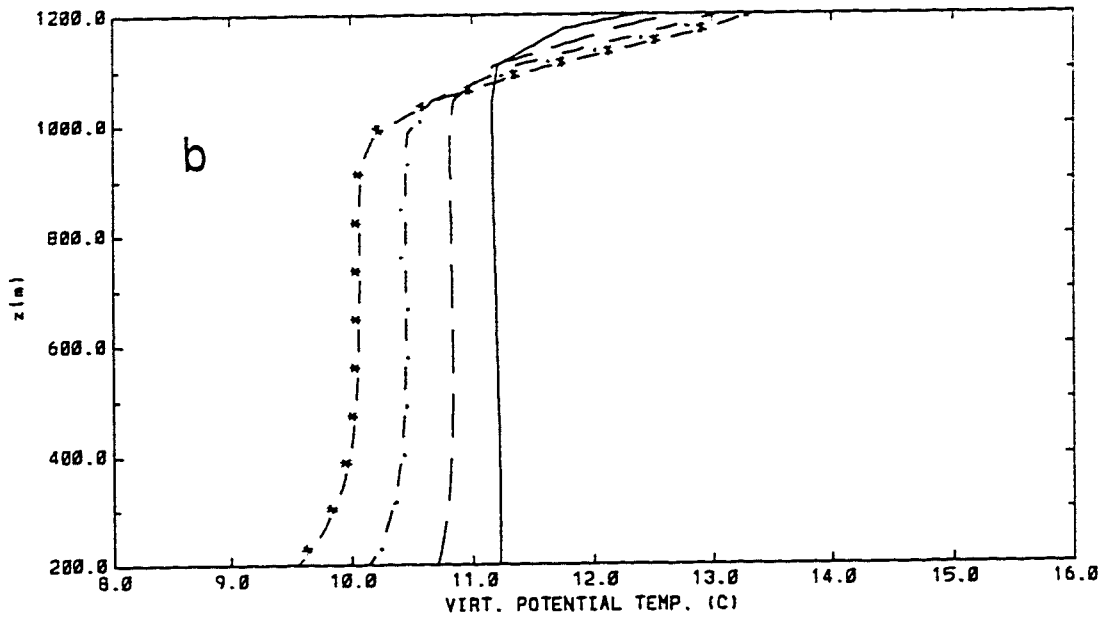
b
1200.0
1000.0
800.0
600.0
400.0
200.0
z(m)
8.0
9.0
10.0
11.0
12.0
13.0
14.0
15.0
16.0
VIRT. POTENTIAL TEMP. (C)

Fig. 40

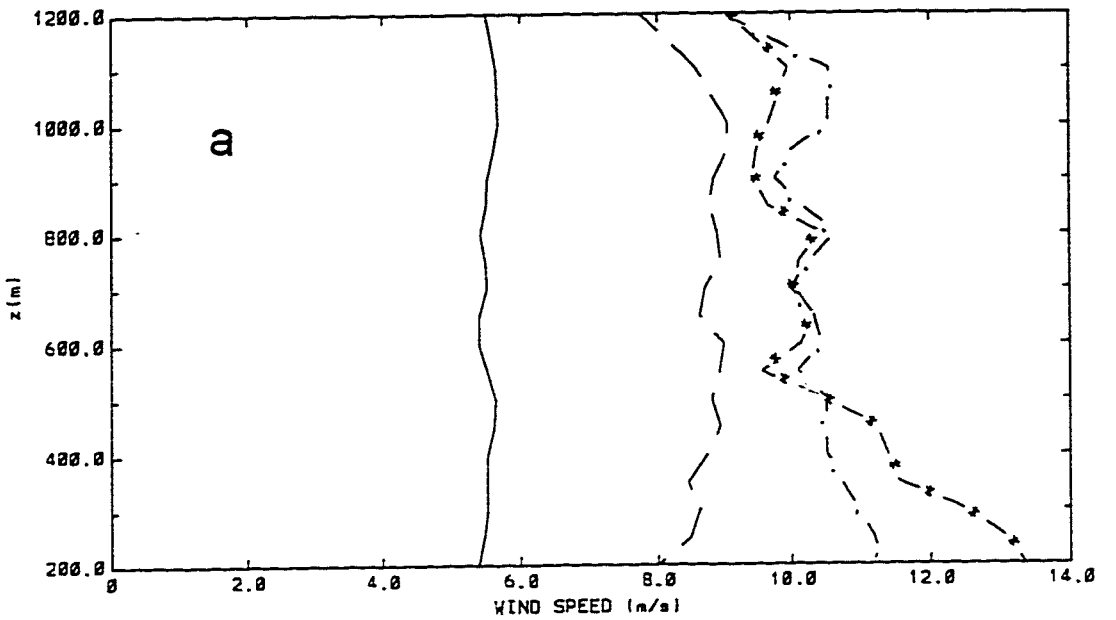
a
1200.0
1000.0
800.0
600.0
400.0
200.0
z(m)
0
2.0
4.0
6.0
8.0
10.0
12.0
14.0
WIND SPEED (m/s)

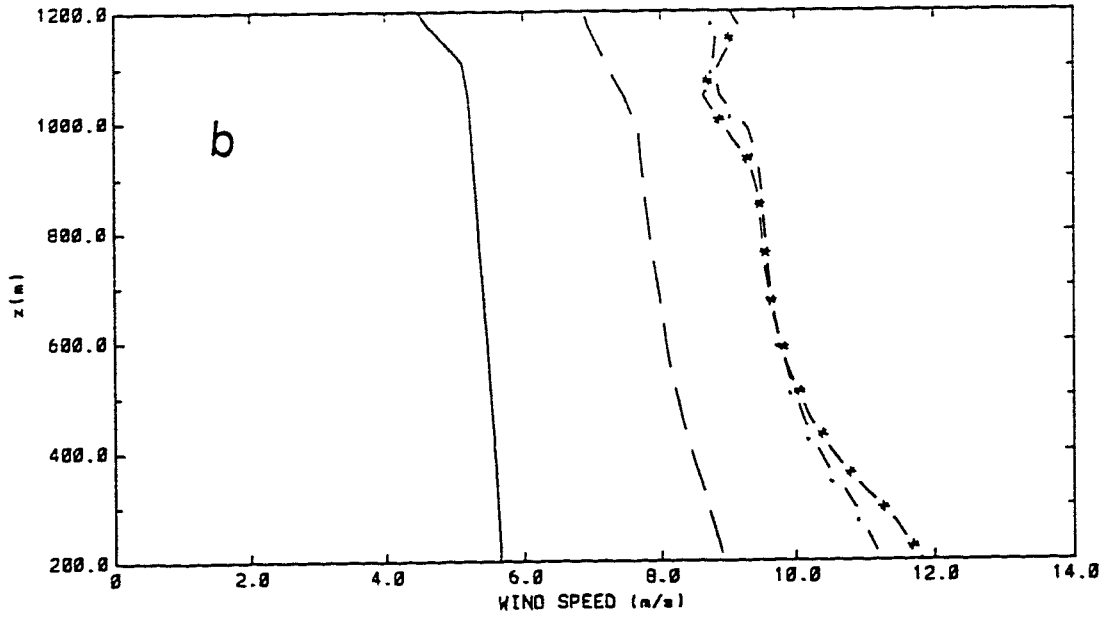
b
1200.0
1000.0
800.0
600.0
400.0
200.0
z(m)
0
2.0
4.0
6.0
8.0
10.0
12.0
14.0
WIND SPEED (m/s)

Fig. 41

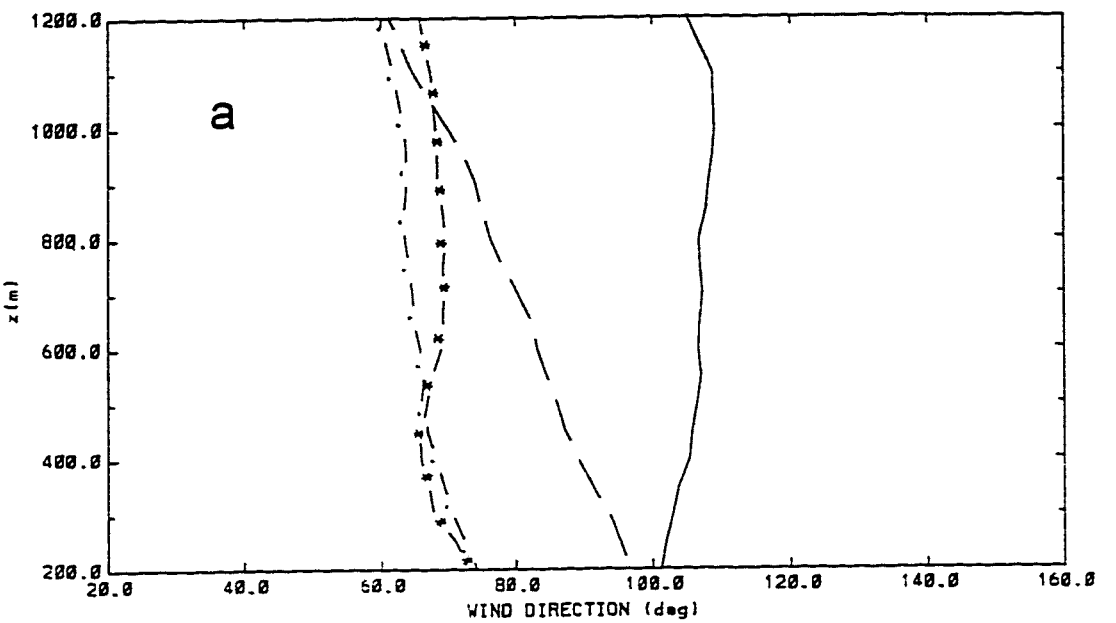
a
1200.0
1000.0
800.0
600.0
400.0
200.0
z(m)
20.0
40.0
60.0
80.0
100.0
120.0
140.0
160.0
WIND DIRECTION (deg)

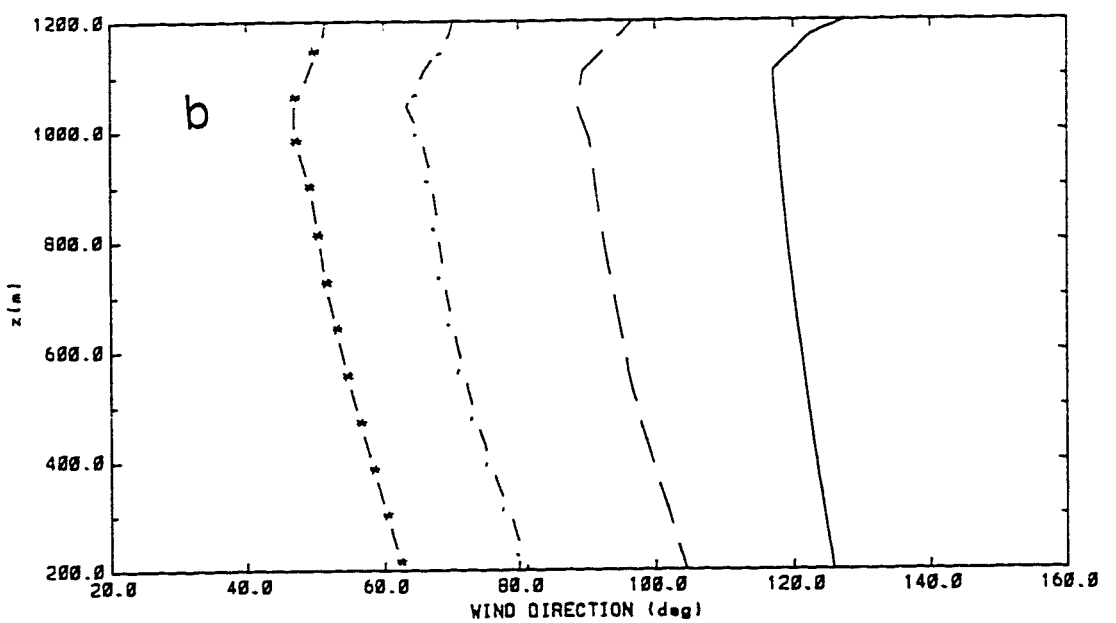
b
1200.0
1000.0
800.0
600.0
400.0
200.0
z(m)
20.0
40.0
60.0
80.0
100.0
120.0
140.0
160.0
WIND DIRECTION (deg)

Fig. 42

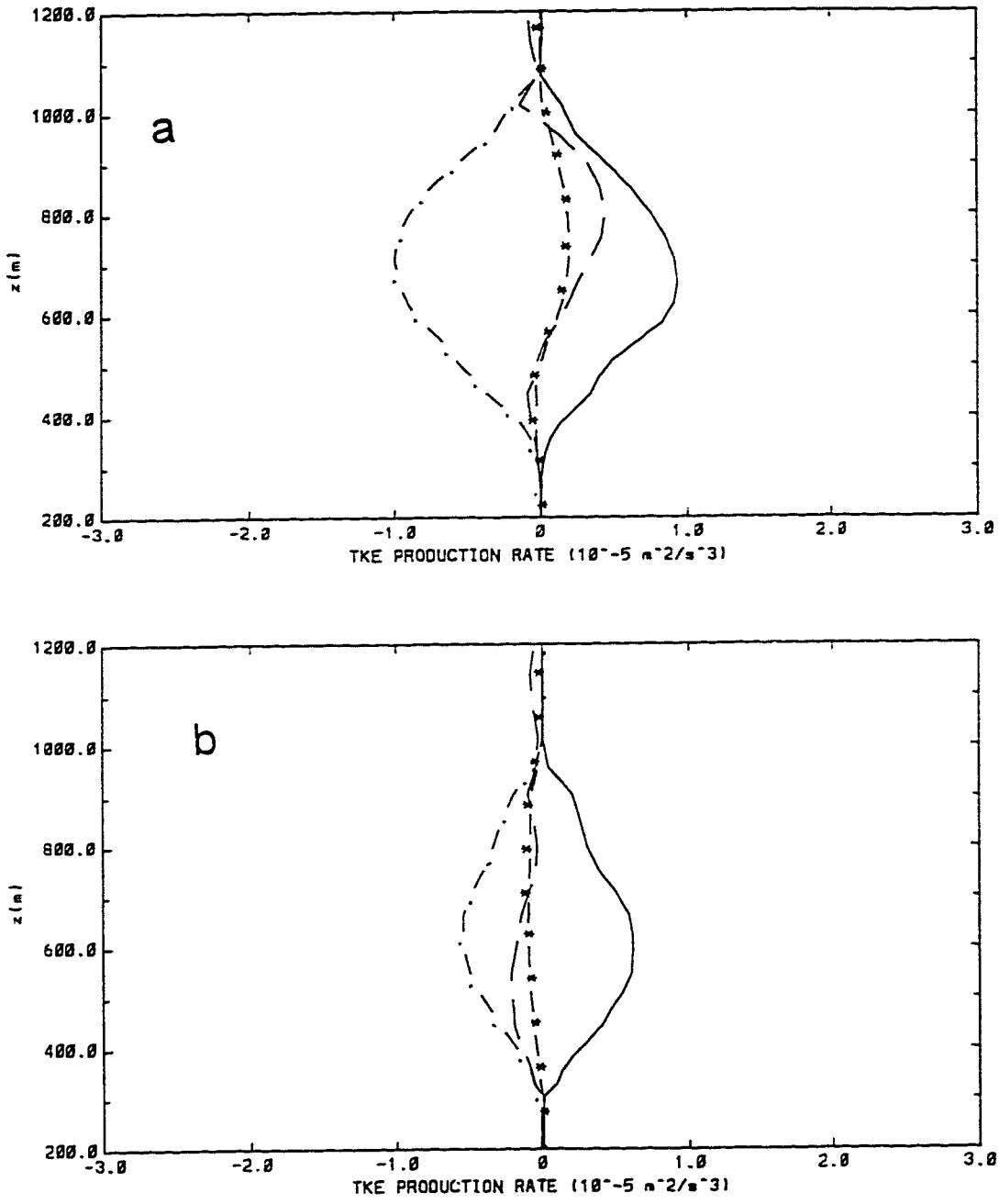
a
b
1200.0
1000.0
800.0
600.0
400.0
200.0
z(m)
-3.0
-2.0
-1.0
0
1.0
2.0
3.0
TKE PRODUCTION RATE (10^-5 m^2/s^3)

Fig. 43

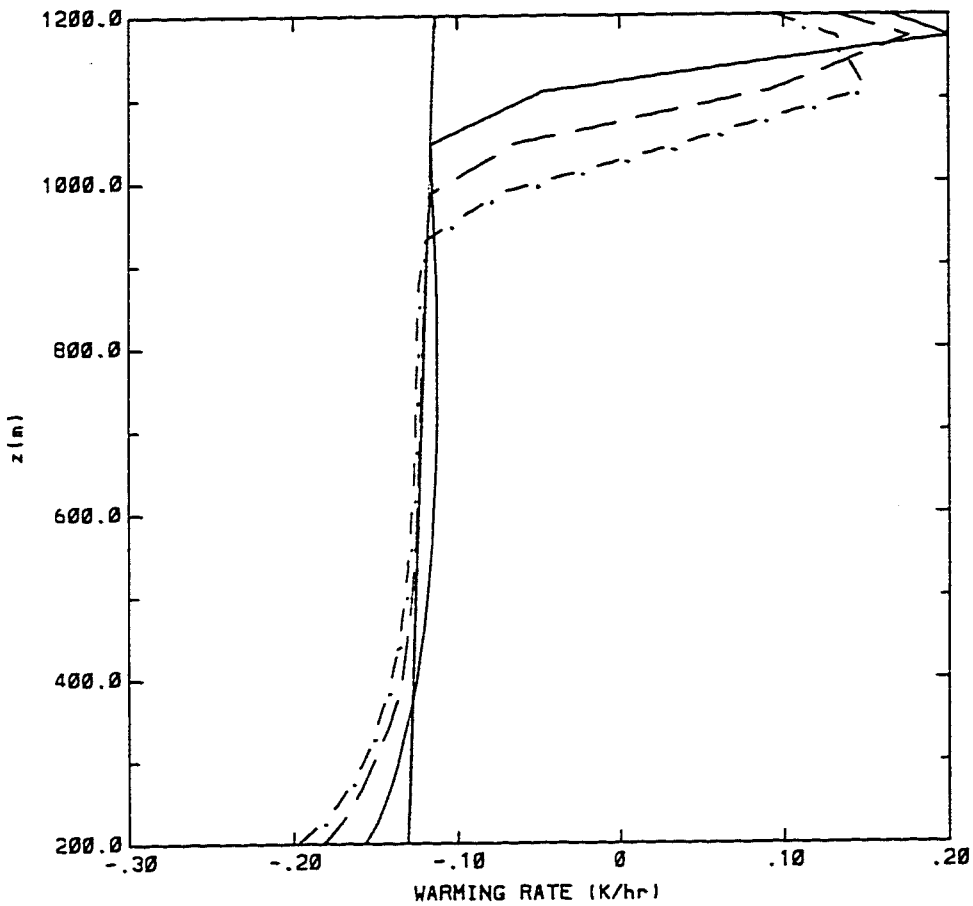
1200.0
1000.0
800.0
600.0
400.0
200.0
z(m)
-.30
-.20
-.10
0
.10
.20
WARMING RATE (K/hr)

Fig. 44

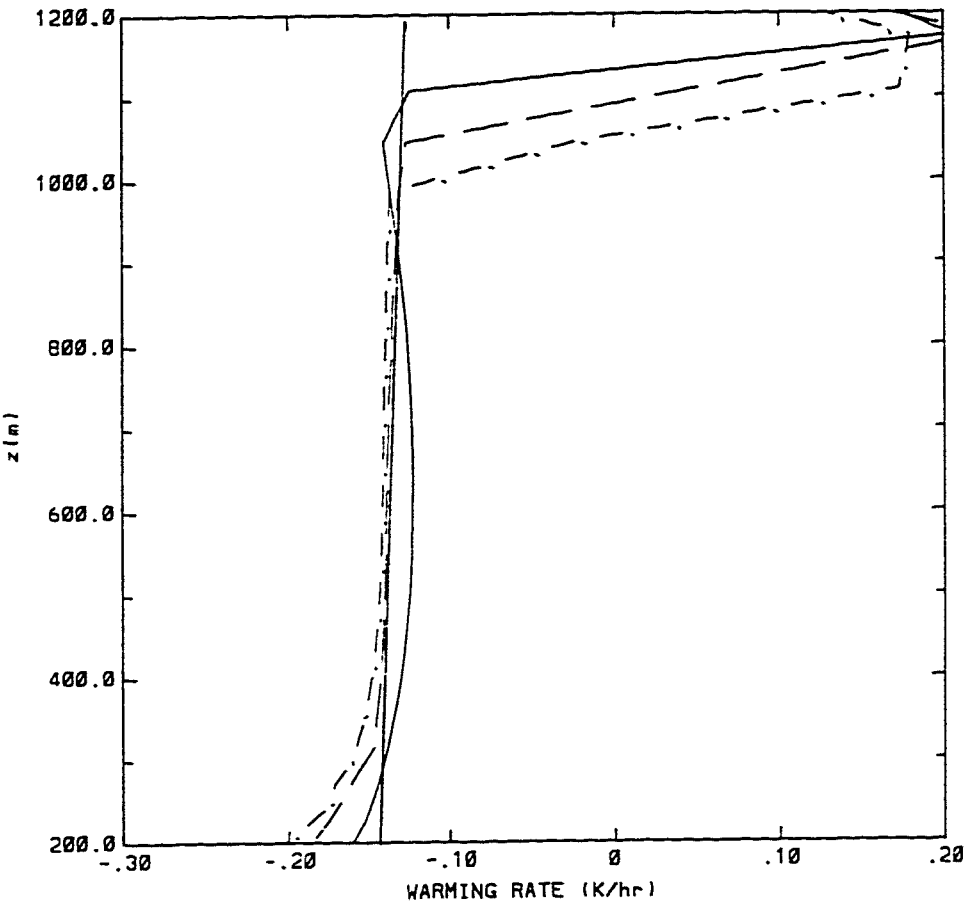
1200.0
1000.0
800.0
600.0
400.0
200.0
z(m)
-.30
-.20
-.10
0
.10
.20
WARMING RATE (K/hr)

Fig. 45

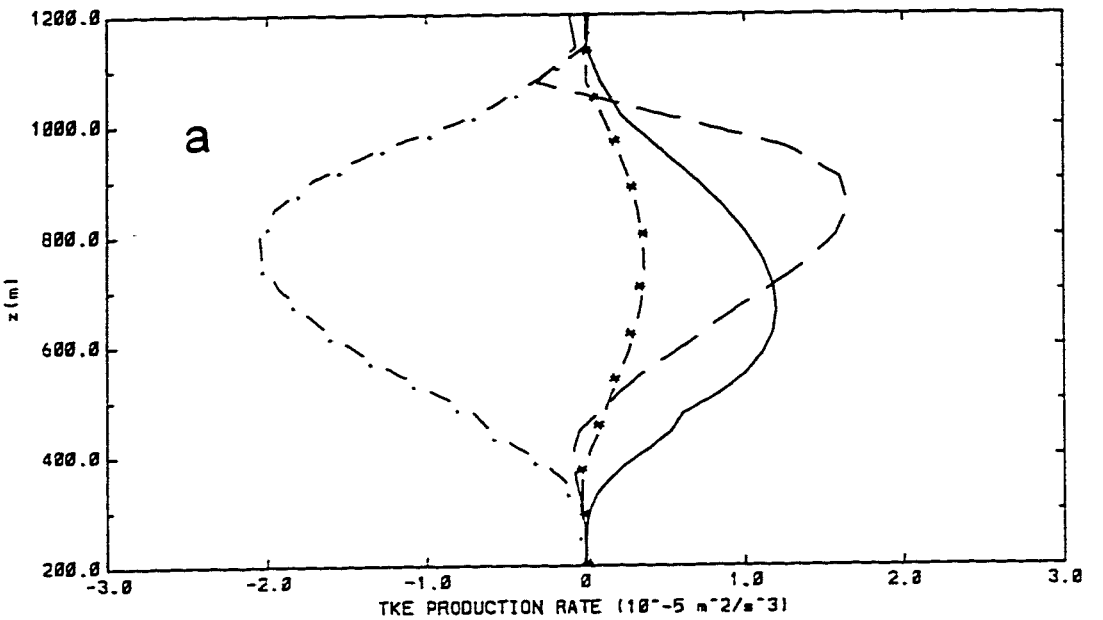
a
1200.0
1000.0
800.0
600.0
400.0
200.0
z(m)
-3.0
-2.0
-1.0
0
1.0
2.0
3.0
TKE PRODUCTION RATE (10^-5 m^2/s^3)

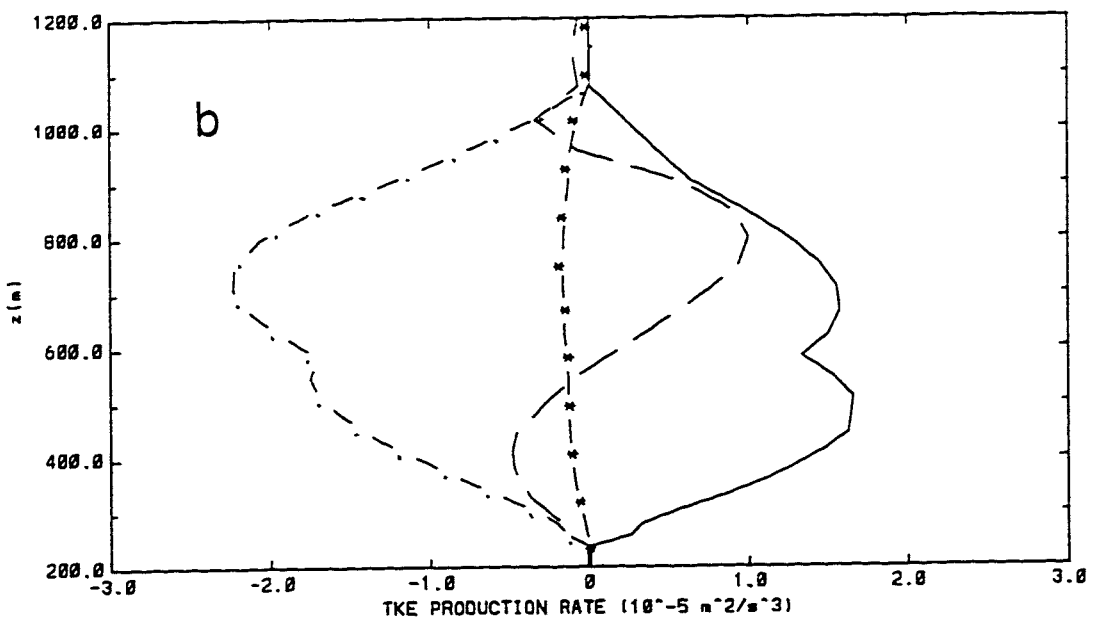
b
1200.0
1000.0
800.0
600.0
400.0
200.0
z(m)
-3.0
-2.0
-1.0
0
1.0
2.0
3.0
TKE PRODUCTION RATE (10^-5 m^2/s^3)

Fig. 46

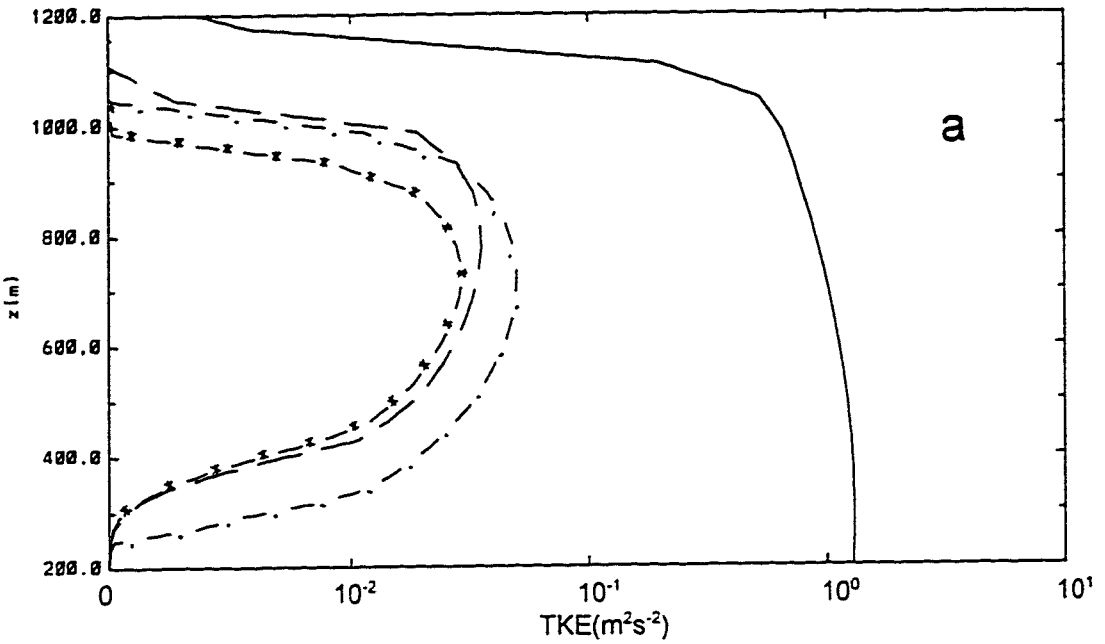
1200.0
1000.0
800.0
600.0
400.0
200.0
z(m)
a
0
10-2
10-1
100
101
TKE(m2s-2)

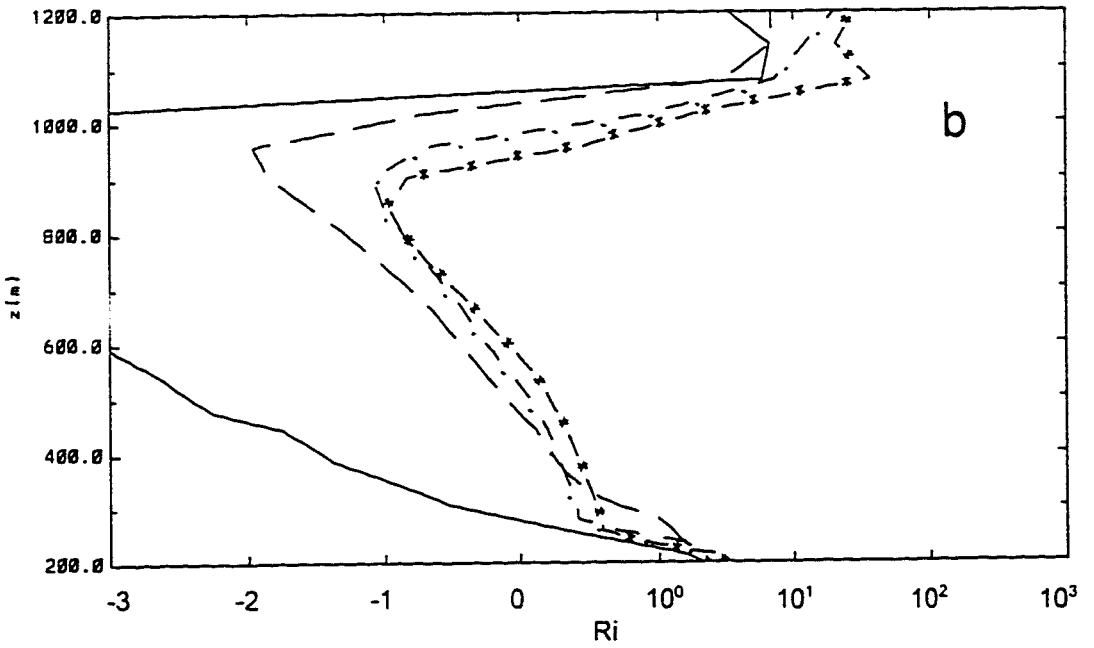
1200.0
1000.0
800.0
600.0
400.0
200.0
z(m)
b
-3
-2
-1
0
100
101
102
103
Ri

Fig. 47

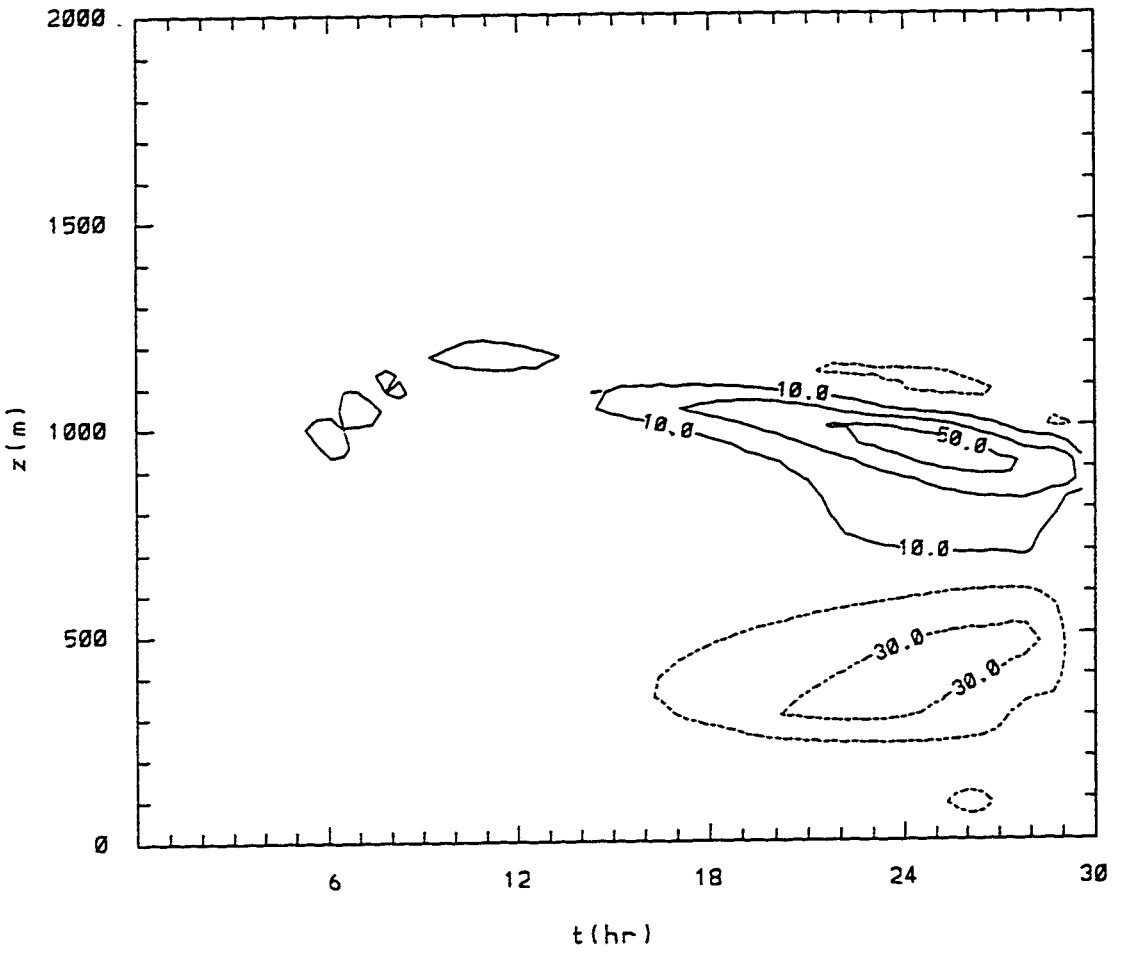

Fig. 48

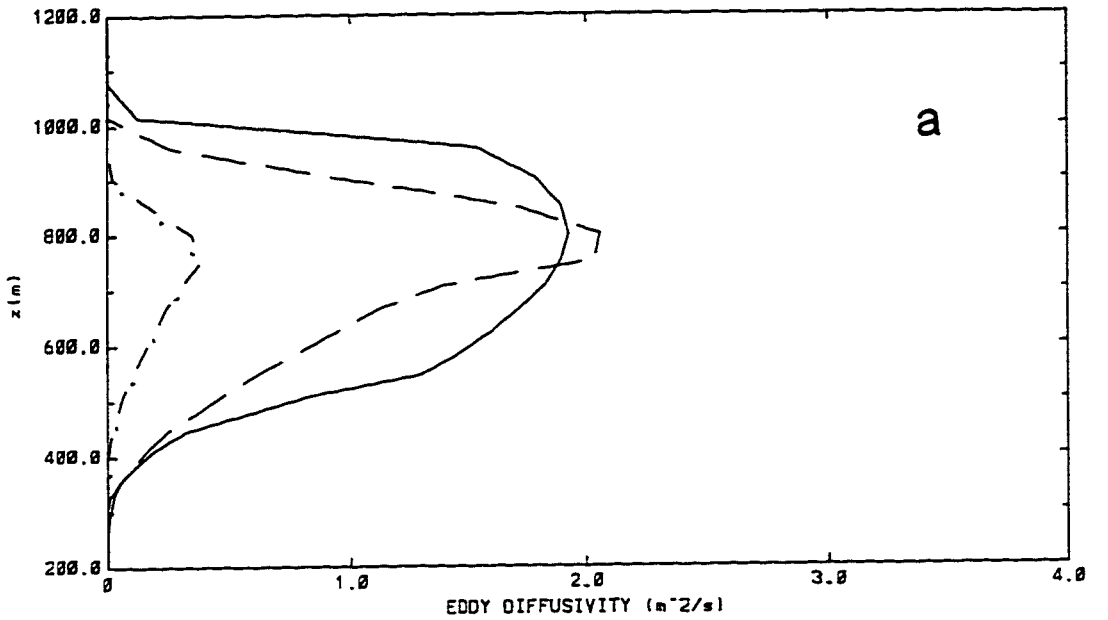
1200.0
1000.0
800.0
600.0
400.0
200.0
z(m)
a
0
1.0
2.0
3.0
4.0
EDDY DIFFUSIVITY (m^2/s)

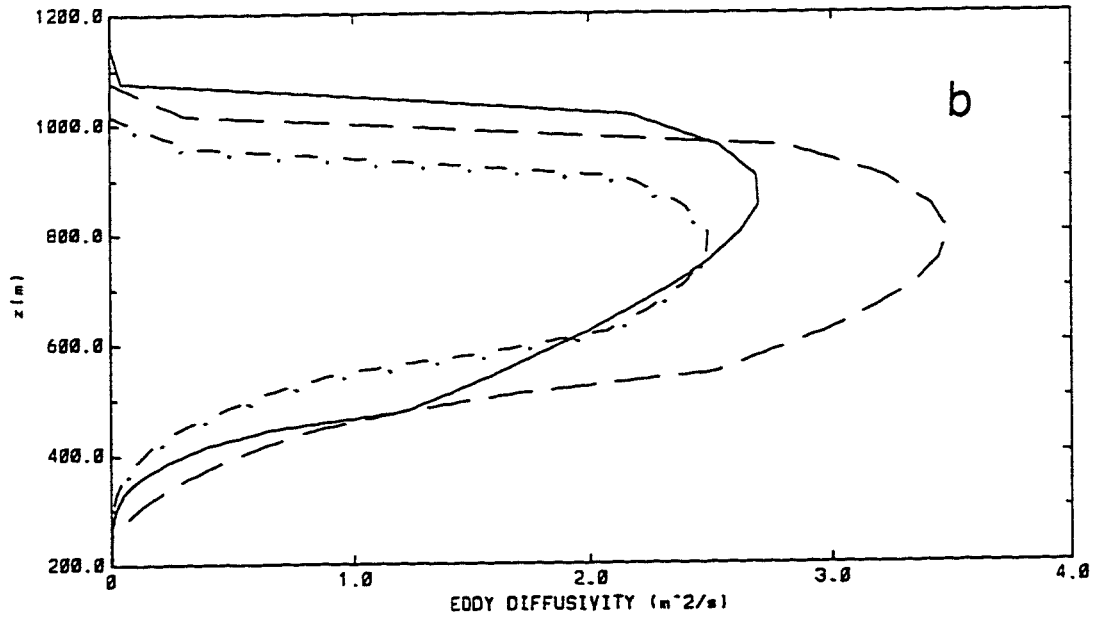
1200.0
1000.0
800.0
600.0
400.0
200.0
z(m)
b
0
1.0
2.0
3.0
4.0
EDDY DIFFUSIVITY (m^2/s)

Fig. 49

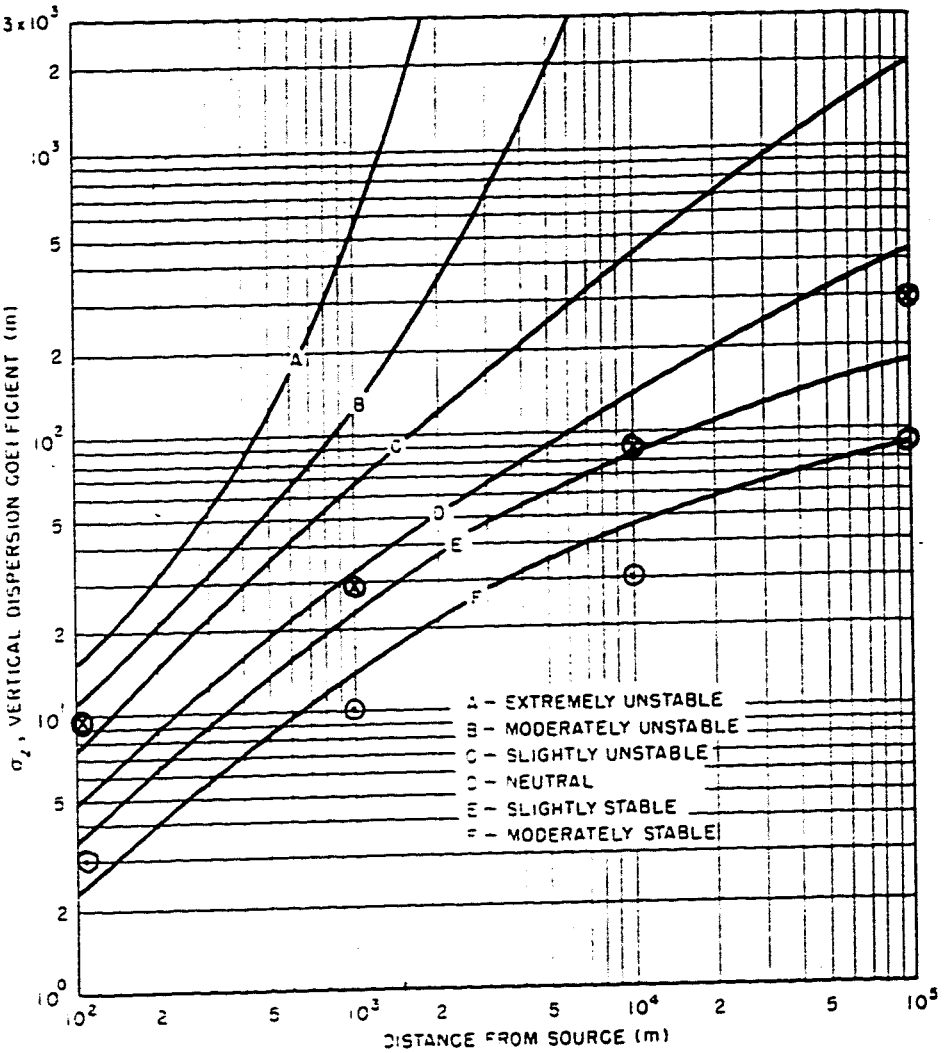
σ_z, VERTICAL DISPERSION COEFFICIENT (m)
DISTANCE FROM SOURCE (m)
A
B
C
D
E
F
A – EXTREMELY UNSTABLE
B – MODERATELY UNSTABLE
C – SLIGHTLY UNSTABLE
D – NEUTRAL
E – SLIGHTLY STABLE
F – MODERATELY STABLE

Fig. 50